PERCEPTION AUGMENTATION AND ASSISTANCE FOR IMPROVED SURGICAL AWARENESS

By

Rashid Muhammed Yasin

Dissertation

Submitted to the Faculty of the

Graduate School of Vanderbilt University

in partial fulfillment of the requirements

for the degree of

DOCTOR OF PHILOSOPHY

in

Mechanical Engineering

January 31, 2020

Nashville, Tennessee

Approved:

Nabil Simaan, Ph.D

Robert Webster, Ph.D

Karl Zelik, Ph.D

Jack Noble, Ph.D

Peter Kazanzides, Ph.D

بسم الله الرحمن الرحيم

ACKNOWLEDGMENTS

I thank my wife, Eftitan, for her love, support, and strength. The pride and accomplishment I feel from this thesis is nothing in comparison to how much I have benefitted and grown from your companionship. I strive to emulate your accomplishments and character. You became a doctor before me, so now I'm getting closer to your level.

There would have been no graduate degree and no thesis without the guidance and example set by my parents. For their continual feedback throughout studies, I am eternally grateful. For Baba, I thank you for all the conversations that helped me understand the high level importance of my research and how to focus and crystalize my thoughts. Thank you, Mom, for being always encouraging me to work hard but also to take advantage of the one life that I have to live and not go *too* crazy with research work.

The members of the ARMA lab have been a continual source of assistance. From my early mentors, Jason and Haoran, who helped me learn the basics; to my comrades Nima, Long, and Giuseppe who struggled alongside me; to the next generation who I am proud to have continue the lab legacy, Colette, Andrew, Garrison, Neel, and Elan: you have been an important part of my career. Thank you for your camaraderie and feedback.

I thank my collaborators from a variety of institutions. All the members of the NRI-CSA grant were integral to the success of my research and your collaboration is much appreciated. Our clinical collaborators at Vanderbilt were extremely important in providing clinical expertise and guidance: Drs. Rivas, O'Connell, Dedmon, and Hunter. I especially appreciate Dr. Labadie for providing access to shared research space and a CT scanner. Further, a thank you to the physicians who took part in our user study (especially Drs. Chaudhri and Roland who travelled from New York to participate). I also thank Claudiu (الله يرحمه) and the team from Cochlear for their assistance and feedback throughout our research collaboration.

I also thank the funding institutions. NSF NRI: Large: Collaborative Research: Com-

plementary Situational Awareness for Human-Robot Partnerships IIS-1327566, as well as the funding from Cochlear Corporation that supported portions of this work.

Thanks to the dissertation committee for reviewing and providing feedback on this work. It is a long work to review, and I am appreciative of your time.

Lastly, I have to give a tremendous thank you to Nabil. I was not a roboticist when I came to Vanderbilt, but I feel comfortable taking that label now. My abilities as a researcher and engineer have been revolutionized from where I was before entering the program. I learned greatly from your classroom knowledge, research supervision, and direct feedback. But moreover, your refusal to compromise research quality and to always insist on putting out exceptional work will stay with me for my entire career. I am especially grateful that you have been so clear on not approaching cutting corners on the ethics of responsible research and professional behavior. To have had an advisor produce such high quality research while also maintaining impeccable integrity has been a blessing and inspiration.

TABLE OF CONTENTS

LIST OF TABLES

LIST OF FIGURES

CHAPTER 1
INTRODUCTION

1.1 Motivation: Situational Awareness and Perception Augmentation in Surgery

The introduction of minimally invasive surgery (MIS) and robot-assisted minimally invasive surgery (RAMIS) have created many opportunities for enabling new surgical approaches that limit patient trauma, improve outcomes, or expand the set of possible capabilities compared to traditional open surgery. However, these new opportunities are also coupled with new challenges. Some challenges are mechanical: how to create physical systems capable of retaining surgical dexterity and large workspaces even when entering the body through small incisions or natural orifices. Other challenges are sensory: when a surgeon must operate a robot through telemanipulation, the basic sense of touch through haptic feedback is lost. Given that commercially available robotic surgical systems do not currently provide force sensing and haptic feedback capabilities, this presents a sensory barrier that complicates task execution when surgeons attempt to safeguard the anatomy against trauma during forceful interaction with tissue.

Some of these challenges are being addressed through works exploring new methods of intraoperative sensing to extract more information during surgery. This sensing problem is coupled to a broader category of perception deficit: in addition to the collection of raw information (i.e. interaction forces), there is the question of how to interpret these sensing signals and build surgeon perception. For example, if force sensing capabilities are added to a robot, how are those forces used to guide the surgeon's understanding of the environment interaction? The core questions of this research involve not only what sensory information to collect and how to collect it, but also how to use and convey that information in a way to maximise the surgeon's situational awareness of the environment and improve

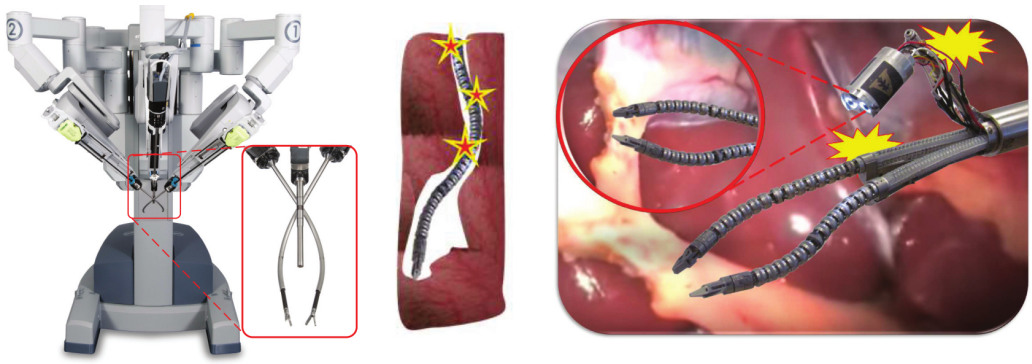

Figure 1.1: Left) da Vinci Xi system by Intuitive Surgical. Right) IREP surgical system with complex environment contact states outside the surgeon's field of view. Figure adapted from [1]

task execution and dexterity.

A concurrent development to the above is the desire for robotic systems to not merely replicate the abilities present in manual surgery but to augment surgeon capabilities to improve surgical execution and eventual patient outcomes. While the technical and regulatory barriers to achieving fully autonomous control are high, semi-autonomous control and guidance methods present a variety of methods for improving task-execution in RAMIS. To allow increased autonomy and semi-automated task execution, accurate surgical registration is required. Collecting sufficient information intraoperatively to register preoperative plans/information and update them for intraoperative guidance is an important step in this development.

Our group recently published a review on medical robotic technologies and the associated challenges in different kinds of surgical interventions [1]. In RAMIS, this work highlighted the need for and progress toward both perception and manipulation augmentation. For MIS systems as pictured in Fig. 1.1, it is common to have complex environment contact states that may not be visible through an endoscope. Imaging technologies such as MRI, CT, and ultrasound have allowed for better understanding of patient anatomy, while robotic solutions like the da Vinci or IREP have presented methods for improved manipulation through minimally invasive means while retaining high dexterity and intu-

itive control strategies, but maintaining a surgeon's awareness of the entire, increasingly complex, surgical scene is still a challenge.

The current limitations of robotic surgical systems in terms of dexterity, sensing, and perception motivate the broad aspects of this dissertation which comprise the key chapters of this work. The following is a brief review of relevant works in several areas related to surgical intervention, sensing and user feedback. This review helps establish the scientific gaps and the societal needs that have motivated this research.

1.1.1 Intraoperative Dexterity: Deep Reach into the Anatomy

One of key drivers for greater adoption of RAMIS has been the ability to provide enhanced distal dexterity, motion scaling and to offer deep reach of multiple instruments while avoiding the need for mastering the reverse kinematic mapping required during manual laprascopic procedures[4, 5, 6]. The da Vinci, ZEUS, and RAVEN surgical systems provided this baseline level of manipulation assistance, however continued demand for deeper reach into the anatomy through natural orifices or single port access have motivated new areas of research to overcome the limitations of multi-port robotic access with rigid tools limited to dexterous motion only at their distal tip.

One trend is the move toward even more minimally invasive surgical systems that allow natural orifice transluminal endoscopic surgery (NOTES) or single-port access (SPA). The single site da Vinci system allowed laparoscopic procedures to be performed through a single incision. A variety of other research platforms have been developed for minimally invasive or single-port access as reviewed in [7, 1]. These platforms represent a variety of design architectures, including embedded actuation in the joints, linkage-based systems, wire-driven systems, and those with continuum arms. Many of these systems use multiple arms for coordinated motion and often use distal wrists for enhanced end-effector dexterity.

Continuum structures for minimally invasive access have taken on a variety of forms for different applications, including actuated catheters, concentric tube robots, and multi-

backbone or wire-driven continuum robots [8]. These have been designed for applications including single-port surgery in the abdomen, transurethral, transoral, and transnasal surgery.[9, 10, 11, 12]

Additional systems have been presented to apply the benefits of RAMIS to different surgical domains, including microsurgery in a variety of anatomical areas. This requires the development of new robot architectures to provide high dexterity with end-effectors of the appropriate size and manipulators of the proper accuracy to fit particular applications. In the eye, sub-micron or micron-level accuracy systems have been created for telemanipulated access [13, 14], collaborative control [15], or handheld tremor reduction [16].

As the adoption of robotic assistance expands to encompass more additional surgical domains and approaches, new robotic architectures will be needed for the particular needs of the workspace size, required tools, dexterity, and manipulation accuracy presented by these applications. Chapter 2, contains a review of robotic systems that have been developed for middle ear surgery. Also, in Chapter 2 we build on previous results using a robotic platform for robot-assisted and image guided retinal microsurgery using optical coherence tomopgraphy[17]. This system is used to explore the possible benefits of a new approach to minimally invasive middle ear surgery while focusing on quantifying the reachable workspace using current manual tools and comparing it to when using a custom miniature continuum robot.

1.1.2 Sensing: Visualization and Intraoperative Perception Aids

During minimally invasive surgery, a key component to surgical perception is white-light visualization of the surgical scene and the ability of the expert surgeon to relate visual cues to pre-operative images and their own understanding of the anatomy. When interacting with the anatomy, surgeons must form their own situational awareness of the surgical site and the sequence of surgical steps that should be carried out. Surgeons must adapt their work to reflect the intraoperative scene, and they often rely on sensory cues in the form

of vision and forces of interaction with the anatomy. A review of the challenges facing surgeons in terms of surgical situational awareness was presented in [1, 18, 8] within the context of multi-port MIS and NOTES. In this review we include works focused on use of white-light imaging and use of *artificial* perception to offer complementary perception during surgery.

The sense of sight is one of the core ways that humans understand their environment and regulate task performance - this is especially true in MIS where the sense of touch is severely degraded and surgeons must rely on images from whatever visualization method is put into the patient minimally invasively. Due to the centrality of vision in performing these procedures, the methodology of obtaining visual feedback is extremely important. From cystoscopes to Hopkins rod endoscopes to stereo endoscopes with 3D visualization, technological developments in visualization have allowed more minimally invasive procedures and facilitated the use of finer instrumentation and robotic solutions under visual control. With these minimally invasive techniques, patients can benefit from reduced blood loss, scarring, infection rates, pain, and recovery times.

In endoscopically-guided procedures, the endoscope is often offset from the center of the working channel and can be occluded by tools intersecting with the field of view. In single-port systems, this is exacerbated by the close proximity of the vision system and the tools or robot arms. On top of this, continuum robots or other non-straight architectures may also have elbows that protrude outside the field of view and move in directions different from those commanded to the end-effector, causing undesired tissue interaction outside the visualized field.

Reiter and Allen [19] presented methods for visual tracking of the arms of the IREP single port system for when parts of the continuum arm may be occluded or outside the camera's field of view. Probabilistic roadmaps have been used to penalize motions blocking the view of an eye-in-hand camera [20] or to plan occlusion-free trajectories [21]. Others have looked at methods for redundancy-resolution of continuum robots for task completion

while minimizing occlusion of the field of view [22].

While surgeons have reported great utility in the stereo vision available with the da Vinci system, the lack of other sensory information is reportedly a challenge. Augmenting direct vision of the surgical scene with overlaid information or with other sensory modalities will be useful in providing surgeons with more information about the state of the environment. Furthermore, since vision feedback is a prerequisite for enabling the surgeons to operate, the use of visual cues to form artificial perception is an interesting research question. For example, visual tracking has been used to estimate applied forces during organ manipulation and overlay deformation maps on the surgical scene [23].

Within the context of this dissertation, we explore the use of intraoperative light-intensity as a means to estimate depth of insertion of cochlear implant electrode arrays. In Chapter 3 we propose this modality as a low cost approach to providing surgical perception augmentation and we explore the potential benefits of white-light imaging for guiding surgeons during manual insertion of electrode arrays in cochlear implant surgery. In Chapters 5 and 6, we explore the utility of sensory information overlay during teleoperation with the aim of reducing mental burden during surgery and improving surgical performance in tasks of force-controlled ablation, knot tightening, and organ palpation.

1.1.3 Sensing: Robot-Environment Interaction Forces

During RAMIS for soft-tissue surgery, a lack of sensing and control of environmental interaction forces can lead to worse surgical outcomes and adverse events that endanger patients' health. Excess forces applied to soft tissues can damage sensitive anatomy [24]. Improperly sutured organs can be damaged through limited bloodflow [25] or blood leakage due to loose suturing[26]. Due to these factors and surgeon feedback that the lack of haptic interaction control is detrimental to surgical performance, a number of studies have investigated various methods for sensing, regulating, and communicating robot-environment forces, finding force feedback useful in reinstating surgeons' ability to sense and control

forceful interactions [24, 27, 28, 29, 30, 31].

A number of different approaches have been used in collecting force sensing information during robot-environment interaction. A 2008 review [32] cataloged a variety of methods: strain gauges [33, 34, 35, 36, 37, 38], load cells [39], LVDT sensors [40], fiber Bragg grating [41, 42] and optical micrometry [43, 44]. Laparoscopic tools have been augmented with sensors in a variety of fashions [39, 45, 33, 46, 47].

Because of the challenges in integration of these sensors into largely disposable devices that must also be sterilizable, rugged, and not overly expensive, others have looked at acutation-level sensing for estimation of tip forces through actuator-level current monitoring [48, 49], strain gauges [34, 50, 37], pneumatic pressure monitoring [45, 51], or backbone loadcell forces [52, 53] with investigations into the use of dithering for improved estimation [54, 55]. There is still work to be done in the field before clinical adoption to address challenges in cost, sterilizability, or dealing with frictional and other uncertainties in indirect force estimation algorithms using actuation-level measurements.

Considering prior works, there are several questions that remain to be answered. First, if force sensing is present, how can this be used to augment surgical performance during force regulation and force-guided exploration tasks? And which methods of feedback are more or less effective? Furthermore, in the case where robot control may be partitioned between user control and semi-autonomous control, how would such semi-automation be beneficial compared to direct sensory feedback or augmented sensory feedback? In Chapter 5 we try to answer these questions while using continuum robots with online estimation of forces of interaction and then with the use of a traditional RAMIS system with a model-mediated controller in Chapter 6.

1.1.4 Haptic and Force Feedback During RAMIS Teleoperation

In open surgery, surgeons identify subsurface organ features through manual palpation of soft tissues [56], and the lack of haptic feedback to accomplish palpation or other force-

regulation tasks is known to be a major limitation of RAMIS [57, 58]. Due to this known limitation, investigation of haptics in robotics and RAMIS has continued on a number of different fronts and a number of literature reviews [59, 60, 61] have been conducted.

Haptic feedback has been studied in a variety of contexts, showing efficacy in increasing accuracy during task execution [62, 63, 64, 65, 66], decreasing task completion time [67, 68], and decreasing interaction forces [69, 70]. This has been applied to a variety of contexts: catheter insertion [71]; suturing [72, 73]; palpation [70]; keyhole neurosurgery [74]; needle insertion [75, 76].

Many previous works have investigated a variety of palpation methods for stiffness estimation from tool-interaction. Embedded sensor arrays have been integrated into probes to extract stiffness information [77, 78, 79, 80]. Others have used rolling probes across the surface of an organ [81] or discrete probing motions in a grid on top of an organ [53, 82, 83]. A telemanipulated continuum robot was used under force control to map environment stiffness and geometry in [84]. Dynamic excitation of tissue was used to estimate impedance parameters alongside a multi-resolution probing algorithm [85].

Once a method to measure forces or stiffnesses has been identified and used in a particular system, there are still open questions in the communication of that information to the user for effective understanding of the underlying data. Researchers have investigated visual, auditory, kinesthetic, and tactile feedback mechanisms to relay diverse types of data, including bending forces, grip forces, blunt dissection forces, or suture-tightening forces [86].

An important distinction in the classification of haptic interaction is the difference between kinesthetic and tactile feedback. The former relays forces to some device grasped by the user to transmit force information. The latter uses some form of cutaneous feedback display that can be palpated or felt with the fingers that can convey finer features than the raw interaction forces conveyed in kinesthetic feedback [86]. Research has been made in a variety of types of tactile feedback devices [70, 87, 88, 68] or "pseudo-haptic" displays

that use visual cues to convey the status of some haptic interaction feature [89, 90].

In kinesthetic feedback using telemanipulated devices, an important methodological question is the stability and transparency of the feedback scheme. Different control methods have been compared for perceiving object deformability [91], and many have investigated how to optimize for transparency while still guaranteeing stability. The 2-layer method in [92, 93] separates out a passivity layer from the transparency layer. This gives an absolute guarantee of stability by preventing the generation of "virtual energy"; the method has been used to magnify interaction forces for better sensitivity in detection of varying stiffness and changing interaction forces [94].

Haptic feedback alone, especially kinesthetic feedback for relaying end-effector forces, is insufficient for conveying the more complicated contact/interaction situations that may appear in a number of surgical scenarios. In the reaching into deep anatomy by continuum robots, contact may happen at more locations than purely at the end effector. In the identification of subsurface features, the ability to palpate and find the location of tumors, arteries, or other unseen anatomy, it may be useful to supplement pure force information with algorithmic identification of stiffness or other features that identify the location of these structures. Additionally, when dealing with virtual fixtures and other sources of force information, a lack of semi-automated assistance may lead to high cognitive load that may impede accurate and quick task execution. These challenges motivate the work in Chapter 6 which investigates multi-modality feedback and integration of semi-autonomous actions into RAMIS systems to relieve the mental and physical burden on the surgeon.

1.2 Motivation and Technical Gaps

Given the surgical needs and prior work commented on above, great progress has been made in visualizing the surgical field, sensing robot-environment interaction forces, and using those sensed forces for guiding haptic feedback methods and improved robot control. However, there remain a number of technological gaps that this research aims to fill.

This dissertation explores addressing the particular technical needs within a diverse set of medical applications and in a variety of anatomical contexts. These range from the Otologic space in middle ear microsurgery (Chapter 2) to cochlear implant insertion (Chapter 3) to single-port laparoscopic surgery (Chapters 4, 5, 6). The first investigation in middle ear surgery focused on manipulation assistance, but the lack of additional sensory information motivated additional investigations into perception augmentation in other domains. A subsequent investigation in cochlear implant insertion focused on collecting visual intraoperative data and assisting surgeons in task execution. Intraoperative assistance was then explored in robotic applications to show the utility of new force-sensing methods using continuum robots and to develop methods for organ exploration and task autonomy in RAMIS.

Middle Ear Deep Manipulation: The introduction of angled endoscopes allowed for better visualization of larger regions of the middle ear than would be able to be accessed with the traditional surgical armamentarium. These newly visualizable areas of the middle ear workspace may contain disease that should be removed, as in malignant skin growth in cholesteatoma. There is a need to reach these areas to remove this tissue, but the current rigid tools are unable to reach these areas.

Cochlear Implant Insertion Metrics: Cochlear implant insertion is a delicate procedure that is complicated by the lack of an ability to see the execution of implant insertion due to the inability to see into the cochlea during insertion. There is a lack of information on the metrics of how different surgeons perform insertions and how technique varies between surgeons and when a single surgeon performs an insertion multiple times on the same anatomy.

Cochlear Implant Guidance: Various (semi-)automated techniques have been proposed for assisting cochlear implant insertion, as well as for visualization of the inner ear. However, there are few investigations into the utility of low-cost assistance methods that do not change the fundamental surgical methods as found in current clinical practice.

Continuum Robot Palpation Assistance: The adoption of continuum robots for RAMIS has been proposed in a number of works due to their high dexterity and ability to reach into deep anatomy. However, due to their flexible nature, it is still a challenge to use them for forceful environment interaction tasks. This is especially the case when using these flexible systems to interact with soft anatomy as may be found in soft organ palpation.

Continuum Robot Intrinsic Force Sensing: A number of methods have been proposed to achieve force sensing in continuum robots – either through actuation load measurement (joint-level force sensing) or through imaging (indirect *ex-situ* force sensing) or embedded sensors (*in-situ* force sensing). Previously presented methods for joint-level sensing are insufficient to deal with estimation of forces for continuum robots in high-force contact with soft environments in the presence of large actuation line friction. This is characteristic of what may be found in clinically deployable systems which have more frictional uncertainties than some of the research platforms presented in the literature.

Telemanipulation Feedback: When operating in contact with the anatomy and desiring to regulate interaction forces, there is a lack of established methods for user assistance. In scenarios like exploratory palpation and force-regulated dissection or ablation, surgeons must control and measure forces during soft organ interaction. Currently, clinically available laparoscopic systems do not have force feedback capabilities, and the question of how to achieve forceful interaction tasks without greatly increasing cognitive load is still an open question.

1.3 Key Contributions

Given the above technical gaps and clinical motivations, this thesis presents a number of contributions aimed at filling those gaps and providing new techniques and methods for addressing the above problems.

Middle Ear Deep Manipulation: A study was carried out to evaluate the feasibility of dextrous robotic solutions to allow deeper access into the middle ear to match the visual

capabilities with new manipulation techniques. The system was able to reach large areas of the workspace unable to be reached through traditional tools. The newly developed system allowed for access to a broader workspace than the current surgical tools with slower manipulation speed but higher accuracy than handheld tools. This study points towards the potential of robotic tools for greater reach and more accurate disease resection that could lead to better hearing outcomes and less re-resection in treating diseases in the middle ear.

Cochlear Guidance and Technique Measurement: A novel tool for imaging the cochlea was developed that allowed for intraoperative visualization of cochlear anatomy and tracking methods were developed to allow visual segmentation of clinically relevant parameters and guidance for instrument guidance for more repeatable clinical performance. Data was taken that helped establish a baseline for variability in cochlear implant insertion both between surgeons and among a single surgeon's repeated procedures.

Continuum Robot Palpation and Force Sensing: A control algorithm and accompanying palpation techniques were developed and validated on a single port access continuum robot for soft organ palpation and registration. The same system was used for the development of improved methods for force sensing that account for actuation uncertainty via a new modeling formulation that better accounts for uncertainties from hysteresis and a method to update model parameters for increased sensing accuracy. This work has enabled better exploration and interaction capabilities applicable to a broad set of continuum robotic platforms.

Forceful Telemanipulation Assistance: A user study was carried out to compare teleoperated task execution with a variety of feedback methods. Specific methods for robot-environment forceful interaction were investigated. The use of a model-mediated teleoperation framework allowed for better force regulation and more comfortable forceful exploration than simple feedback methods. Model-update methods are presented to allow for independent force regulation during model-mediated telemanipulation.

1.4 Outline

This work is organized as follows: Chapter 2 presents the design and evaluation of a robotic platform for middle ear interventions to match manipulation abilities with the visualization capabilities developed through angled endoscopes. A visualization and tracking/guidance system for cochlear implant insertion guidance is presented in Chapter 3. In the above works, the problem of forceful environment interaction, a major stumbling block to full integration of assistive technologies in RAMIS, was not explored. Therefore, forceful environment interaction strategies for continuum robots are presented in Chapter 4. This is extended to work which integrates force sensing into the continuum robot without the use of external force sensors in Chapter 5. Alongside the specific contributions in continuum robots, a user study was designed and carried out for evaluating user feedback methods for forceful interaction in the control of articulated robotic surgical systems, as described in Chapter 6. Lastly, Chapter 7 concludes with a summary of the work in this thesis and the avenues for future work.

CHAPTER 2
INSPECTION AND TOOLS FOR DEEP ACCESS TO THE MIDDLE EAR

2.1 Overview

Middle ear surgery presents unique challenges because of the constrained operative space and limited access to certain anatomic regions. Angled endoscopes have increased the ability to visualize more of this space, but the traditional surgical armamentarium has been unable to manipulate in the spaces that have become newly visualizable. We hypothesized that the use of a robotic manipulator with a dexterously orientable gripper would expand the ability of middle ear surgeons to perform precise tasks and access otherwise challenging anatomic regions.

We developed a custom-designed robot with a sideways-reaching gripper to evaluate feasibility of manipulation tasks in different middle-ear anatomical zones. Reachable workspace within the middle ear, accuracy of free-space path following, and tool steadiness were compared between robotic telemanipulation and manual control. Preliminarily assessments of the robot's clinical utility included: 1) touching the round window niche, Eustachian tube orifice, and sinus tympani; 2) placing a stapes prosthesis; 3) removal of mockup diseased tissue in the sinus tympani.

2.2 Medical Background

As RAMIS applications have expanded, most prominently in laparoscopic surgery with the use of the da Vinci surgical system, other robotic manipulators have been proposed in the literature in a variety of surgical fields from orthopedics to urology. Middle ear surgery is a field ripe for expansion of robotics because of the particular demands related to surgical technique. With the advent of endoscopic ear surgery, visualization of certain middle ear regions has been greatly enhanced [95]. However, because of the constraints of the ear

canal that are imposed on rigid tools, accessing these areas with currently available surgical instrumentation remains a significant challenge. This challenge presents an opportunity to introduce new robotic manipulators designed specifically for this anatomical region.

Several groups have already investigated the benefits of using robots for middle ear surgery. Rothbaum et al.[96] and Brett et al.[97] have investigated the use of a robotic drill for stapedotomy footplate fenestration. Miroir et al. created a prototype system for middle ear surgery, dubbed the RobOtol [98, 99] that allowed access to the middle ear through the ear canal with rigid tools. Further investigation [100] by the same group resulted in a surgical simulation environment for practicing the use of the robotic system within a simulated ear environment. Anticipating robotic instrumentation in the middle ear, a training system for teleoperated tasks has also been developed [101].

This work differs from prior investigations into robotics for middle ear surgery in that the prototype robotic system was designed to be capable of providing distal dexterity within the confines of the middle ear. The presented system is able to reach sideways once in the middle ear by the use of a retractable, curved gripper that allows surgeons to access anatomy that is visualizable with angled endoscopes, but difficult to reach with current instrumentation. Accordingly, the goal of this research is to explore the capability of the robotic system to access regions of the middle ear that would otherwise be difficult to reach with current tools, and to compare motion precision between manual and robotic tools. This design can facilitate dexterous manipulation within hard-to reach anatomical areas of the middle ear and if used to treat patients with cholesteatoma, abnormal skin growth within the middle ear, this technology may help increase the coverage of disease removal and potentially better preserve ossicles during resection. [102, 103]

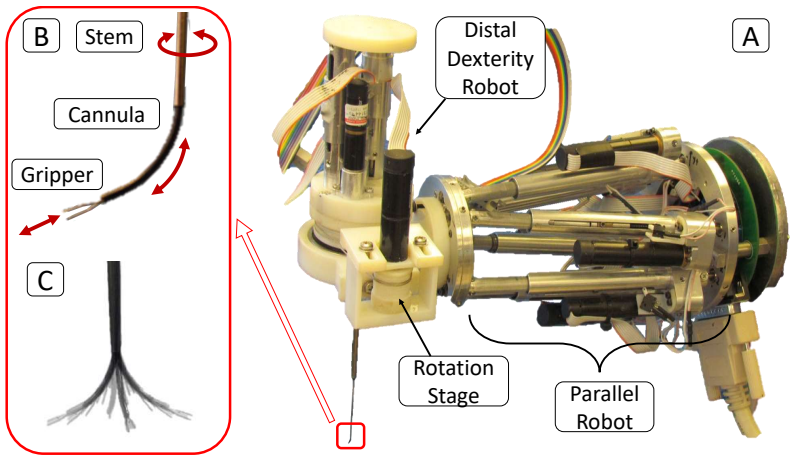

Figure 2.1: Robotic System Overview (A) Parallel robot, distal dexterity robot and rotation stage; (B) the stem, cannula and gripper; (C) a representation of the workspace of the gripper as it is extended and rotated.

2.3 Methods And Materials

2.3.1 Robot Architecture

A hybrid parallel-serial robot was designed to allow access into middle ear anatomy. The robot is composed of two modules connected in series, a custom-designed 6 degree of freedom (DoF) parallel robot and a two DoF distal dexterity robot (DDR). These systems have the same kinematic structure and geometry as detailed in Yu et al.[104] The modules are connected by a 1 DoF rotary axis, resulting in a 9 DoF robot which can be seen in Fig. 2.1A.

The parallel robot is a Stewart/Gough Platform [105, 106]. By changing the length of six struts supporting the moving platform, the position and orientation of the moving platform are controlled in 6 degrees of freedom. Because of the limited orientation workspace of the platform, an additional rotation stage was added to allow the DDR to spin about the longitudinal axis of the tool as shown in Fig. 2.1B. This rotation stage was made of 3D printed ultraviolet cured resin (VeroWhite, Stratasys Inc.) and actuated by an additional motor with a wire-driven transmission.

The DDR makes this work unique by allowing the robot to reach sideways while manip-

ulating within the middle ear. Fig. 2.1B shows the gripper in its extended configuration, and a representation of a range of gripper configurations is shown in Fig. 2.1C. The gripper was constructed from an ophthalmic tool and is attached to a long wire encased by a slightly larger tube. When the gripper is pulled back into the tube, the jaws are forced closed, closing the gripper. The tube is a 0.65 mm superelastic nitinol tube that has been shape set to have a bend at its tip with a radius of 7.5 mm which acts as an orientable cannula.

This cannula allows the robot to access areas of the anatomy unreachable with straight tools. The cannula is surrounded by a stainless steel stem; retracting the cannula into the stem straightens the cannula. When the cannula is fully retracted, the gripper points straight along the axis of the tool, whereas when the cannula is fully extended, the gripper is oriented at the end of a 7.5mm radius bend. By retracting and extending the tube and spinning the DDR about its longitudinal axis, the gripper can act as a straight tool or reach a variety of areas deep in the anatomy. The gripper and cannula are actuated by two motors with leadscrews on the top of the DDR.

2.3.2 Telemanipulation Architecture

Because there are kinematic redundancies in the 9 DoF robot architecture, some method must be used to resolve how to control the end-effector motion and that of the redundant actuators. One option would be to use 6 DoF end-effector control with some form of automated redundancy resolution method, however the differences in speed and accuracy between the parallel robot and DDR make this approach cumbersome. Instead, a partitioned approach was undertaken that gave the user full control over the robot's motion.

The frames and nomenclature for the presented approach method are shown in Table 2.1. The telemanipulation framework is separated into two pieces: the first is the control of the rotation stage and the parallel robot to form one 7 DoF robot. The remaining 2 DoF in the DDR are controlled independently, precluding the ability to simultaneously control all 9 DoF, but allowing for sequential control of the DDR and the 7 DoF robot. Users controlled

the device using an Omega.7 haptic device from Force Dimension (Lyon, Switzerland) and a pair of footpedals - a telemanipulation pedal and a DDR control pedal.

Symbol	Description
${}^{a}\mathbf{H}_{b}$	Homogeneous transform which transforms a point in frame {b}, ${}^{b}\mathbf{h}$, to a point in frame {a}, ${}^{a}\mathbf{h}$, via the relationship ${}^{a}\mathbf{h} = {}^{a}\mathbf{H}_{b}\ {}^{b}\mathbf{h}$
${}^{a}\mathbf{R}_{b}$	Rotation matrix that rotates some vector in frame {b} to frame {a}
${}^{a}\mathbf{p}_{c}$	Vector c as observed in frame a
$\{o\}$	Frame of the Omega.7 master device
$\{m\}$	Frame of the master device handle
$\{w\}$	Robot world/base frame
$\{p\}$	Frame of the robot's moving platform
$\{t\}$	Frame of the robot tool tip

Table 2.1: Frames and transformations used in middle ear telemanipulation framework

Fig. 2.2 shows the overall telemanipulation architecture used for the 7 DoF robot. When the telemanipulation footpedal was not pressed, the robot's desired position was held constant, and when pressed, the robot followed the user's movement on the Omega.7 master device.

When a user pressed the telemanipulation pedal, the "Telemanipulation" block in Fig. 2.2 became active. On the press event, the controller saved the homogeneous transform of the current master pose, ${}^{o}\mathbf{H}_{m}^{0}$ and tool pose, ${}^{w}\mathbf{H}_{t}^{0}$. These were used to calculate the desired tool pose, ${}^{w}\mathbf{H}_{t}^{des}$, as the user moved the master during a given footpedal press. *A priori* knowledge of the rotation, ${}^{o}\mathbf{R}_{w}$, between the frame of the Omega.7, {o}, and the robot world frame, {w}, was assumed.

While the pedal was pressed, the desired orientation (${}^{w}\mathbf{R}_{t}^{des}$) and position (${}^{w}\mathbf{p}_{t}{}^{des}$) that form ${}^{w}\mathbf{H}_{t}^{des}$ were calculated as:

$$ {}^{w}\mathbf{R}_{m} = {}^{w}\mathbf{R}_{o}\ {}^{o}\mathbf{R}_{m}\ {}^{o}\mathbf{R}_{w} \tag{2.1} $$

$$ \Delta{}^{w}\mathbf{R}_{m} = \left({}^{w}\mathbf{R}_{m}^{0}\right)^{T}\ {}^{w}\mathbf{R}_{m} \tag{2.2} $$

$$ {}^{w}\mathbf{R}_{t}^{des} = {}^{w}\mathbf{R}_{t}^{0}\ \left(\Delta{}^{w}\mathbf{R}_{m}\right) \tag{2.3} $$

$$ {}^{w}\mathbf{p}_{t}{}^{des} = {}^{w}\mathbf{R}_{o}({}^{o}\mathbf{p}_{m}{}^{cur} - {}^{o}\mathbf{p}_{m}{}^{0}) + {}^{w}\mathbf{p}_{t}{}^{0} \tag{2.4} $$

This was used to calculate the updated tool pose. Because of the redundant nature of the task, some adjustments were made to the above "standard" telemanipulation framework. First, motions from the master were filtered such that:

$$^{o}\mathbf{R}_{m} = Rotx(\theta_a)Roty(\theta_b) \tag{2.5}$$

Where θ_a and θ_b are the angles of rotation of the proximal angles of the Omega.7 haptic device - this ignores rotation of the third axis of the Omega.7, meaning that the master was nominally only controlling 5 DoF of the robot. *Rotx* and and *Roty* are defined as:

$$Rotx(\gamma) = \begin{bmatrix} 1 & 0 & 0 \\ 0 & \cos\gamma & -\sin\gamma \\ 0 & \sin\gamma & \cos\gamma \end{bmatrix} \tag{2.6}$$

$$Roty(\gamma) = \begin{bmatrix} \cos\gamma & 0 & \sin\gamma \\ 0 & 1 & 0 \\ -\sin\gamma & 0 & \cos\gamma \end{bmatrix} \tag{2.7}$$

The third axis of the Omega.7, θ_c, was used to directly control the rotational stage. Similar to the above framework, when the telemanipulation footpedal was pressed, the current angle of the third axis, θ_c^0, and the current angle of the rotational stage, θ_7^0, were saved. Then, the desired angle of the rotation stage was set as:

$$\theta_7^{des} = (\theta_c - \theta_c^0) + \theta_7^0 \tag{2.8}$$

The rotational stage was then controlled by a low level PID controller.

Trajectory generation: Because a user's hand could move rapidly and abruptly change the desired pose of the tool, a trajectory planner was implemented to not feed $^{w}\mathbf{H}_{t}^{des}$ directly into the low level joint controller. This also was used to implement a secondary control

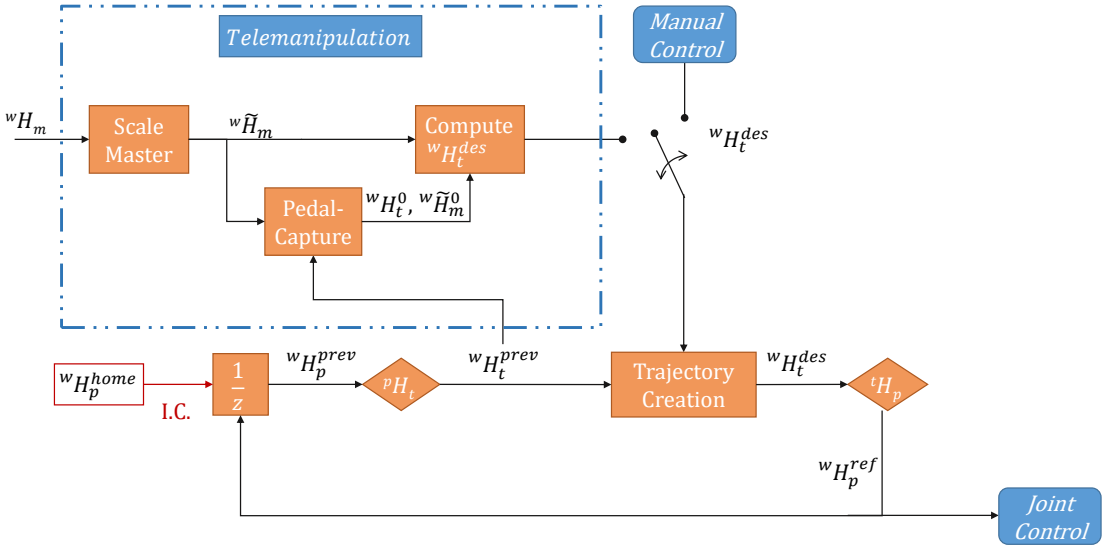

Figure 2.2: Teleoperation method for parallel robot with rotational stage

mode using the "Manual Control" input in Fig. 2.2, which allowed a user to programmatically input desired poses to the robot.

First, a world frame definition of the differential rotation between the tool pose at the previous time step and the desired tool pose was calculated as:

$$\Delta\mathbf{R} = {}^{w}\mathbf{R}_{t}^{des}({}^{w}\mathbf{R}_{t}^{prev})^{\mathrm{T}} \tag{2.9}$$

This was decomposed into an axis-angle formulation:

$$\Delta\theta = \cos^{-1}\left(\frac{trace(\Delta\mathbf{R})-1}{2}\right) \tag{2.10}$$

$$\boldsymbol{\nu} = \frac{1}{2\sin(\Delta\theta)}\begin{bmatrix}\Delta R(3,2)-\Delta R(2,3)\\ \Delta R(1,3)-\Delta R(3,1)\\ \Delta R(2,1)-\Delta R(1,2)\end{bmatrix} \tag{2.11}$$

Where ν represents the rotation axis of the rotation and $\Delta\theta$ the angular error. A scaling

factor α_o for orientational velocity was defined as:

$$\alpha_o = \begin{cases} 0, & if \Delta\theta < \varepsilon_o \\ \frac{\Delta\theta}{\omega_{max}}, & if |\frac{\Delta\theta}{\omega_{max}}| < 1 \\ 1, & otherwise \end{cases} \tag{2.12}$$

Where ε_o is the smallest angular error desired and ω_{max} is the maximum orientational velocity. This was used to scale the desired angular velocity as:

$$\omega_{sdes} = \alpha_o \, \omega_{max} \, \nu \, dt \tag{2.13}$$

The instantaneous rotational velocity can then be found

$$\Omega = [\omega_{sdes}]_x \tag{2.14}$$

$$\dot{R} = \Omega^w \mathbf{R}_t^{prev} \tag{2.15}$$

where $[*]_x$ the cross product matrix of a vector. Scaling of the positional velocity was taken care of in a similar way:

$$\delta p = \|t_{des} - t_{prev}\| \tag{2.16}$$

$$\delta \hat{p} = \frac{t_{des} - t_{prev}}{\delta p} \tag{2.17}$$

$$\alpha_p = \begin{cases} 0, & \delta p < \varepsilon_p \\ \frac{\delta p}{v_{max}}, & \frac{\delta p}{v_{max}} < 1 \\ 1, & otherwise \end{cases} \tag{2.18}$$

$$\dot{p} = \alpha_p v_{max} \delta \hat{p} dt \tag{2.19}$$

Where ε_p and v_{max} are the minimum desired positional error and maximum Cartesian

velocity. Once $\dot{R}$ and $\dot{p}$ are found, the reference transformation was set as:

$$R_{ref} = R_{prev} + \dot{R} \tag{2.20}$$

$$p_{ref} = p_{pref} + \dot{p} \tag{2.21}$$

$${}^{w}\mathbf{H}_{t}^{ref} = \begin{bmatrix} R_{ref} & p_{ref} \\ \mathbf{0} & 1 \end{bmatrix} \tag{2.22}$$

The tool reference frame ${}^{w}\mathbf{H}_{t}^{ref}$ is then multiplied by the tooltip-to-moving-platform transformation ${}^{t}\mathbf{H}_{p}$ to find the homogeneous transformation of the pose of the moving platform ${}^{w}\mathbf{H}_{p}^{ref}$. Knowing the reference pose of the moving platform, a simple inverse kinematic solution was used to find the corresponding joint lengths for all the joints of the parallel robot. These were fed into a low-level PID controller.

2 DoF DDR Control: The DDR footpedal was used to command cannula action, independent of telemanipulation of the 7 DoF robot. When the DDR pedal was pressed, the gripper of the Omega.7 was used to control the gripper of the robot and the pitch joint of the Omega.7 was used to control the extension of the cannula using the same relationship as (2.8). Telemanipulation of the robot was disabled when this footpedal was pressed.

2.3.3 Tool-Robot Comparison Experiments

The experimental setup can be seen in Fig. 2.3 where the surgeon is seen seated with the temporal bone, endoscope, haptic control device, robot, and a screen in front of him. The ear canal skin and tympanic membrane were removed from the cadaveric bones. Although this provides greater access to the middle ear than in most clinical scenarios, the physicians performing this research routinely elevate the tympanic membrane off the malleus during chronic ear surgery, therefore the operative exposure is not drastically different.

To evaluate differences in reachable areas, the workspace of the robot's extendable cannula was compared to that of a curved manual tool. A Rosen needle was chosen for the

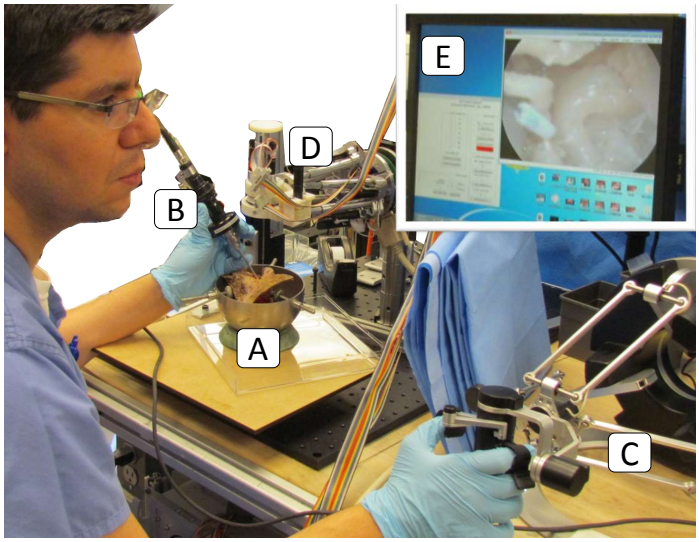

Figure 2.3: Experimental Setup - The surgeon was seated in front of a pre-prepared temporal bone (A) with endoscope (B) and master telemanipulation device (C) in his hands which controlled the robot (D). Visualization of the endoscope view was available on a monitor (E) along with the robot control user interface.

manual tool, as it can be used in tasks that require both in-line and curved manipulation. Optical tracking markers were attached to the back of the needle and the top of the robot as well as to a standard bone-specimen holder to track the position of the tool tip and robot gripper relative to the bone, as pictured in Fig. 2.4. The needle and robot were used to trace the edges of the reachable area within the bone to characterize the size of the workspace. The tympanic ring was used as a cut-off plane for the experiment: points lateral to the plane of the tympanic ring were not included in the workspace evaluation. A H40 MicronTracker optical tracking system with 15Hz measurement rate and 0.14mm RMS target jitter was used for acquiring the 3D positions of the markers (ClaroNav).

To choose a robot control method and compare robot performance with manual tool use, surgeons tested different robot control techniques and manual tools in free space. Surgeons were asked to follow a square path on a piece of 1 mm spacing grid paper with the tip of the gripper 10 times. Using standard color-thresholding image processing techniques, the location of the tool tip was identified in videos of the experiments. Tracking error was calculated as the distance in mm to the closest point on the square path in all frames of the

video. Results were compared between three user-control strategies.

Two fellowship trained neurotologists carried out the line-tracing experiments. The first user control strategy was a manual approach simply holding a straight pick in hand: the current standard for middle ear operation. The second approach utilized a "collaborative control" scheme. The surgeon steered the robot by manipulating the DDR grasped in his hand. A force sensor attached at the base of the DDR commanded the robot to actively move with the forces applied by the user. In the third method, the robot was telemanipulated using the Omega.7 haptic device to move the robot. The telemanipulation scheme included motion-scaling to allow the user to make finer, more precise movements. The results of this experiment, detailed below, did not show a difference in control accuracy between telemanipulated and collaborative control schemes, but to allow users to command all 9 DoF of the system in a single interface, the telemanipulated scheme was used for the remaining experiments.

In addition to the comparison experiments outside the bone, tool steadiness was compared in a temporal bone between manual control of the Rosen needle and robotic control of the gripper. The needle and robot were equipped with optical tracking frames in the same method as during the workspace experiments (Fig. 2.4). An accelerometer (Bosch BNO055) was attached to both tools to better measure dynamic movement.

To test tool steadiness in static tasks, a non-surgeon user was asked to hold the tooltip of the Rosen needle and the robot at a fixed location. Tooltip steadiness for the static task was calculated as the average radius of the point cloud representing all tool tip positions captured by the MicronTracker, with a smaller radius indicating increased steadiness. Five trials were carried out for both the needle and robot with a length of 40 seconds per trial.

To test tooltip steadiness during dynamic motion tasks, a surgeon touched the stapes capitulum and then exited the bone using both the needle and the robot. This was repeated six consecutive times per trial and repeated in five trials for a sample size of 30 motion paths. For this dynamic motion task, steadiness was calculated as the average tooltip

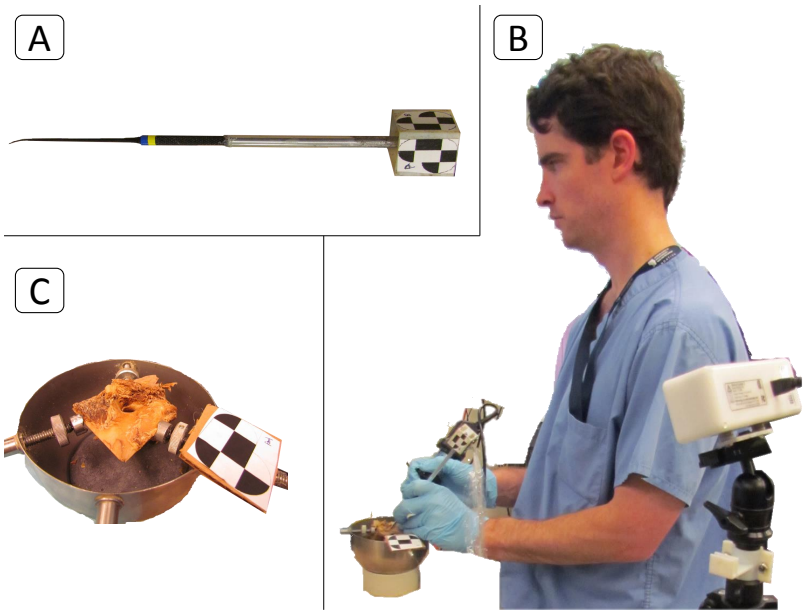

Figure 2.4: Tool Tracking Setup - (A) Rosen needle equipped with optical tracking marker for tip tracking; (B) Surgeon performing stapes touch experiment with bone, tool, endoscope, and MicronTracker; (C) Temporal bone specimen with optical tracking marker affixed to bowl.

deviation from a smoothed tooltip path: a smaller deviation relating to increased tool steadiness. The smoothed path representing intentional motion was extracted using all movements associated with frequencies smaller than 1 Hz. This cutoff frequency was chosen by inspecting the Fourier transform of the tooltip acceleration obtained from the accelerometer. There were two clusters of signal power around 0 Hz and around 5-10 Hz, so filtering at 1 Hz separated low frequency intentional motion from high frequency unintentional motion.

2.3.4 Temporal Bone Feasibility Experiments

The robot was used in a number of feasibility tasks in temporal bones to assess the workspace of the system and capability to accomplish surgical tasks. As a proof of feasibility for use of this system in eradicating cholesteatoma and accessing hard-to-access regions of the middle ear in patients with intact ossicles, the user touched the tips of the gripper to the Eustachian tube entrance, the round window region, and the sinus tympani

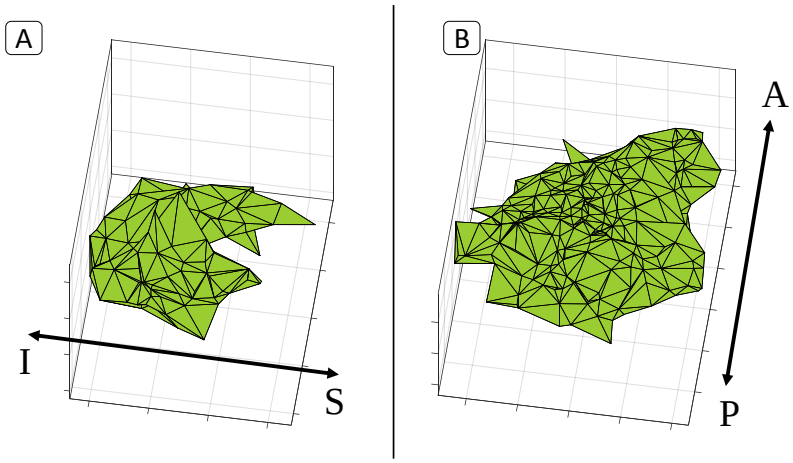

Figure 2.5: Workspace Comparison - (A) shows the size of the manual tool's workspace within the middle ear compared to (B) the robot's workspace with the extendable cannula. I, S, P, A denote inferior, superior, posterior, and anterior directions, respectively.

in three temporal bones.

The robot was then used to perform a series of clinically relevant surgical tasks within the middle ear. The first task was the ability to place a nitinol stapes piston prosthesis (Grace Medical, Memphis TN). This was chosen as it was felt to be a challenging manipulation task. The second task was the removal of mockup disease tissue from the sinus tympani. A small piece of paper was coated in glycerin and inserted into the sinus tympani. The robot's gripper was used to grab and remove this foreign body.

2.4 Results

In evaluating the workspace of the robot and the manual tool, the robot demonstrated a much larger workspace due to the use of the extendable cannula, Fig. 2.5. Specifically, the manual tool had an estimated total workspace of 430 mm^3, whereas the robot had an estimated workspace of 1960 mm^3 (an increase in reachable area of 355%).

Micro-manipulation with our robotic system was associated with reduced tracking errors when compared to manual manipulation. Following the line-tracing procedure outlined in section 2.3.3, manual manipulation (0.14mm) had a larger average tracking error when compared to the cooperative (0.09mm) and telemanipulated (0.09mm) modes. The stan-

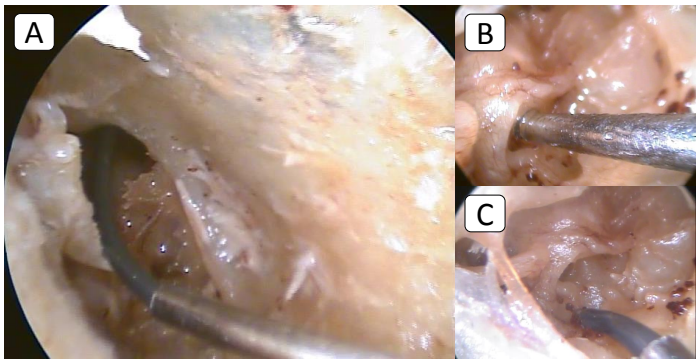

Figure 2.6: Robotic Anatomy Access - Using the curved cannula, the robot gripper is seen touching (A) the entrance of the Eustachian tube; (B) the round window; (C) the sinus tympani.

dard deviation of the error in the manual mode (0.13mm) was also larger than that of the telemanipulated (0.09mm) and cooperative modes (0.09mm).

Experiments in the middle ear also showed increased tool tip steadiness when using the robot. In a 40 second static steadiness experiment with no desired movement, manual tool use exhibited a mean norm deviation of 2.24 mm compared to 0.81 mm using the robot ($p < .001$). The mean norm of tool tip deviation during a dynamic experiment touching the stapes was 1.85 mm for the manual tool compared to 1.44 mm of average deviation using the robot ($p < 10^{-6}$). However, the robot was slower in completing the task: the average time to carefully touch the stapes and remove the tool was 7.23 seconds manually compared to 14.27 seconds for the robot ($p < 10^{-8}$).

In regard to feasibility tasks, the DDR was able to successfully access anatomy in the periphery of the middle ear without injury or manipulation of the intact ossicular chain. Specifically, the DDR forceps were used to touch the Eustachian tube orifice (Fig. 2.6A), the round window membrane (Fig. 2.6B), and sinus tympani (Fig. 2.6C) with ease in 3 separate temporal bones. The ability of the DDR to place a stapes piston prosthesis in a stapedotomy and onto the incus was assessed. A 4.5 mm piston prosthesis remained stable in the retractable gripper throughout the procedure, and placement in the stapedotomy and onto the incus was achieved (Fig. 2.7). The ability of the DDR to grasp and remove foreign

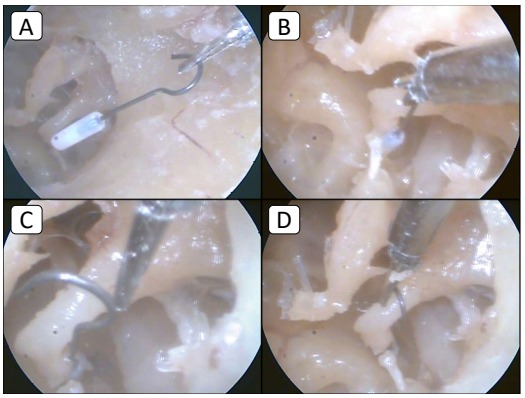

Figure 2.7: Stapes Prosthesis Placement - A basic grasp of the prosthesis with the robot is seen in (A), the placement of the prosthesis is pictured in (B), and fine adjustment of the prosthesis placement is pictured in (C) and (D).

materials/undesirable disease from the sinus tympani was achieved and proved feasible.

2.5 Discussion

This robotic system expands on prior works on middle ear robotic surgery by offering steerable tools with distal dexterity suitable for the confined space of the middle ear. The results demonstrate the ability of our robotic system to perform with better tracking and more steady motion than manual manipulation. This has significant clinical implications in regards to middle ear surgery. Given the small space of the middle ear combined with the need to manipulate delicate structures in an anatomically sensitive region, greater control of the operating instrument is desirable.

The robot was chosen to be telemanipulated for the experiments inside the middle ear after preliminary experiments showed no difference in gross motion accuracy between cooperative control and telemanipulated control. However, the cooperative control method did not allow surgeons to control additional DoF easily in the same interface and was more difficult to use when performing tasks with both positional and orientational control. This is something to keep in mind for future developments - the increased number of DoF prevented easy control through a collaborative interface without an intuitive method for redundancy resolution. The use of telemanipulation is also expected to reduce the burden

on the surgeon from an ergonomic standpoint by removing the need to stabilize the surgical tools while holding a specific posture over the patient and allowing the surgeon to sit in a comfortably designed telemanipulation environment without worrying about tool position except at the gripper tip.

The use of a parallel robot has a number of advantages over prior work using serial manipulators for middle ear surgery. First, the robot is able to carry large loads for its weight and is much stiffer than a comparable serial robot. The largest drawback of parallel architectures is the robot's small workspace which has been mitigated by an additional actuator that allows the DDR to spin around the gripper's main axis. Other than this, the workspace does not need to be enlarged because the middle ear is a relatively small area and large gross motion is not needed to access all areas of the relevant anatomy.

The system was shown to be able to reach anatomic regions of the middle ear which can be challenging to access with available tools. With the introduction of endoscopes, visualization of these regions is enhanced, but manipulation of sites such as the posterior recesses and Eustachian tube orifice remains difficult. As seen from our reachable workspace evaluation, the robot increases the space reachable inside the inner ear by 355%. The ability to reach regions in the periphery of the middle ear space, as demonstrated by this research, would be useful for a variety of middle ear procedures. Specifically, improved removal of cholesteatoma from these regions could potentially impact preservation of ossicles, recurrence rates and the need for second look procedures. This is speculative at the current time, but the robotic steerable gripper is promising and the use of dexterous robotic end effectors in middle ear surgery still should be further explored.

Lastly, this new method of access will provide the opportunity for surgeons to attempt interventions that are currently difficult to realize. As an example, access to the Eustachian tube may improve the ability of surgeons to insert balloons or remove lesion on the interior of the Eustachian tube through the middle ear. Further, the ability to access and manipulate tissue within the sinus tympani, as demonstrated herein, would have significant clinical

applications in surgery for cholesteatoma. While the endoscope can now provide visualization of these areas, disease removal from the posterior recesses remains challenging.

Important to note is that one potential source of error in the workspace calculation is that measurements were made at the top of the robot, as it is impossible to attach optical markers to the tool tip and visualize inside the ear. This means that the position of the tip is calculated based on a model of the robot's geometry and not measured in real-time. Therefore, if the stem of the cannula was bent during experiments, results would be inaccurate. While care was taken to prevent this from occurring, it is possible that there could be some distortion of the data due to bending of the stem.

2.6 Limitations and Considerations for Future Work

While the removal of the mockup disease was successful, visualization proved difficult due to the position of the robot above the workspace. This suggests that a future design of the robot should minimize bulk above the middle ear and/or incorporate visualization tools in its design. The use of the gripper without stereo vision or haptic feedback was difficult. Future developments would need to include better feedback modalities for enhanced usability.

The strength of the ophthalmic gripper used in this prototype design is another potential area needing improvement. While the right size for an instrument to be used in the middle ear and able to hold a prosthesis without difficulty, it is likely that the grasping force will be insufficient for the higher forces needed in removal of tissue when treating cholesteatoma.

The future of robotics in the middle ear depends on a variety of implementation factors in addition to the questions of technical feasibility which were started to be addressed in this work. Studies in various surgical domains have found robotic approaches to significantly increase cost, decrease cost, or to not have significant results [107, 108, 109]. The costs of robotic surgery compared to manual surgery depend heavily on the particular benefits of robotics in a given type of intervention and if outcomes, procedure time, or length of

hospital stay are affected. Cost can even increase further if training is required, particularly when using a new robotic system, as such systems will have a steeper learning curve [110]. Ultimately, the cost-effectiveness of robotics in the middle ear will depend on changes in operative time and outcomes associated with a clinically deployed system. If clinical outcomes can be improved and repeat surgeries can be avoided through the use of robotic technology, such systems may have a widespread adoption. The ability to comprehensively remove cholesteatoma from the entire middle ear cleft will potentially be possible with robotic systems such as the one described herein; however, a more robust system and further tests will certainly be required to achieve this goal.

This work is a preliminary first step intended to demonstrate the potential feasibility of robotic approaches in the middle ear space. In order to fully improve the ergonomics of middle ear surgery through use of telemanipulated tools, additional components will need to be developed to position an endoscope during surgery and collision avoidance methods will need to be developed. In addition, the workspace of the robot has not been optimized - the bending angle of the cannula is suitable for reaching relevant anatomy, but future work should explore optimal design of the bent curvature in order to best cover all relevant anatomy within the middle ear while avoiding environment collision. Collision avoidance can be achieved via registration to preoperative scans or the incorporation of haptic feedback to the user based on robot force sensing. Sterilizability, rapid deployability, and similar concerns necessary for clinical realization have not been addressed with this current work - future work will need to be done to make a truly translational system.

2.7 Conclusion

This investigation demonstrated that robotic assistance allows surgeons to access challenging regions of the middle ear with an increased workspace compared to simple manual tools. Coordinated and accurate manipulation was evidenced by motion analyses which compared favorably to manual manipulation. The completion of feasibility tasks within the

middle ear showed the robot is able to perform clinically relevant tasks such as reaching the sinus tympani, placing a stapes prosthesis and removing mock-up disease from the posterior recesses.

The reachable workspace in the middle ear was considerably greater with the robot as compared to manual manipulation using a Rosen needle. In a simple path tracing task outside the ear, robotic telemanipulation was associated with significantly reduced error. Within the middle ear, the robot contributed to steadier movement, but longer task completion time. The gripper successfully placed a 4.5 mm piston prosthesis, accessed the round window niche, Eustachian tube orifice, and removed mockup disease from the sinus tympani.

The lack of haptic feedback and the overall nonintuitive user interface of holding an endoscope with one hand while using a master device in the other made this system difficult to control and use, especially during any sort of robotic task dealing with forceful interaction. This was exacerbated by the low grasping capabilities of the gripper. This points the way for future needed developments not only in improved designs for robots than can combine visualization control with manipulation control, but with interfaces and data collection that allow for more intuitive user control with force information conveyed to the user.

CHAPTER 3
INSPECTION AND GUIDANCE TOOLS FOR COCHLEAR IMPLANT INSERTION

Cochlear implants are used to treat severe to profound sensorineural hearing loss. Proper placement of the electrode array (EA) inside the cochlea is required for effective stimulation of the auditory nerve and for reducing intracochlear trauma during implantation. Reduction of intracochlear trauma can preserve functioning hair cells in patients with residual hearing. However, because the bony structure of the cochlea prevents direct surgical visualization, it is technically challenging to ensure proper placement of the EA - leading to intracochlear trauma and limited preservation of residual hearing.

Due to the precision required for proper cochlear implant placement and the requirements of a soft surgical technique to reduce trauma and preserve residual hearing, this chapter investigates the use of a cochlear inspection tool and real time guidance via visual and auditory cues to reduce variability in surgical execution of perimodiolar electrode array placement. Variability of surgical technique is characterized in standard practice on temporal bone specimens, then the changes in surgical behavior when using intracochlear visualization and assistance are assessed.

3.1 Medical Background

Hearing loss and deafness are serious medical impairments that affect a large proportion of the population. In the United States of America, there are almost 2 million residents over the age of 12 with severe hearing loss and 0.4 million with profound hearing loss in their better ear [111]. Despite this large number of affected individuals, as of 2012, only 58,000 adults and 38,000 children had been fitted with cochlear implants [112]. Hearing loss can have drastic impacts on socioeconomic status of those with this condition, lowering

educational attainment rates and increasing the odds of low income, unemployment, or underemployment [113]. Medical interventions that can reduce the amount of hearing loss may recoup some of the estimated almost $300,000 in economic costs to the country per individual with profound deafness or severe hearing impairment [114].

Cochlear implants are suited for individuals with deafness or severe hardness of hearing, and while not all people with such conditions will be candidates for cochlear implant surgery, there is a growing range of individuals who can serve as candidates. In addition to an aging population that will have a higher prevalence of hearing difficulties and the fact that approximately 3 out of 1000 children are born deaf [115], the candidate pool for CI implantation is growing due to the expansion of situations in which implantation is medically advisable, including those with residual hearing that must be preserved [116]. As more patients with residual hearing are being treated with cochlear implants, a soft surgical technique has been adopted to avoid intracochlear trauma. Trauma to structures inside the ear can affect residual hearing, leading to worse hearing outcomes [117].

There are two major types of electrode arrays: outer wall and perimodiolar. Outer wall electrodes are inserted directly into the cochlea and their flexible nature allows them to follow the outer wall and align with the helical structure of the cochlea. Perimodiolar EAs are designed to follow the inner wall, which is hypothesized to allow for better electrical stimulation since the stimulation target (the auditory nerve bundle) resides at the center of the helix. These EAs have a naturally bent shape that matches the nominal cochlear geometry. A platinum stylet holds each array straight for original insertion into the cochlea, but as the array is pushed off the stylet, it bends to match the shape of the cochlea in a surgical technique referred to as Advance Off-Stylet (AOS). The AOS procedure is shown in Fig. 3.1. Due to the need to insert the array in a particular orientation and with AOS started at the proper depth such that the shape of the EA matches the shape of the cochlea, the surgical technique involved in perimodiolar EA insertion is more technically challenging than that in outer wall arrays. This work used practice electrodes of the most commonly

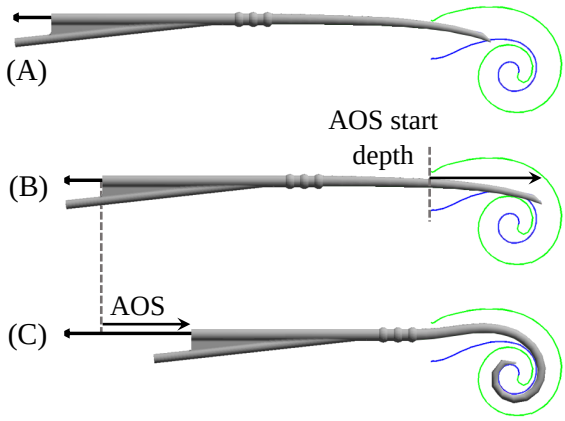

Figure 3.1: The insertion process for a perimodiolar electrode array. A) An electrode is inserted into the cochlea B) At the beginning of the Advance Off-Stylet (AOS) procedure, the tip of the electrode has been inserted to the proper depth so that it is at the basal turn. C) With the stylet held in place, the electrode is slid off the stylet to match the shape of the cochlea.

used perimodiolar EA, the Contour Advance, provided by Cochlear Corporation.

Regardless of the array type, one of the factors most important for good hearing outcomes is atraumatic insertion with the electrode array residing fully in the scala tympani [118, 119] (a helical chamber within the cochlea). However, membrane rupture causing electrodes to leave the scala tympani and other intracochlear trauma may occur with very small forces [120] at or below the limit of force perception by hand. In addition, placement of the electrode array close to the modiolar wall has been shown to reduce excitation thresholds [121] and lead to better hearing outcomes [122]. Placement of perimodioloar electrode arrays requires skill in choosing the access point into the scala tympani [123] and in aligning the pre-bent electrode array accurately with the natural bend of the cochlear basal turn. This skill dependence was shown to lead to lower rates of electrode positioning within the scala tympani for perimodiolar electrodes [122], highlighting the need for better guidance when using this kind of array.

The combined surgical requirements of maintaining optimal electrode position for better nerve stimulation and soft insertion technique for reduced trauma are complicated by a number of factors. Since the cochlea is a closed bony structure, there is no way to visual-

ize the electrode position intraoperatively. While surgeons can inspect the extra-cochlear anatomy, there are variations in cochlear anatomy between different individuals, so it is impossible to fully discern intracochlear anatomy by inspecting extracochlear anatomical landmarks [116, 124]. While surgeons can approximate what should be done on average, their surgical technique may or may not match the anatomy of any given patient if they must rely solely on extracochlear inspection. These combined factors contribute to a perception deficit which, when added to the inability of surgeons to fully control the shape of the EA during insertion, leads to intrachochlear trauma.

3.1.1 Relevant Works

There have been a number of works in the past that have worked toward automatic or robotic insertion of cochlear electrode arrays. These have included automated insertion of custom electrodes with embedded actuation [125], parallel robots for insertion [126, 127], and an automated insertion tool [128] with force sensing [129] and image guidance [130]. Preoperative imaging has been used to guide the insertion process combined with a specialized drilling procedure with a patient-mounted frame [131] or a robotically drilled narrow mastoidectomy [132]. These approaches require large changes to the surgical workflow and may require specialized tools to insert the electrode through a narrow channel compared to a standard mastoidectomy.

Due to the complexity, cost, and need for precise registration of robotic techniques, simpler methods for improving cochlear implant insertion have been attempted as well. Intracochlear inspection has been achieved previously [133] but without an examination of the possible uses of what to do with the information gained by the surgeon after the use of an intracochlear visualization tool. Surgical simulators have been used to show that training and image guidance is possible for the improvement of surgical technique [134], and preoperative imaging has been shown to improve insertion technique and electrode positioning when surgeons are given directions on how to insert an EA [135]. In the broader

otologic space, visualization of the middle ear through the eustachian tube has also been proposed [136].

Other methods to improve electrode positioning have investigated additional sensory modalities to localize electrodes during insertion, including the use of intracochlear bipolar impedance measurements [137], OCT measurements [138] or a built-in MEMS sensor within a custom electrode [139]. Previous work on complementing the surgeon's perception has shown that the combination of in-vivo force sensing with machine learning methods can warn the surgeon about an impending electrode insertion failure such as the onset of tip foldover [140].

3.1.2 Motivation and Contribution

This work is motivated by the lack of baseline data regarding surgeon performance in terms of insertion metrics defined as the AOS depth and alignment error of the perimodiolar electrode array with the basal turn of the cochlea. In addition, the potential benefits of visual guidance in reducing variability in insertion metrics has not been investigated. The contribution is aimed at addressing these two needs while also investigating the utility of intracochlear inspection prior to implantation as an aid for surgeons' understanding of the internal anatomy relative to the externally visible bony anatomy.

This work expands on prior works by investigating the possibility of surgical guidance with minimally disruptive imaging techniques in order to elucidate the potential benefits of low-cost and simple methods in improving surgeons' performance. By focusing on fiberscopic inspection and improved instrument motion guidance, we present a low-cost, simple to implement system for improvement in electrode array insertion and investigate the utility of different guidance cues in improving the consistency of surgical performance.

Figure 3.2: Cochlear Inspection Tool comprised of a 1mm flexible fiberscope with 10,000 imaging fibers, a user handle and optical tracking markers.

3.2 Tool Design

An intracochlear inspection tool was designed to provide surgeons more information about the patient anatomy; this was combined with tool tracking and a graphical user interface (GUI) in order to provide real-time guidance and recording of tool movements during EA insertion. Visualization of the intracochlear anatomy was achieved by insertion of a small fiberscope through the cochleostomy. The handle for this device can be seen in Fig. 3.2, which is termed the Cochlear Inspection Tool (CIT).

The CIT was composed of a 3D-printed resin case that clamped around a 1mm fiberscope with 10,000 image fibers, manufactured by Medit Inc (Manitoba, Canada). Weighing only 32 g, it fit comfortably in a surgeon's hand. The fiberscope fit into the cochlea without contacting the walls of the scala tympani, however it was large enough that in many bones a larger extended window cochleostomy had to be performed than would normally be clinically necessary. Smaller diameter endoscopes or fiberscopes are commercially available and could be substituted in eventual clinical adoption, but the overall procedure would remain unchanged and so the slightly larger diameter should not affect the study results. The fiberscope was attached to a Toshiba (Tokyo, Japan) IK-M44H camera with an Omex Technologies (Illinois, USA) 45mm optical coupler. Light for the fiberscope was provided with a Karl Storz (Tuttlingen, Germany) Xenon 175 Watt light source.

3.2.1 Tool Tracking and Calibration

The CIT, along with electrode-holding forceps and stylet-pulling tweezers were outfitted with four tracking markers to record the location and orientation of the instrument

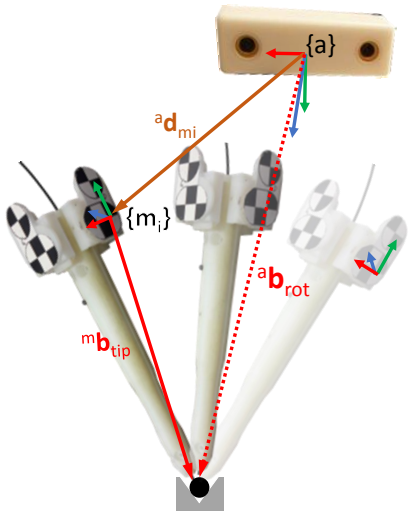

Figure 3.3: Tip calibration procedure for Cochlear Inspection Tool (CIT). The tool is rotated around a central pivot point to find the tip location in each optical tracking marker's frame.

movements throughout an experiment. A Claron Technology (Ontario, Canada) Micron-Tracker 2 optical tracker was used to measure the tool poses, which has a calibrated RMS accuracy of 0.2 mm and jitter of 0.015 mm for a static target. Tracked tool locations were reported in reference to a reference marker mounted on the temporal bone so that all instrument locations were reported relative to a frame attached to the cochlea.

The location of the tip of the tool relative to its markers was determined in a calibration procedure by rotating the tool around its tip. By attaching a sphere at the end of the tool, the tip was constrained to remain in place while the sphere rolled within a cone. The sphere adds a known offset to the tooltip distance which can be subtracted off after the calibration procedure is finished. Fig. 3.3 represents this process graphically. After collecting the poses of the markers during the rotation, the tool tip frame can be calculated.The readings taken by the optical tracker during this calibration can be represented as:

$$^{a}\mathbf{b}_{rot} = {}^{a}\mathbf{d}_{m_i} + {}^{a}\mathbf{R}_{m_i}\,{}^{m}\mathbf{b}_{tip} \tag{3.1}$$

Where the superscript 'a' represents a measurement in the optical tracker frame {a}, and

the superscript 'm' a measurement expressed in the marker's frame {m}. The vector ${}^{a}\mathbf{b}_{rot}$ is the location of the pivot point around which the tool was rotated, ${}^{a}\mathbf{d}_{m_i}$ is the location of the marker in the i^{th} pose of the tool, ${}^{a}\mathbf{R}_{m_i}$ is the rotation matrix of the marker's orientation in the i^{th} pose, and ${}^{m}\mathbf{b}_{tip}$ is the location of the tip of the tool in the marker frame. Since ${}^{m}\mathbf{b}_{tip}$ and ${}^{a}\mathbf{b}_{rot}$ represent constant unknowns, they do not require any subscripts, whereas ${}^{a}\mathbf{R}_{m_i}$ and ${}^{a}\mathbf{d}_{m_i}$ are pose-dependent. Rearranging this relationship as:

$$ {}^{a}\mathbf{R}_{m_i}\,{}^{m}\mathbf{b}_{tip} - {}^{a}\mathbf{b}_{rot} = -{}^{a}\mathbf{d}_{m_i} \tag{3.2} $$

Multiple readings can be stacked to find a least squares solution for the unknowns:

$$ \begin{bmatrix} {}^{m}\mathbf{b}_{tip} \\ {}^{a}\mathbf{b}_{rot} \end{bmatrix} = \begin{bmatrix} \vdots & \vdots \\ {}^{a}\mathbf{R}_{m_i} & -\mathbf{I} \\ \vdots & \vdots \end{bmatrix}^{\dagger} \begin{bmatrix} \vdots \\ -{}^{a}\mathbf{d}_{m_i} \\ \vdots \end{bmatrix} \tag{3.3} $$

where the † superscript represents the Moore-Penrose Pseudo-Inverse.

Each tool was equipped with 4 optical tracking markers on the top, bottom, left, and right sides of the tool so that at least one marker could be seen no matter how the surgeon held the tool relative to the optical tracker. The above procedure estimated the location of the tip only for one marker on one tool, so it was repeated for every marker on each tool. This procedure only produces the location of the tip, so one of the markers was defined as a reference frame and its orientation was defined as the tip orientation. When this reference marker was not visible, the average relative rotation between the currently visible marker and the reference marker was used to calculate the tip pose during an experiment. Measurements of the relative rotation between the markers were taken with the tool in various poses and averaged to eliminate sensor noise. Averaging of rotations was carried out using quaternion-based rotation averaging as described in [141]. The resulting tool-tip position and orientation is henceforth referred to as 'CIT tip frame'.

To account for the effects of possible movement of the temporal bone or the tracker during an experiment, a world frame is defined as a marker rigidly affixed to each temporal bone. This frame is designated as {w} and is simultaneously tracked along with all tool markers. All other marker measurements are pre-multiplied by the homogeneous transform ${}^{a}\mathbf{H}_{w}{}^{-1}$, the inverse of the homogeneous transform of the {w} frame seen by the tracker, to put them in the frame of the bone-attached world frame. This procedure is carried out for all poses describing tool motion and is therefore omitted in the equations describing tool pose for brevity of notation.

3.2.2 Camera Frame Calibration

While the pose of the CIT is known from the markers and associated calibration, the fiberscope camera is not necessarily aligned with the tool itself. The fiber, before being clamped in place by the CIT, can spin and may not be facing in the exact direction of the a priori frame of the CIT. Therefore, a rotation must be introduced between the CIT tip frame and the fiberscope camera frame.

The calibration procedure can be performed using a marker recognizable from the optical tracker that can be simultaneously visualized through the CIT. Fig. 3.5 shows the calibration setup to define the rotation matrix between the view in the endoscope camera frame {c} and the calibrated CIT tip frame {tip}, designated ${}^{c}\mathbf{R}_{tip}$. The CIT is oriented perpendicular to a fixed calibration marker with frame {d} that is visible to the optical tracker and also through the endoscope camera (note that the figure does not show exact perpendicularity for ease of visualization). The CIT is rotated about its longitudinal axis until a red line in the image view aligns with a designated line on the calibration marker. The lines were designed so that the frames {c} and {d} align when the lines overlap.

The calculation of the rotation matrix ${}^{c}\mathbf{R}_{tip}$ is found using a loop closure equation of

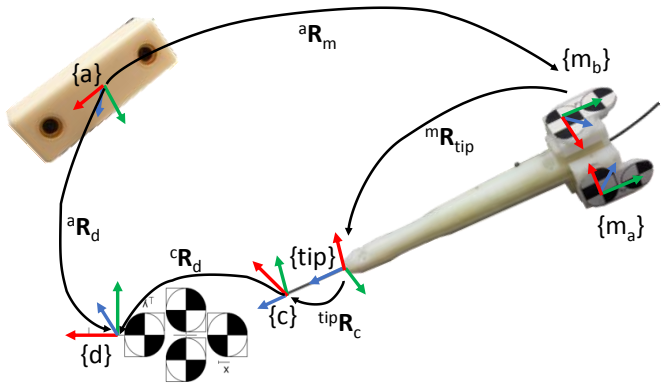

Figure 3.4: Calculation of the camera calibration matrix with the aid of a calibration marker

the frames in Fig. 3.4 and rearranging to solve:

$$ {}^{d}\mathbf{R}_{a} = {}^{m}\mathbf{R}_{a}\,{}^{tip}\mathbf{R}_{m}\,{}^{c}\mathbf{R}_{tip}\,{}^{d}\mathbf{R}_{c} \tag{3.4} $$

When the user has aligned the image properly, ${}^{d}\mathbf{R}_{c}$ is an identity matrix. Both ${}^{d}\mathbf{R}_{a}$ and ${}^{m}\mathbf{R}_{a}$ are measured directly from the optical tracker. ${}^{tip}\mathbf{R}_{m}$ is known from the CIT tip frame calibration procedure in Section 3.2.1. Therefore, ${}^{c}\mathbf{R}_{tip}$ can be calculated and saved according to equation 3.5. This rotation is applied to the CIT tip frame when saving any orientations measured according to the view in the CIT image.

$$ {}^{c}\mathbf{R}_{tip} = \left({}^{m}\mathbf{R}_{a}\,{}^{tip}\mathbf{R}_{m}\right)^{\mathrm{T}}\,{}^{d}\mathbf{R}_{a}\,\left({}^{d}\mathbf{R}_{c}\right)^{\mathrm{T}} \tag{3.5} $$

3.2.3 Electrode Tip Calibration

Every time an electrode was first grasped in the electrode forceps, the surgeon was asked to calibrate the electrode tip by aligning the electrode array tip to be tangent to a line in an optical calibration marker, as in Fig. 3.5. The relative pose between the tool tip and the indicated mark on the calibration marker was used to discern the fixed offset between the orientation of the electrode holder and the tip of the electrode array. Since each electrode was grasped slightly differently, this step was necessary to account for variations in grasp

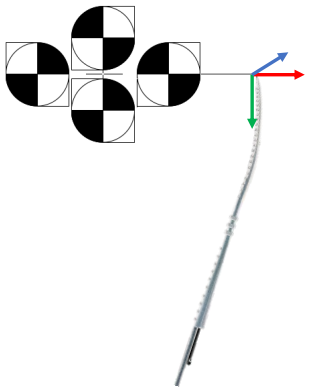

Figure 3.5: Electrode calibration marker

from trial to trial and from surgeon to surgeon.

3.3 Basal Turn Depth Segmentation

During PEA insertion, the depth of AOS is one important metric for accurate placement of the EA inside the cochlea. A number of different methods were attempted to achieve reliable, automatic depth measurement of the basal turn relative to the distal end of the fiberscope.

A first approach was the use of optical flow to measure depth into the cochlea. This method suffered from both implementation issues specific to the anatomy/geometry as well as more fundamental issues with depth estimation by using optical flow. Firstly, the anatomy inside the ear is relatively smooth, lacking the sharp corners that are best for tracking in optical flow algorithms. Additionally, the lighting that is attached to the image fiber results in a constantly changing lighting condition that can result in tracking the light coming from the fiber instead of objects in the image. Furthermore, the optical flow algorithm only results in generalized movement of points, from which estimation of camera movement must be calculated. And even when that is done, there is no measurement or segmentation of the basal turn itself, only the depth of insertion. For all these reasons, this was determined not to be a suitable method to continue pursuing.

Because of the need to segment the basal turn, direct image processing was attempted to try to extract the edge of the turn in images and use that as a guideline for the depth estimation. The first task is to extract that particular edge from the image. The segmentation process involved multiple steps of thresholding, edge detection, noise reduction, and picking the longest edge in a cleaned image, some of which are shown in Fig. 3.6. Once

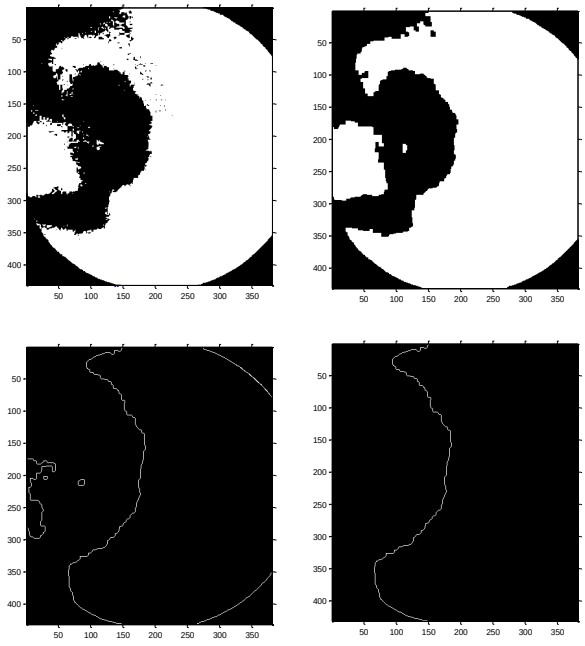

Figure 3.6: Binary images and edge segmentation of basal turn

the edge representing the basal turn has been segmented, it is still necessary to create some unified metric of size. For this task, it was decided that fitting an ellipse is generally in keeping with the anatomy. While the anatomy is not exactly elliptical, it can be well-approximated by such a shape. It is also appealing because the major axis of the ellipse can be used as the size of the basal turn, and then that size can be fed into a monocular vision algorithm to estimate the depth of the turn. However, fitting an ellipse to a subset of arbitrary points is a somewhat difficult problem - the Random Sample and Consensus (RANSAC) algorithm is one good option that works well in a number of contexts. An example of the total segmentation and the ellipse fit to the edge can be seen in Fig. 3.7. While the RANSAC algorithm can be made to work, it requires relatively long processing

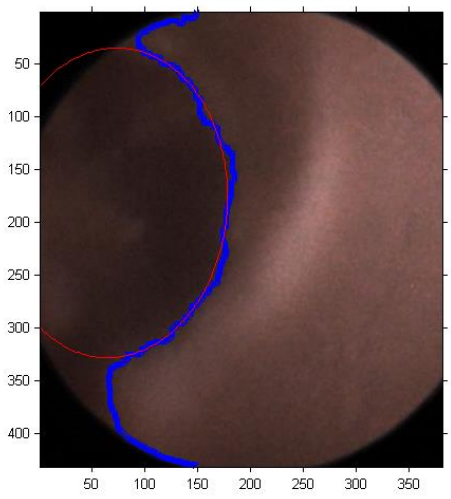

Figure 3.7: RANSAC Algorithm Results

time to pick the right ellipse out of the image. Also, because it is based on randomly picking points out of the image, there is no guarantee of convergence. There is also the problem that, if the image contains other smooth features, there can be multiple ellipses detected in the images which can confuse the algorithm's results. In the end, this complicated method contained a large number of parameters that would need re-tuning and a long computation time, so a simpler method was sought.

3.3.1 Reflected Light to Estimate Depth of the Basal Turn

While simpler than the above methods in image segmentation or optical flow, an image-intensity-based method proved more repeatable. When approaching the wall, more of the light from the fiber is reflected back into the image and image intensity increases. This intensity can be thresholded to determine proximity to the basal turn which can inform when to initiate AOS technique.

The method was tested on human temporal bones prepared with a lateral round window mastoidectomy mounted on an ATI Nano43 force-torque transducer. Repeated insertions were carried out using the bone holder setup and Cartesian robot seen in Fig. 3.8a and b.

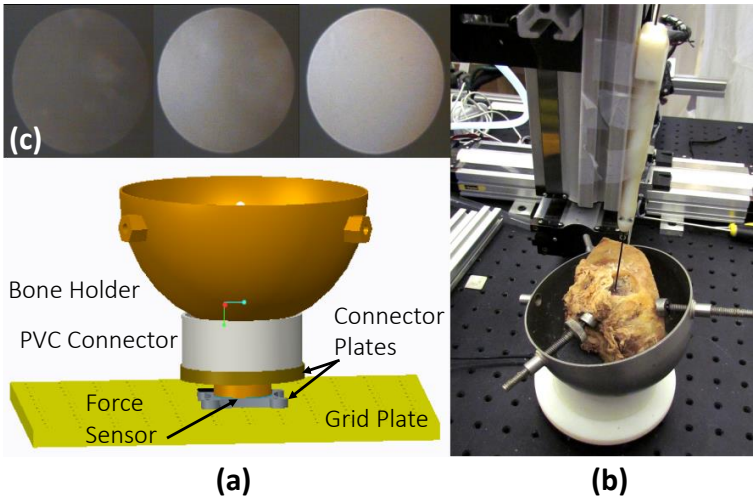

Figure 3.8: (a, b) Experimental setup for controlled insertion of CIT into temporal bone specimen with force measurements and fiberscopic visualization (c) example intensity images as the fiberscope approaches the modiolar wall

The CIT was mounted on a 3-axis Cartesian robot and aligned to have clear access through a cochleostomy into the cochlea. The robot was used to slowly insert the fiber into the cochlea vertically until its tip made contact with the wall of the basal turn. Contact with the wall was determined by manually segmenting a rise in the force measurements indicating wall contact. While repeatable, this manual process is one source of potential error. After wall contact, the fiber was retracted 5mm to set a home point. From this point, repeated insertions were carried out in steps of 0.2 mm until reaching the original home point. An image was taken at each step to characterize the intensity vs depth relationship; an example set of images is shown in Fig. 3.8c. The force sensor was unbiased at the start of each insertion into the cochlea and force data was filtered by a moving-window averaging filter with a length of 10 samples at 5kHz sampling frequency. Intensity was reported as the mean of all pixels in the image, normalized between 0 and 1, where 1 represents the intensity of an image with the tip of the fiber placed in front of a white background (as close as possible, but within the limits of the focal length of the fiberscope lens).

36 insertions were carried out in 3 temporal bones. Originally, 5 bones were analyzed using the experimental setup, however 2 bones were removed from analysis due to discol-

oration from mold/bacteria not representative of living anatomy due to long storage time. The 36 insertion experiments were divided into 3 groups of 4 insertions per bone. For each insertion group, the bone was removed and affixed to the setup in a new orientation to capture changes in approach angle and rotation of the endoscope relative to the bone that may occur in the eventual use of this tool.

3.3.2 Reflected Light Depth Results

Fig. 3.9 shows the intensity-measurement results across 36 insertion in 3 temporal bones. The solid line is the average intensity, the error bars are the 95% confidence interval on the mean, the dotted lines are the 95% data intervals (two standard deviations from the mean), and the gray bounds represent the maximum and minimum intensities. In two insertion groups, the fiber was deflected away from the wall, reducing intensity measurements. Since a surgeon would know to reorient when seeing such a deflection, these were dropped from analysis in Fig. 3.9b. With this exclusion, a threshold of mean normalized intensity of 0.33 can estimate the basal turn depth in 95% of cases with an uncertainty of 1.2 mm without touching the wall of the basal turn.

This method shows the viability of using fiberscopic visualization of cochlear anatomy and the usefulness of light-intensity-based methods for characterizing distance to the basal turn. This a naive approach to estimate the distance to the basal turn based on 95% of expected normalized intensity across bones.

Additional methods that could be investigated include Bayesian filtering considering measurement history for a given bone and a statistical prior across many bones to improve the distance estimation robustness and accuracy. The intensity rise near the basal turn should be more prominent in a clinical setting where the surgeon can manually re-orient the fiber, and in living specimens where there will be less drying out of the bone which, even after re-wetting, contributed to decreased light reflectivity. Future work should investigate the repeatability of these results across additional bones and in in-vivo situations, as this

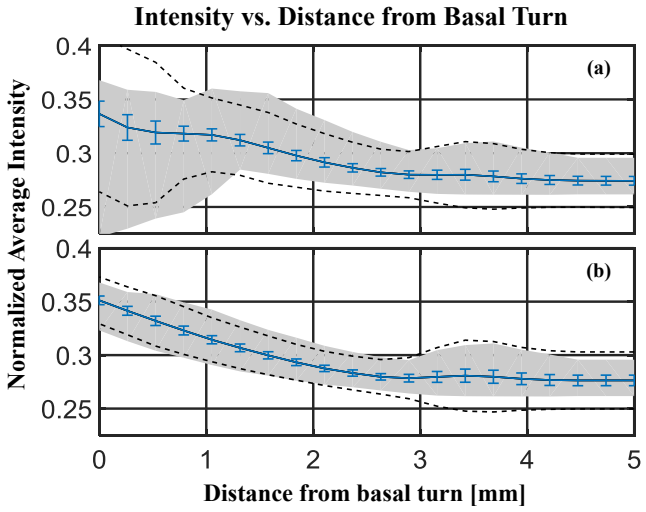

Figure 3.9: Intensity vs wall distance results: mean intensity (solid line), 95% CI error bars of the mean, 95% of expected data (dotted line), max and min bounds (gray area) for behavior in (a) all insertions (b) insertions without fiber deflection.

work has limited data to draw on. Whereas the ex-vivo bones were largely devoid of visual features suitable for application of optic flow because the bone appearance in formalin-fixed cadaver bones is white and very smooth, the vasculature in living tissue would presumably provide additional visual features (e.g. vasculature) and different optical properties in light reflection.

3.4 User Study Materials & Methods

A user study was developed to establish a baseline for surgeon performance during perimodiolar electrode array insertion and to investigate the utility of surgical guidance using the CIT. Performance metrics were defined by which the electrode array alignment and the depth of AOS initiation were quantified. This included a definition of ground-truth data for optimal parameters for each of these measurements. A physical experimental setup was designed and constructed and a software suite was created consisting of a user guidance graphical user interface (GUI), tool motion tracking, and data-logging. Practice Contour Advance perimodiolar EAs that were not connected to a receiver were used as a stand-in for

functioning electrodes (supplied by Cochlear Corporation). The practice electrode arrays have not undergone a rigorous post-manufacturing certification process and therefore may not be an accurate depiction of EA's for clinical use. These components were used in a user study of trained otologic surgeons whose protocol is presented in section 3.5.

3.4.1 Electrode Arrays Insertion Performance Metrics

Three metrics were used to characterize surgeon performance: AOS depth, EA approach vector, and EA roll.

Advance Off-Stylet Depth: Improper depth of AOS can contribute to improper EA seating and potential tip fold-over [142]. While markers on the PEA indicate a preferred AOS initiation depth, variability in anatomy and drilling changes the optimal AOS depth for a given patient. While tip fold-over has relatively low rates of occurrence, around 2% [143], more accurate and repeatable AOS initiation should reduce this adverse effect as well as improve EA placement and reduce trauma, which motivates AOS depth as one important surgical metric.

Electrode Roll: To improve the alignment of a PEA's shape and that of the cochlea, the EA should be inserted so that it curls in the same direction as the helix of the cochlea. This alignment was characterized by the angle θ in Fig. 3.10, which represents the roll angle of the EA around its longitudinal axis, $\hat{\mathbf{b}}$, with respect to the cochlea's major axis, $\hat{\mathbf{h}}$. θ is calculated as the angle between $\hat{\mathbf{h}}$ and $\hat{\mathbf{e}}$, the bending axis of the EA.

Surgical technique characterized by misalignment of the EA's natural bending plane and the cochlea's basal turn are noted when θ is very large or highly variable. This misalignment can result in deviation from the soft surgical technique, rubbing the EA against the walls of the cochlea or causing a translocation of the EA from the ST to the SV.

Electrode Approach Vector: The approach vector into the cochlea characterized the overall orientation of vector $\hat{\mathbf{b}}$ in Fig. 3.10. There is no ground truth vector that has been

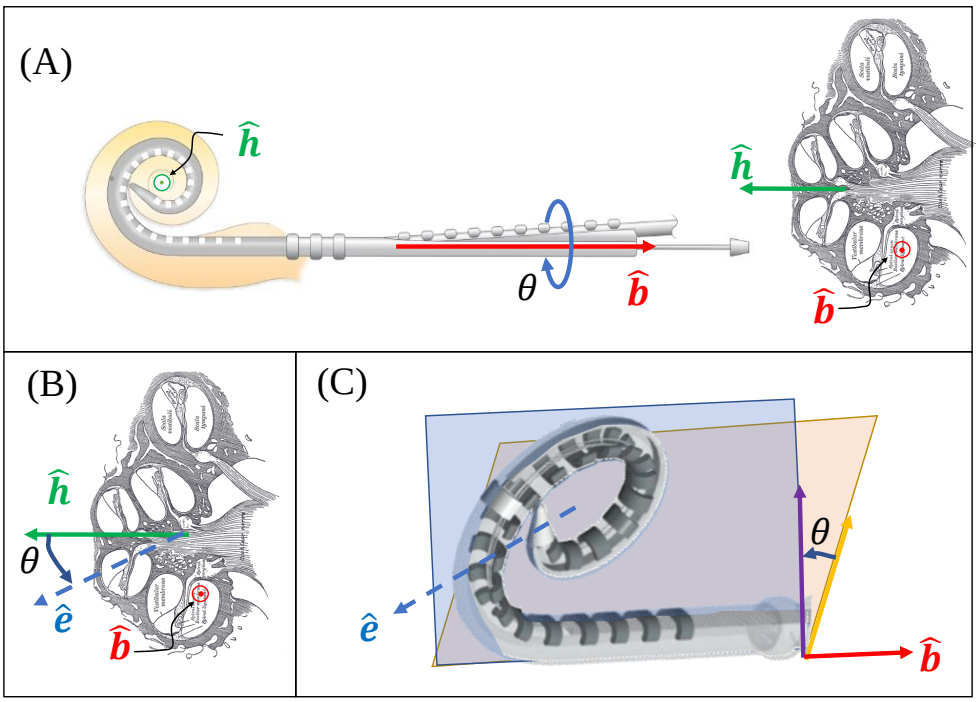

Figure 3.10: Surgeons must roll the array about its longitudinal axis $\hat{\mathbf{b}}$ to allow the electrode curl about $\hat{\mathbf{e}}$ to match the major axis of the cochlear helix $\hat{\mathbf{h}}$. Cochlear longitudinal section in public domain from [2]

reported in the literature that would represent an "optimal" electrode approach vector. We hypothesized that the vector corresponding to the longitudinal axis of the fiber of the CIT during inspection would present a useful target. However, surgeons found it difficult to control 3 orientational degrees of freedom and insertion depth while simultaneously respecting the constraints provided by the geometry of the cochleostomy, mastoidectomy, and facial recess, which limited the potential access angles into the cochlea. Additionally, the curved and flexible shape of the electrodes made the determination of what constituted a "tip approach vector" difficult to standardize and communicate to surgeons. Because of these factors, and in consultation with local surgeons testing the system, we did not provide guidance in controlling this vector but still collected data to show baseline variability of this metric.

Ground Truth Measurements: To assess the above metrics, it was necessary to determine appropriate ground truth measurements of the relevant anatomical characteristics. We

created a 3D CT model of each temporal bone using a Xoran xCAT ENT scanner (Xoran Technologies, Ann Arbor, MI) with isotropic 0.3mm voxels, tube potential of 125 kV, and current of 6 mA [144]. Two scans were taken, one before any experiments took place and another with EAs glued in place after all experiments were completed.

The plane of the basal turn was determined by automatic segmentation of the major axis of the cochlea in CT following previously published methods[145, 146]. While this process gives a particular plane of the curling of the cochlea, it may deviate slightly from the optimal angle for the electrode roll, which depends not only on the anatomy, but also on EA design and the insertion trajectory; the determination of this exact angle is beyond the scope of this research. After segmentation of the cochleostomy in CT, the depth into the cochlea toward the basal turn was measured along the vector from the cochleostomy to the outer wall at the basal turn. The optimal depth was defined as the length along this vector at the basal turn. This linear measurement of depth approximates the angular measurements from Cohen's template[147] that more closely corresponds to the physical motion of the surgeon during insertion.

3.4.2 User Study Experimental Setup

An experimental setup was devised to facilitate the user study described in Section 3.5. The setup was designed to allow data-logging of tool positions and orientations and insertion force data while also making use of a custom graphic user interface (GUI) with audio and visual cues for assisting surgeons in achieving proper alignment during electrode insertion.

Fig. 3.11 shows the experimental setup used to carry out the experiments. In addition to the tracked tools and calibration marker, a surgical microscope was used for illumination and visualization of the bone specimen. Twelve temporal bone specimens were prepared with access to the scala tympani of the cochlea via a mastoidectomy and extended round window cochleostomies drilled by otology fellows and residents at Vanderbilt University

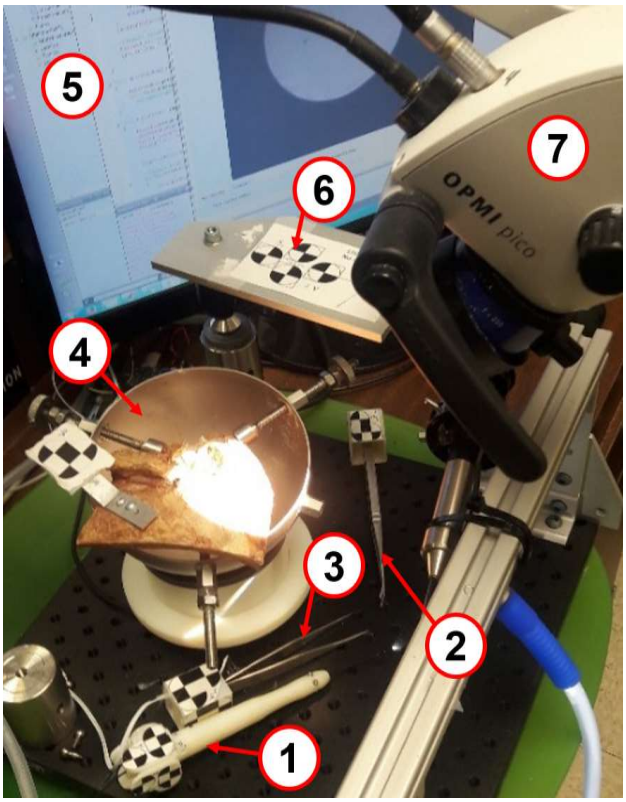

Figure 3.11: A view of the experimental setup: 1) The Cochlear Inspection Tool 2) Electrode-holding forceps 3) Stylet-holding tweezers 4) Bone holder mounted on a force sensor 5) Screen to see CIT images and GUI for tool guidance 6) Calibration Marker 7) Surgical Microscope.

Medical Center. The variability of cochleostomy location may provide additional uncertainty in the final outcomes of the study, as cochleostomy location can impact electrode placement [148].

Each bone was numbered and affixed with an optical tracking marker. The bones were supplied in a formalin-fixed state to allow for greater longevity than fresh bones. Since the study relies on the general anatomy of the cochlea and not measurements or interaction with tissue or other sensitive structures directly, the use of fixed as opposed to fresh bones should not have provided any significant detriment to the realism of the study. Each bone specimen was placed in a standard temporal bone holder as seen in Fig. 3.12. Surgeons were allowed to adjust the position of the holder and the position of the bone in the holder to best approximate the orientation of an ear as they would expect to see it in surgery.

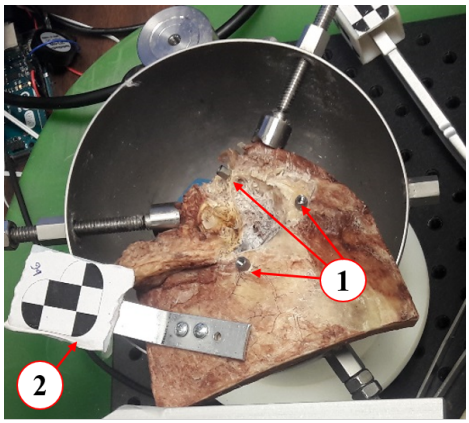

Figure 3.12: Each bone was equipped with: 1) fiducials and 2) a unique tracking marker so that the tracking software could measure the location of the bone and a registration could be performed between CT scans of the bone and the optical tracking measurements.

To be able to register the bones to the optical tracking system as well as any CT images taken, multiple screws with spherical fiducial attachments were affixed to the bones to act as tracking fiducials. Three screws, seen in Fig. 3.12, were attached to the bone for easy segmentation in both CT and by an optically tracked tool. With these locations saved in both CT and optical tracking frames, any CT scans can be registered to the frame of the optical tracking marker on the bone via a rigid registration.

Forces were recorded during electrode insertion using an ATI Nano 43 force/torque sensor. The sensor was rigidly attached to a metal plate. A custom-made attachment connected the force sensor to the bowl holding the bone specimen. For the surgeons' ease in aligning the bones, the bowl was not rigidly attached to the fixture but instead held in place by a rubber ring; friction between the ring and the heavy metal bowl prevented movement during standard surgical practice and forces could be measured as transmitted through the ring, but it still allowed the surgeon to reposition the bone between experiments. A software system was created to assist in carrying out these experiments for data recording and providing visual guidance. The system was written in C++ using Qt and contained functionality integral to many different pieces of the experimental protocol. It displayed images from the CIT camera with interfaces for capturing still images and recording video. The software

communicated with the MicronTracker system to record and display representations of the tool orientations in real-time with various different graphical user interface (GUI) overlays.

The software was used to save all relevant pieces of information during the experiment so that all the orientations and positions of the tools could be used during evaluation and statistical analysis. It was made to be easy to use by an assistant to the surgeon who pressed various buttons on a visual interface to record pertinent data of the tool movements during the procedure.

3.5 User Study Design

In order to establish baseline surgeon performance during electrode array insertion and evaluate the utility of CIT visualization and guidance, a group of surgeons were enrolled in an IRB-approved user study. A total of 7 surgeons were enrolled in the protocol, however 2 less-experienced surgical residents were excluded from analysis after taking a partial dataset due to stated lack of familiarity with the procedure.

The surgeons consisted of 2 attending physicians, 2 surgical fellows, and 1 senior resident. Surgeons were recruited from Vanderbilt University and New York University medical centers. Most surgeons sat for multiple sessions due to the length of the full protocol spanning over 3 hours in total. One of the surgeons assisted with the ergonomics of the experimental setup and the fine-tuning of the user interface; therefore this user acquired significant skill using the tool and experience completing the steps of the experimental protocol compared to the other surgeons who only had a brief 15-30 minute training period at the beginning of the protocol.

The overall design of the user study is summarized in Table 3.1. There were 4 types of procedures performed by each surgeon enrolled in the study: there were both unguided and CIT-guided experiments of both electrode orientation experiments and full electrode insertion experiments. The difference between guided/unguided experiments and orientation/insertion experiments are defined in more detail in the sections below. The orientation

experiments used the same 5 bones across all surgeons; however some of the surgeons used only a subset of these bones due to time constraints and preliminary statistical analysis showing that a smaller dataset would be satisfactory. Each surgeon was assigned 2 bones for the full insertion experiments that were not shared with the other surgeons.

Each surgeon was afforded a period of training and orientation to practice using the CIT to inspect the anatomy and learning how to understand the software associated with the visualization and guidance. Additionally, each surgeon was given the opportunity to rearrange each bone presented to him/her in the bone holder to match the expected position of a human ear in surgery.

In the final trial of the full insertion experiments, the electrode was glued in place and the final electrode location was segmented in a CT scan. Each surgeon had one glued trial with an unguided insertion and one glued trial with a guided experiment. After the user study had concluded for all 5 surgeons, 100 trials had been completed across 5 bones for both unguided and guided orientation experiments and 20 trials over 10 bones for both unguided and guided full insertion experiments. One reason for repeating the full insertion experiments was to measure forces during insertion. However, there were no statistical differences in the forces between unguided and guided experiments and more inter-experiment differences due to the conditions of the bones used and the particulars of the method we used to soak the bones in a perilymph-imitating fluid (a glycerin-saline mixture). Therefore, details of these results have not been included.

3.5.1 Unguided Orientation and Assessment of AOS Onset Depth

During unguided mock-insertions the surgeons were asked to hold an electrode array with standard electrode forceps and align the electrode as if (s)he were starting an insertion, but not performing the Advance-Off-Stylet (AOS) procedure. This procedure is termed an "orientation experiment" since the electrode is oriented in the direction of insertion, but not inserted fully into the cochlea. The surgeons were asked to insert the electrode array into

	Number of Trials	Total Bone Specimens	Bones per Surgeon	Forces Measured
Unguided Electrode Orientation	100	5	{2,4,4,5,5}*	No
CIT-Guided Electrode Orientation	100	5	{2,4,4,5,5}*	No
Unguided Full Insertion	20	10	2	Yes
CIT-Guided Full Insertion	20	10	2	Yes

Table 3.1: Design parameters of the user study to evaluate utility of cochlear inspection and guidance in insertion of electrode arrays. *The protocol originally specified 5 bones per surgeon, but fewer were used in practice after preliminary statistical analysis to respect time constraints of enrolled surgeons.

the cochlea to the depth that corresponds with the beginning of AOS while also aligning the plane of natural bend of the electrode array with their perceived plane of the basal turn. The surgeon held the electrode array in the bone at the position and orientation where AOS would be initiated, and the software saved the current orientation of the electrode array and its depth as measured by the optical tracking markers on the electrode forceps. After the electrode pose had been saved, the surgeon was asked to remove the electrode without inserting it fully into the cochlea.

Each surgeon repeated this process 5 times for each bone. This experiment was used to characterize surgeon repeatability and assure statistical significance by increasing the number of insertions without wearing out the cochlea by repeated insertion and removal of electrodes that could change the experimental conditions after preliminary insertions had been completed.

3.5.2 Guided Orientation and Assessment of AOS Onset Depth

Similar to the previous experiment, each surgeon performed an orientation-only experiment without fully inserting an electrode, but this was preceded with an inspection step that allowed the surgeon to use visual cues to pick a depth and direction for optimal insertion and use that to guide instrument position during electrode orientation.

The first step the surgeon performed was the inspection of the cochlea. The Cochlear

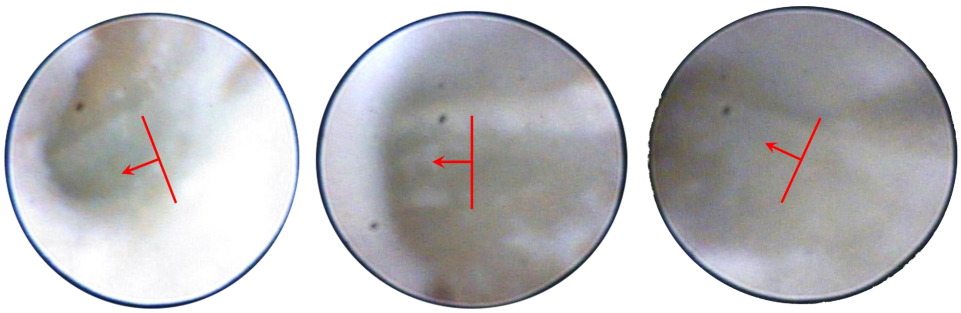

Figure 3.13: Images from the CIT as it is inserted into one of the bones used in this study. The red arrow shows the user's estimate of the optimal bending direction of the electrode array.

Inspection Tool (CIT) with accompanying fiberscope was inserted into the cochlea to visualize the basal turn. Using the camera view shown in the GUI, the surgeon selected the depth of optimal AOS by inserting the plane of the image to the depth corresponding with optimal AOS. They simultaneously marked the desired electrode roll angle by communicating with the assistant who controlled an overlaid arrow on the screen in order to digitize the surgeon's interpretation of the basal turn direction in the image plane. Example images from the fiberscope with an arrow overlaid are shown in Fig. 3.13. Once the orientation and depth data were saved, the surgeon put down the CIT and moved to the next step of the experiment.

In order to reduce the number of steps of the experiment as well as to focus on assistive techniques, the depth-estimation techniques using light intensity presented above were not used for guiding surgeons in estimating the depth of the basal turn for AOS depth guidance during the user study. Instead, the surgeons' own expertise was used while visualizing the basal turn manually.

After inspection, the surgeon picked up an electrode and oriented it as if carrying out an electrode insertion, as above. However, in this case, the surgeon was also assisted by a GUI to guide the forceps in order to match the orientation and depth data (s)he just saved using the CIT.

Fig. 3.14 shows the GUI represented in three core zones. Fig. 3.14(a) provides a 3D

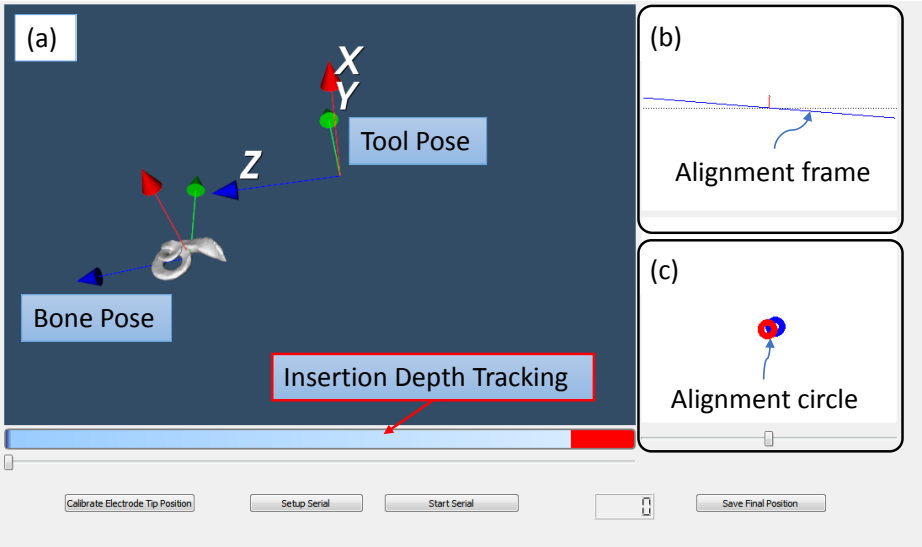

Figure 3.14: A guidance GUI consisting of (a) a 3D display of cochlea and tool tip frames, (b) a graphic guidance zone for roll about the longitudinal axis at the base of the electrode array, (c) a graphic guidance zone for guiding the tool approach vector.

rendering of the electrode tip relative to a desired position at which AOS should start. At the bottom of this zone, the insertion depth is also shown using a horizontal bar that turns red when reaching the pose commensurate with the beginning of AOS. Simultaneously, a buzzer was used to indicate that the surgeon should commence AOS. Fig. 3.14(b) provides the user with information about the roll of the electrode array about the longitudinal axis of its base. Information from the CIT software regarding the previously digitized orientation of the basal turn is used to guide the user to roll the tool such that an alignment frame is aligned having its long axis horizontal and its short axis pointing up. Fig. 3.14(c) provides the user with guidance regarding the tool approach angle into the facial recess. A stationary reference alignment circle is used with another circle to provide cues on tool movement for proper approach angle. The user is instructed to tilt the forceps about the entrance to the facial recess to align the circles.

Using the GUI's auditory and visual feedback, the user placed the electrode array and signalled an assistant to click the appropriate button on the GUI to save the final tool orientation and position, concluding that trial.

3.5.3 Unguided Full Electrode Insertion

A full electrode insertion under standard clinical procedure followed the steps in Section 3.5.1, but with AOS completed. Surgeons were asked to use practice Contour Advance perimodiolar electrode arrays with standard manual tools to insert the EA's into a temporal bone. The surgeons were asked to insert the EA using the standard best surgical practice they use for placement of these arrays using the AOS technique. Tool motions and insertion forces were recorded. A microswitch was attached to a set of tweezers to record when the surgeon began to grab the stylet to start AOS. On a given bone, this was repeated twice to measure forces and the electrode was glued in place on the final trial with cyanoacrylate glue.

3.5.4 Guided Full Electrode Insertion

The surgeon repeated the first steps of cochlear inspection and digitization in Section 3.5.2. However, after the orientation and depth information was recorded, the surgeon carried out a full electrode insertion using those tools as a guide. As in Section 3.5.3, forces and tool positions were recorded for the duration of this experiment. The final electrode was glued in place for CT scanning of final implant placement.

3.6 User Study Results

3.6.1 Insertion Forces

In the full insertion experiments, forces were measured but no significant differences were observed between forces in the guided and unguided insertion experiments (p=0.81). Bones were soaked in a mixed glycerin-saline solution to match the approximate physical characteristics of the perilymph. A mean level of forces throughout the experiments of 1.3 and 1.4 Newtons were observed for the unguided and guided experiments, respectively. These levels of forces, higher than those reported previously in the literature, may be due

to accidental hand-bone contact by the surgeons or contact between the forceps and the bone that may have corrupted the measurements of forces on the cochlea by the electrode itself. Additionally, while the bones were soaked and rewetted in the perilymph-imitating solution, leaking bones and variations in the time of soaking and amount of time the bone was left out while the surgeon was getting set up may have contributed to changed force results.

3.6.2 Approach Angle

Study data was analyzed to measure the overall approach vector of the electrode as it was inserted into the cochlea. The approach vector was intended to be controlled by using the orientation of the CIT during inspection as the optimal insertion vector, but as mentioned above, this angle was not actively guided during experiments due to surgeon feedback, so this dataset can only give a baseline measure of surgeon variability.

Fig. 3.15 shows the results of the insertion vectors, plotted as a polar plot centered at the mean CIT insertion direction from each bone. There was a mean absolute angular difference from the central direction of 21.0° with a standard deviation of 14.5°. This result also agrees with prior results from previous investigations by our research group in [149].

3.6.3 AOS Depth

Assistance features were provided to guide the depth of initiation of AOS, but the results showed a multimillimeter range of insertion depths across individual physicians, individual bones, and the entire dataset and no statistically significant difference between guided and unguided insertions ($p = 0.85$). The results are shown in Fig. 3.16, where the baseline basal turn depth was calculated by inserting the fiber until contact was made with the bone, and the 'depth' was reported as the difference between that depth and the final electrode insertion depth. This maintains a standardized baseline for each bone in the experiment.

There are a number of factors contributing to the lack of statistically significant results

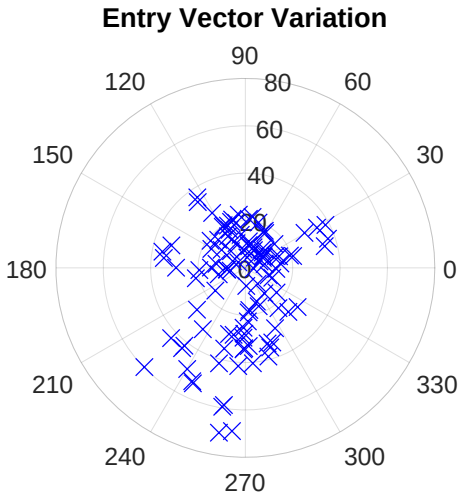

Figure 3.15: The approach angle results show a broad range of insertion directions of the electrode as it enters the cochlea.

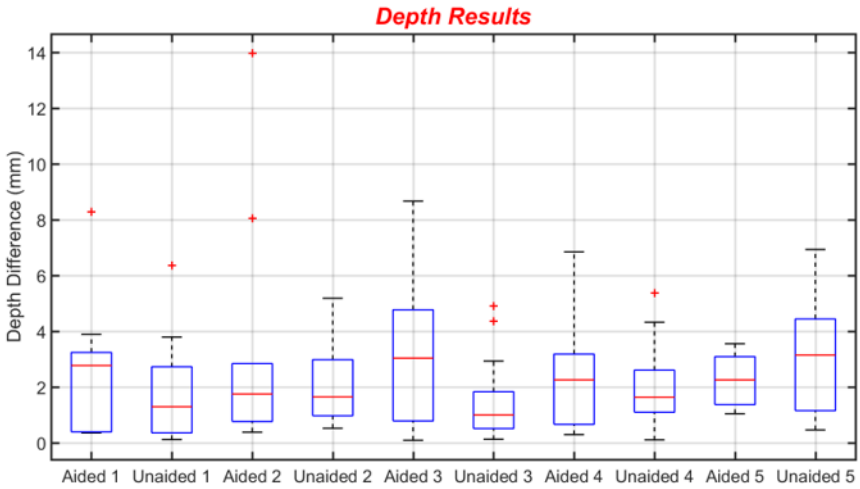

Figure 3.16: Electode insertion depth at AOS initiation for each surgeon, reported as distance between basal turn depth and the chosen AOS initiation depth.

between guided and unguided datasets and why there was a large range of depths found. The selection of a target depth by using the images provided by the CIT was challenging: in a monocular imaging scenario without some kind of stereo vision, it is very difficult to determine depth. Additionally, the images shown are not what surgeons are used to seeing when inserting electrode arrays, so a lack of familiarity inhibited surgeons from choosing repeatable and accurate target depths. The surgeons also performed the insertion while looking through the microscope, which prevented them from viewing the visual interface simultaneously. While a sound cue was used to alert them of reaching the target depth, it was difficult to have their concentration focus on the depth while they were inserting the electrode through the cochleostomy.

The tracking and registration uncertainties reported above may have also contributed to the lack of statistically significant differences and high variability. Lastly, the flexibility of both the CIT and the EA made it so that slight deflections of either caused the depth to be very difficult to control and measure repeatably. Good measurements of flex are unavailable due to the infeasibility of tracking within the cochlea, which would obviate the need for tool tracking at the proximal end of the tool. Large deformations were not expected, as the CIT was intended to be inserted in a straight line through the cochleostomy toward the basal turn. The electrode array similarly should not be bent between calibration and the start of AOS, but these are optimal assumptions that may not always be adhered to in practice.

3.6.4 Basal Turn Orientation

Fig. 3.17 shows the aggregate angular orientation of roll of the electrode compared to the ground truth angle found by CT image segmentation. The leftmost boxplot shows the distribution of angles of the final electrode position without any guidance. The next boxplot displays the angles for the final electrode position with CIT guidance. The third shows the angle chosen by the surgeon using the CIT, and the fourth shows the difference between the second and third boxplots. The detailed results of each of these distributions are discussed

below.

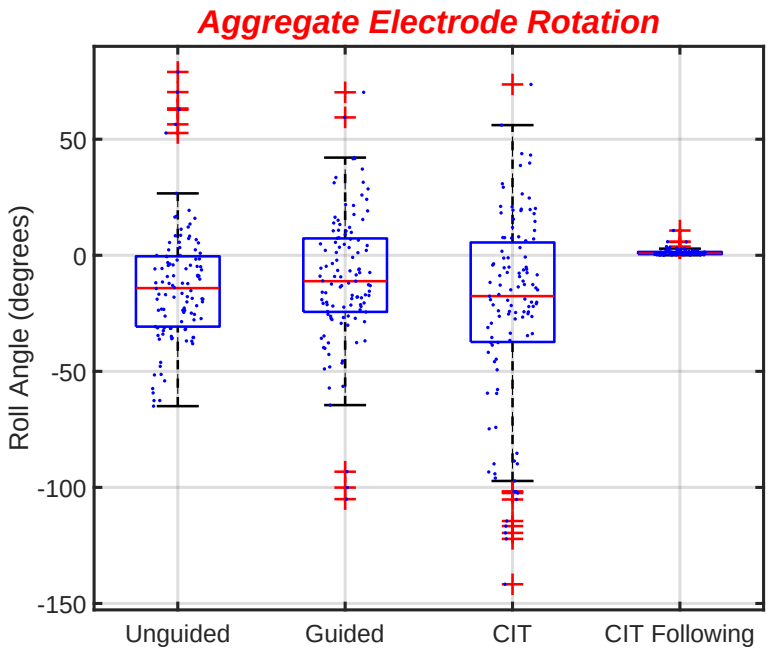

Figure 3.17: The left plots show electrode roll angles for the unguided and guided electrode insertion experiments, the second plot from the right shows the target roll angles chosen by surgeons using the CIT, and the rightmost shows the absolute difference between the previous two plots.

Unguided: In the results for the baseline (no guidance) roll of the electrode, indicating the surgeon's understanding of the orientation of the major axis of the cochlear helix, there was a standard deviation of 32.9° across all surgeons and bones when no guidance was used (first box plot in Fig. 3.17). There was a mean difference, in aggregate across all bones and physicians, of 4.4° degrees between the bending plane as indicated by the electrode position and the plane defined by the cochlea's helical axis as segmented in a CT scan. The root-mean-square (RMS) angular difference between these measurements was 33.0°, showing that while centered close to the ground truth angle, there was a large variation in performance.

Guided: For the guided results (second box plot in Fig. 3.17), the standard deviation was 33.4°, with a mean of $-2.1°$ and an RMS difference of 33.9°. These aggregated results across all surgeons and bones do not indicate a statistically significant difference in mean

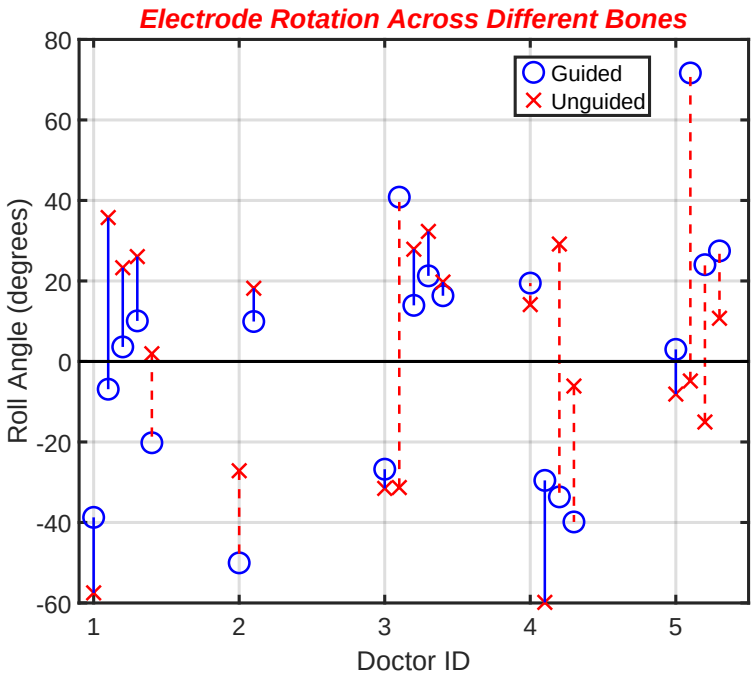

Figure 3.18: Mean unguided and guided electrode roll for each bone and surgeon. Blue lines have a guided result closer to the ground truth, red dashed lines have an unguided result closer to the ground truth.

(p=0.59) or variance (p=0.83) between insertions with and without CIT guidance using a t-test and f-test to test for mean and variance differences, respectively. This means that the use of the CIT did not change the user's behaviour in selecting the roll of the electrode array.

To further compare guided v.s. unguided basal turn orientation (electrode roll), Fig. 3.18 was prepared to show the results of the electrode roll broken down by bone for each physician. The results are grouped by surgeon with each surgeon's experiments on one bone represented by one of the vertical lines. The blue circle marks the mean guided roll angle and the red x marks the mean unguided roll angle. The mean change between unguided and guided results in this set was 0.9°, with an RMS change of 34.1°. The solid blue lines show results where the guided result was closer to the ground truth and the red dashed lines show where the unguided results matched the ground truth better. 11 of the guided results had a closer angle and 9 of the unguided results had a closer angle.

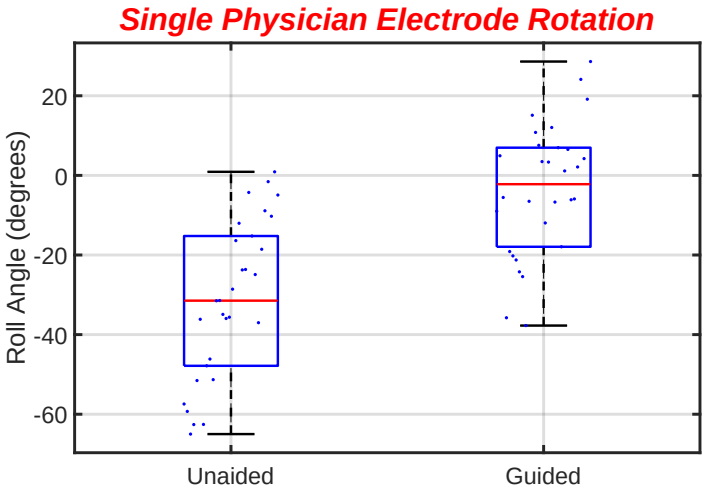

Figure 3.19: Mean unguided and guided electrode roll for preliminary study subject, with significant difference in behavior when using CIT guidance.

The data for Dr. ID #1 was collected as a preliminary dataset to set a baseline for performance and to understand the appropriate amount of data needed to show statistical significance across all the physicians in the trial. This preliminary dataset, which was collected prior to enrolling the other users in the study, is shown in Fig. 3.19. In a t-test of this data, the CIT was shown to significantly change the mean electrode roll orientation ($p < 0.0001, N = 30$).

CIT Inspected: The third boxplot in Fig. 3.17, representing the angle chosen by the surgeon for an optimal insertion as visualized in the CIT, has similar statistics as the previous two with a mean of 3.5°, standard deviation of 34.0° and RMS difference of 34.0°. The similarity of this to the unguided results shows that the ability of visual inspection to choose an orientation of the basal turn was not an improvement over the surgeon's capabilities when using a microscope. However, because of the large RMS error, it does show that the inspection contributed to changes in surgeons' behavior, although not in a systematic fashion.

CIT Following: The rightmost boxplot in Fig. 3.17 shows the absolute difference in the segmented angle of the third boxplot and the final angle in the second boxplot. This

Table 3.2: Electrode roll statistics for all surgeons across different bones, measured in degrees. σ and N designate the standard deviation and the number of samples.

	Bone 1	Bone 2	Bone 3	Bone 4	Bone 5	All Bones
Unguided Mean	$-22.06°$	$-8.42°$	$16.33°$	$16.90°$	$10.82°$	$-4.4°$
Guided Mean	$-18.67°$	$17.19°$	$1.99°$	$4.73°$	$-1.94°$	$-2.1°$
Unguided σ	$28.63°$	$40.01°$	$19.85°$	$19.52°$	$13.21°$	$32.9°$
Guided σ	$30.84°$	$43.01°$	$26.08°$	$29.18°$	$20.48°$	$33.4°$
N	25	25	20	20	10	100

Table 3.3: Electrode roll statistics for all surgeons broken down by individual, measured in degrees. σ and N designate the standard deviation and the number of samples.

	Dr. 1	Dr. 2	Dr. 3	Dr. 4	Dr. 5
Unguided Mean	$-31.3°$	$-15.2°$	$-18.0°$	$12.8°$	$1.9°$
Guided Mean	$-3.4°$	$-27.5°$	$-20.2°$	$25.7°$	$-26.9°$
Unguided σ	$19.9°$	$10.6°$	$22.4°$	$34.5°$	$10.0°$
Guided σ	$16.6°$	$20.6°$	$15.4°$	$19.1°$	$35.7°$
N	30	15	30	20	20

difference represents the ability of a surgeon to orient the electrode to match the desired roll angle segmented using the CIT. This distribution has a mean of $1.3°$, showing that surgeons are able to follow an insertion direction if they are guided using our GUI.

Table 3.2 shows various statistical measures of the electrode roll for each of the bones, across all surgeons who had performed experiments on that bone. Even within a given bone, standard deviations for both unguided and guided insertions are large, up to over $40°$. There is no consistent pattern between the mean orientation of either the guided or unguided result or the difference between the mean results.

The same statistics shown in Table 3.2 per bone are broken down by user in Table 3.3. Standard deviations per physician are overall smaller than those per bone, indicating that, as expected, there is variability coming from both each surgeon's actions and the differences between each surgeon's understanding of the anatomy and surgical approach. This can be seen visually in Fig. 3.20 which presents the electrode roll data for all the surgeons enrolled in the study, broken down into guided and unguided trials.

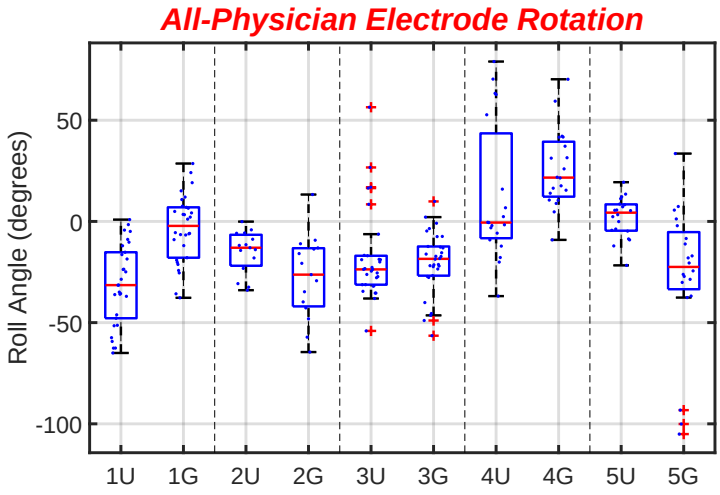

Figure 3.20: Electrode roll across all physicians, boxplots labeled 'U' represent unaided trials, whereas those with 'G' represent guided trials.

3.6.5 Final Placement of Full Insertions

Post implantation CT scans were taken of all bones with electrodes fully inserted in them after the last insertion was finished by each study participant. A previously published software package segmented the different scala of the cochlea and the location of the electrode array [145, 146]. In the guided experiments, 3 out of 5 insertions stayed completely within the ST throughout their length, with one translocation from the ST into the SV and one full insertion into the SV. This was true for only 1 of the 5 unguided results: there were 3 ST to SV translocations and one insertion entirely into the SV. Because of the small sample size, statistical significance of these result cannot be determined. This rate of non-ST insertions is consistent with the literature: studies report rates of placement at least partially outside the ST ranging from 40 to 55% when using the Contour Advance [150, 123].

Fig. 3.21 shows example reconstructed cochlea and electrode shape using the methods in [145, 146] using both preoperative and postoperative imaging and anatomical atlases to estimate the post operative EA placement. Figures (a) and (b) show full ST insertions with and without guidance, Fig. 3.21(c) shows a guided insertion which was fully contained

within the SV, and Fig. 3.21(d) shows an unguided insertion where the EA translocated from the ST to the SV. When interpreting these figures, note that the use of practice electrodes is not representative of Contour Advance arrays used in patients since these practice electrodes have not been inspected and certified by Cochlear Corporation. Also, while the study was designed not to overuse any given specimen, the bones had been used previously for the preceding experiments, which may have resulted in damage or changes to the bone structure through the repeated insertion and removal of EAs and the CIT fiber. This means that, while useful for evaluation between different methodologies, these results may not reflect expectations in a clinical setting.

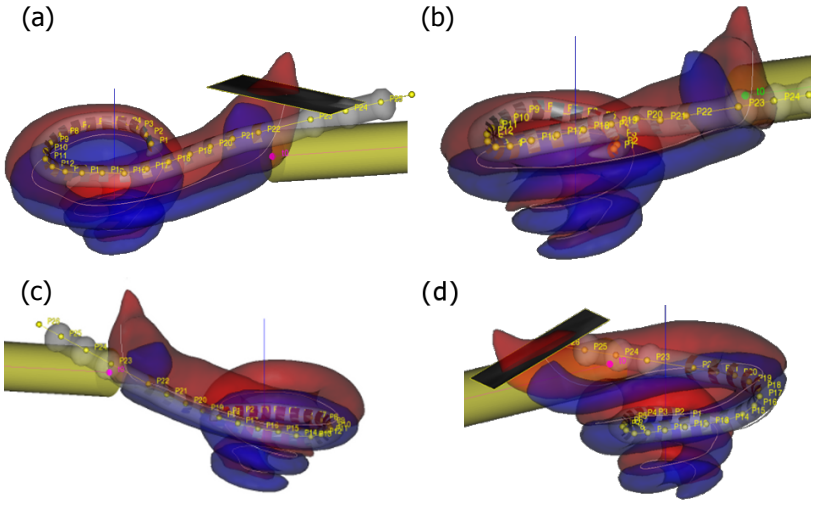

Figure 3.21: Sample results of postoperative scans for final EA placement. (a) Guided full ST insertion, (b) Unguided full ST insertion, (c) Guided full SV insertion, (d) Unguided insertion with ST to SV translocation.

3.7 Conclusion

The delicate nature of the inner ear anatomy provides a difficult challenge for surgeons when inserting electrode arrays, which is hindered by the fact that internal anatomy varies between individuals and is not correlated to external anatomy for a given patient. The high accuracy requirements for atraumatic and effective cochlear electrode array insertion motivated our investigation into new tools for intraoperative anatomical inspection and tool

feedback systems. To this end, we reported baseline variability of a number of EA insertion metrics as well as the change in those metrics when surgeons were guided by a graphical interface and visual cochlear inspection.

The results show a fairly large deviation in the electrode insertion directions: 32.9° in electrode roll and a norm deviation of 21° in electrode approach vector. When using intracochlear inspection with software assistance to help guide electrode AOS depth and electrode roll, it was found that the results were not statistically different from the no-assistance experiments.

However, as seen in the last boxplot in Fig. 3.17, the reason the CIT guidance does not seem to affect surgeon activity is not that surgeons are unable to follow the angles they chose during visualization, it is rather that they are not used to intracochlear visualization and as such do not have the ability to make consistent and informed decisions based on this type of information and select a wide variety of angles even when given images of the intracochlear anatomy. With more training, it is possible that the CIT would allow surgeons to become more consistent - more data would have to be taken and training activities studied to make any conclusions.

There is reason to believe training may help in the use of the CIT for electrode roll guidance because of the above significant results for Dr. ID #1 shown in Fig. 3.19. This user had the most experience with the tool, having assisted with some of the software development for user-friendliness of the interface and having given feedback on early iterations of the ergonomics of the tools and setup. This user was subjected to repeated contact with the setup and the use of the visualization tool over a long period prior to taking data. This long exposure with the system may have played a factor in the user's statistically significant final electrode orientation result, pointing to the potential for training as one avenue of improvement of this method.

Visual inspection may be effective with more training because when the results are separated by surgeon, for many of the bones, there is a large effect of the CIT on the orien-

tational result. While the mean difference between unguided and guided experiments of the surgeons' electrode orientations was 0.9°, the root-mean-square difference was 34.1°. This means that, while in aggregate it looks like the CIT did not affect the orientation across all the experiments, in fact it did affect surgeon behavior, but sometimes in a clockwise direction and sometimes in a counterclockwise direction, as seen in Fig. 3.18. This points to the inspection as something that gives surgeons more data and the ability to change their behavior, but since it is a new modality there is no training to know how to implement changes based on this information.

While surgeons generally reported they understood what they were seeing in the images, the current technology level for fiberscopes is a hindrance to providing a large amount of information. If there is more development in higher resolution imaging tools that could look past the basal turn, such technology may provide a better understanding of the anatomy and clearer images to the surgeons.

Despite the lack of significance in the changing of behavior with visual information in guiding electrode orientation during surgery, surgeons were able to follow visual cues in electrode roll to match a desired insertion orientation of the electrode to within less than 2°. This suggests that future work integrating other sources of realtime information for providing feedback and guidance will have success in improving repeatability of EA insertion.

One potential source of patient-specific anatomical information is the use of preoperative imaging, especially computed tomography (CT) scans. The role of CT in cochlear implant surgery is still being evaluated, with recent studies investigating the costs and benefits of their routine use with no clear conclusions thus far [151]. In addition to the costs associated with routine CT scans, there would be a need for attaching screws into the skull for registration between the CT scan and the intraoperative scene. This presents a hurdle that, while not more invasive than a mastoidectomy, would increase patient discomfort between imaging and the procedure, so must be taken into account before using preoper-

ative imaging to accompany intraoperative feedback unless other registration methods are found. Future work with imaging specialists can enable tracking based on preoperative data to investigate the utility of this approach.

This work motivates the need for future investigation into guidance techniques due to the wide variability between surgeons in electrode approach. For any given cochlea and electrode array shape, there will be a set of insertion parameters to optimally insert the array. However, in current practice, surgeons deviate from one another, and even themselves across repeated trials, greater than 30° in certain measures. There is a large amount of room for future improvement in tool tracking and guidance for improving electrode array insertion.

This chapter has presented the design of an inspection tool and accompanying software to assist in the insertion of perimodiolar electrode arrays into the cochlea to improve surgical outcomes in cochlear implant surgery. While in many experiments the inspection tool changed surgeon behavior, because of the subjectivity involved in its use, it was unable to create statistically significant differences in insertion behavior across many surgeons and experiments. However, surgeons were able to follow insertion cues quite well during a procedure, so if cues about insertion behavior were generated by preoperative imaging, it would be expected that more significant results could be found. Experiments also established baseline performance metrics for surgeons' insertion of electrode arrays: that their surgical parameters are quite variable in a few different respects. Future work should expand on the results of this investigation to integrate other sources of information for guidance and a wider range of electrode arrays.

CHAPTER 4
CONTINUUM ROBOT ORGAN PALPATION

Continuum robots have been investigated for surgical applications due to safety benefits stemming from their inherent compliance and their ability to support dexterity and miniaturization for surgery [8]. Various types of continuum robot architectures for medical applications have been proposed including concentric tube robots [152, 153], tendon-driven robots [154], and multi-backbone continuum robots (MBCRs) [155]. MBCRs are made of segments actuated by pushing and pulling on superelastic nickel-titanium backbones (termed secondary backbones) which are spaced radially around a central backbone and kept at a fixed distance to the central backbone by spacer disks. While the choice of a particular continuum robot architecture depends on the desired clinical application, MBCRs can withstand larger forces than concentric tube robots or catheters, making them attractive for new approaches in single port laparoscopic surgery. Alongside the developments in MBCRs which enable high-force interaction, researchers have also been investigating methods for utilising force sensing during surgery. For these reasons, this chapter focuses on the use of MBCRs during robot-environment interaction in RAMIS.

The chapter starts with an exploration of using continuum robots for organ palpation, an extension of the methods presented in [84]. For this investigation, the challenges in intrinsic force sensing were put to the side to focus on palpation/trajectory profiles and intelligent integration of force sensing and tip tracking for soft organ interaction. Evaluation is performed on the Insertable Robotic Effectors Platform (IREP), a two-armed MBCR designed for single port or natural orifice surgery. Each arm includes two continuum segments, a planar five-bar parallelogram linkage, an insertion stage, and a wrist.

This chapter is organized into 5 sections. Section 4.1 presents the motivating background and prior art. Section 4.2 describes the kinematic framework used to analyze

the motion of MBCRs. Sections 4.3 and 4.4 describe a mixed feedback controller and experiments using that controller for organ palpation for intraoperative registration. Some difficulties of this framework and opportunities for future work are discussed in section 4.5.

4.1 Continuum Robot Palpation Background

During RAMIS, accurate registration between the pre-operative model containing the surgical plan and the intraoperative surgical scene enables key capabilities such as virtual fixtures for assistive telemanipulation and semi-autonomous execution of surgical tasks. However, between planning/imaging and surgery, organs shift and deform due to gravitational loads and changing boundary conditions with neighboring organs due to surgical dissection. This chapter explores the feasibility of using continuum robots for autonomous scanning and registration of organ geometry to pre-operative information. Continuum robots are chosen for this task as a representative example among minimally invasive robotic devices that allow deep reach into the anatomy (e.g. catheters and wire-actuated snake-like robots).

The need to reconcile pre-operative data to the intraoperative surgical field has motivated many years of research on deformable registration. A summary and classification of deformable registration techniques is available in [156]. The majority of deformable registration works focus on using intra-operative imaging or computer-vision/laser scanning (e.g. [157]) to achieve the data needed to update the organ registration and surgical plan. Force-controlled exploration/palpation offers new capabilities for registration: palpation enables simultaneous use of geometry and stiffness for registration, in addition, palpation with continuum robots can reach anatomy out of the field of view of other imaging/vision tools and investigate areas obscured by blood or other fluids. Future force-controlled exploration should be used to augment information from 3D vision or laser scanning. To prove feasibility of this method, we limit the scope of this work to exploring and overcoming challenges in geometry-based registration based on force controlled exploration using

continuum robots.

The use of force-controlled exploration of organ shape was proposed in [158], where effects of scan patterns on the accuracy of shape estimation were explored. Recently, in [159] the use of force-controlled exploration for achieving deformable registration and updating the geometry of a virtual fixture was presented with implementation on a rigid Cartesian stage robot and using the daVinci research kit (dVRK). This work extends these efforts by expanding the robot architectures where feasibility of this approach has been tested. While the Cartesian robot has very high accuracy and no deflections and the dVRK slave has good accuracy [160] (within 1.5 mm) and small deflections, a typical continuum robot will have poor accuracy and significant deflections, thus motivating new approaches in robot control to overcome these challenges.

The accurate registration of a preoperative surgical plan allows for updating virtual fixtures and (semi) autonomous execution of surgical tasks: examples where these capabilities are useful include force- and velocity-controlled ablation along a path and (semi) autonomous suturing. In addition to accurate registration, an accurate kinematic model is required for semi-automated task execution in the absence of end effector sensing. This is difficult for continuum robots which often have poor accuracy. Telemanipulation can overcome these issues via user supervision with sub-millimetric accuracies attainable [161], but that is separate from the use of accurate virtual fixtures or task automation. This work follows the mixed-feedback approach in [162] by sensing the end effector position and closing the loop with a magnetic tracker at the robot tip.

4.1.1 Contribution

The main contribution of this chapter is an updated framework for mixed feedback control for continuum robot interaction with soft environments. The prior work in [84] presented a hybrid force/position control framework for continuum robots by carrying out the task decomposition in configuration space of the continuum robot and relying on

using a model of the configuration space stiffness of the continuum robot. While the approach has been shown to be effective for continuum robots, it does present several challenges due to reliance on motion decomposition in configuration space of the continuum robot. Specifically, if a robot has a combination of continuum segments and non-continuum segments (e.g. the parallelogram linkage in Fig. 5.1), this approach of motion decomposition in configuration space can be burdensome to implement due to the large discrepancy in stiffness between the different joints. Another challenge that we address in this work is the fact that when controlling force with a continuum segment, one may wish to define redundancy resolutions that improve the force sensing capabilities via JEFS. In [84] the inversion of task to configuration space Jacobian occurs in both branches of the hybrid force/motion controller, which can be challenging when one considers redundancy resolution task specification for improving JEFS sensing capabilities.

To address these challenges, we switch the control framework to use hybrid admittance/position control while avoiding the use of task decomposition at configuration space and instead, we rely on task space formulation. This overcomes the limitations outlined above and has the advantage of also offering robustness to uncertainty in the configuration space stiffness since force regulation is achieved through a closed-loop position control relying on an admittance feedback law.

4.2 Kinematic Model

We use the kinematic framework for MBCRs proposed in [163], noting that many kinematic modeling methods for circular-bending continuum robots have also been proposed [164, 165, 153]. Fig. 4.1 and Table 4.1 display the main kinematic variables and matrices used in the kinematic analysis.

The task-space position of the end-effector and joint-space position of the robot joints are represented by $\mathbf{x}$ and $\mathbf{q}$. These are supplemented with a configuration vector represent-

Symbol	Description
$\mathbf{J}_{ab}$	A Jacobian mapping such that $\dot{\mathbf{a}} = \mathbf{J}_{ab}\dot{\mathbf{b}}$ where $\dot{\mathbf{x}}$ designates the time derivative of $\mathbf{x}$
$\mathbf{q}$	A single segment joint space displacement (amount of push/pull on secondary backbones). $\mathbf{q} \in \mathbb{R}^{4\times1}$
$\mathbf{q}_a$	Augmented $\mathbf{q}$ for two-segment robot, $\mathbf{q}_a \in \mathbb{R}^{8\times1}$
ψ	A single segment configuration space vector $\psi = [\theta, \delta]^{\mathrm{T}}$, characterizing the bending angle and bending plane angle; shown in Fig. 4.1. $\psi \in \mathbb{R}^{2\times1}$
ψ_a	Augmented ψ for two-segment robot. $\psi_a \in \mathbb{R}^{4\times1}$
$\boldsymbol{\tau}$	Single-segment secondary backbone actuation forces $\boldsymbol{\tau} \in \mathbb{R}^{4\times1}$
$\boldsymbol{\tau}_a$	Augmented $\boldsymbol{\tau}$ for two-segment robot. $\boldsymbol{\tau}_a \in \mathbb{R}^{8\times1}$
$\dot{\mathbf{x}}$	Task space vector of positional and orientational velocities. $\dot{\mathbf{x}} \in \mathbb{R}^{6\times1}$
$\mathbf{w}_e$	External wrench acting on the end-effector of the robot. $\mathbf{w}_e \in \mathbb{R}^{6\times1}$
∇E	Gradient of the elastic energy E with respect to the configuration perturbation $\Delta\psi_a$

Table 4.1: Nomenclature for kinematics and statics in force sensing formulations

ing the shape of the robot. The shape of the i^{th} segment of a robot is represented as:

$$\psi_i = [\theta_i,\ \delta_i]^{\mathrm{T}} \tag{4.1}$$

θ_i describes the bending angle of the tip of the i^{th} segment of the robot and δ_i describes the bending plane in which the segment is bent. A visual representation of these angles is shown in Fig. 4.1A.

The configuration vector for a two-segment snake is described as $\boldsymbol{\psi_a} = \left[\boldsymbol{\psi}_1^{\mathrm{T}},\ \boldsymbol{\psi}_2^{\mathrm{T}}\right]^{\mathrm{T}}$. Using this vector, a Jacobian describes the relationship between configuration space and joint space velocities:

$$\dot{\mathbf{q}}_a = \mathbf{J}_{q_a\psi_a}\dot{\boldsymbol{\psi}}_a \tag{4.2}$$

where $\dot{\mathbf{q}}_\mathbf{a}$ is the linear velocity of the actuated joints of the entire robot as detailed in Section 4.2.1 in the appendix. The Jacobian $\mathbf{J}_{q_a\psi_a}$ is given in equation (4.6) of Section 4.2.1. A task-to-configuration space mapping can also be found as:

$$\dot{\mathbf{x}} = \mathbf{J}_{x\psi_a}\dot{\boldsymbol{\psi}}_a, \tag{4.3}$$

where $\dot{\mathbf{x}}$ is the task space velocity and $\mathbf{J}_{x\psi_a}$ is given in equation (4.10) in Section 4.2.2.

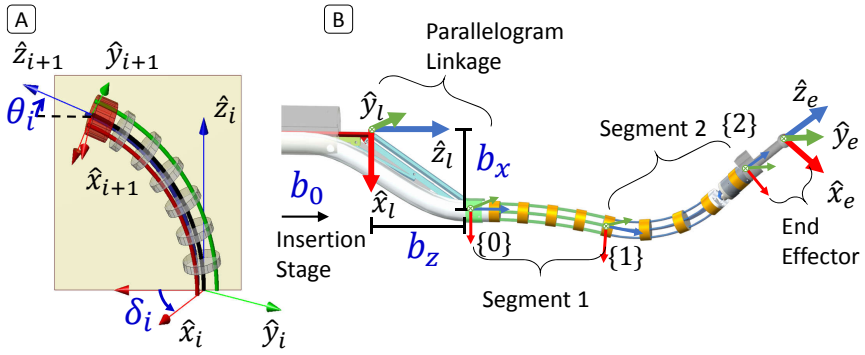

Figure 4.1: The IREP's robot state is represented by the variables in blue. A) The bent angle (θ_i) and bending plane (δ_i) define the configuration space vector ψ for each segment B) The insertion stage displacement, b_0 and parallelogram linkage opening movements (b_x and b_z) position the base of the continuum arm. Frames representing the linkage base, the robot base, the 1st and 2nd segments, and end-effector are designated as l, 0, 1, 2, and e, respectively.

These Jacobians, $\mathbf{J}_{q_a\psi_a}$ and $\mathbf{J}_{x\psi_a}$, are used for describing and controlling the kinematics of the robot as well as for deriving the energetic relationships that govern the force sensing model.

It is useful to describe motions and control directions in the robot base frame $\{0\}$, as seen in Fig. 4.1B, and defined as parallel to $\{1\}$. The z axis of this frame is defined as running along the longitudinal axis of the robot arm when straight. The x axis is aligned with the direction the workspace-expanding linkage is opened, and the y axis, according to the right hand rule, points "downward" away from the stereo module.

4.2.1 Inverse Kinematics

The inverse kinematic mapping between configuration space and joint space is described by a kinematic relationship that relates the amount of bending to the length of the secondary backbones. For the i^{th} segment of the robot with nominal length L_i, the length of the j^{th} secondary backbone, L_{ij}, can be represented as:

$$L_{ij} = L_i + q_{ij} = L_i + \Delta_{ij}(\Theta_i) \tag{4.4}$$

where q_{ij} is the length change of the jth secondary backbone in the i^{th} segment and $\Theta_i \triangleq \theta_i - \frac{\pi}{2}$. θ_i is purely a function of the backbone lengths and does not require an assumption of circular bending of the snake [155]. For the jth secondary backbone, $\Delta_{ij} = r\cos(\delta_i + \sigma_j)$, where $\sigma_j = (j-1)\frac{2\pi}{m}$, and m is the total number of backbones of the robot ($m = 4$ for the IREP).

The augmented joint space vector for the entire robot $\mathbf{q}_a$, is slightly different from a vector of all the q_{ij} variables because the secondary backbones of distal segments must pass through the first segments. The joint space vector $\mathbf{q}_a$ is therefore represented as $\mathbf{q}_a \triangleq [q_{11},\, q_{12},\, q_{13},\, q_{14},\, q_{11}+q_{21},\, q_{12}+q_{22},\, q_{13}+q_{23},\, q_{14}+q_{24}]^{\mathrm{T}}$.

The instantaneous inverse kinematic relationship between joint and configuration space for the i^{th} segment is derived by differentiating (4.4):

$$\mathbf{J}_{q\psi_i} = \begin{bmatrix} r\cos(\delta_i) & -r\sin(\delta_i)\,\Theta_i \\ -r\sin(\delta_i) & -r\cos(\delta_i)\,\Theta_i \\ -r\cos(\delta_i) & r\sin(\delta_i)\,\Theta_i \\ r\sin(\delta_i) & r\cos(\delta_i)\,\Theta_i \end{bmatrix} \quad i = 1,2 \tag{4.5}$$

Because of the aforementioned passthrough of the secondary backbones, backbones of proximal segments must be actuated in tandem with the bending of the distal segments. In the kinematic model, this is achieved by using a lower triangular Jacobian for the entire snake. Therefore, using the two-segment augmented configuration vector $\boldsymbol{\psi}_a = \left[\boldsymbol{\psi}_1^{\mathrm{T}},\, \boldsymbol{\psi}_2^{\mathrm{T}}\right]^{\mathrm{T}}$, the augmented joint space Jacobian is:

$$\dot{\mathbf{q}}_a = \mathbf{J}_{q_a\psi_a}\dot{\boldsymbol{\psi}}_{\boldsymbol{a}}, \quad \mathbf{J}_{q_a\psi_a} = \begin{bmatrix} \mathbf{J}_{q\psi_1} & \mathbf{0} \\ \mathbf{J}_{q\psi_1} & \mathbf{J}_{q\psi_2} \end{bmatrix} \tag{4.6}$$

4.2.2 *Forward Kinematics*

For the i^{th} continuum segment, the position, ${}^{i-1}\mathbf{p}_i$, and orientation, ${}^{i-1}\mathbf{R}_i$, of that segment's tip relative to its base frame can be represented as:

$$ {}^{i-1}\mathbf{p}_i = \begin{bmatrix} \frac{L\cos(\delta_i)\,(\sin(\theta_i)-1)}{\Theta_i} \\ -\frac{L\sin(\delta_i)\,(\sin(\theta_i)-1)}{\Theta_i} \\ -\frac{L\cos(\theta_i)}{\Theta_i} \end{bmatrix} \tag{4.7} $$

$$ {}^{i-1}\mathbf{R}_i = \begin{bmatrix} c_{\Theta_i}c_{\delta_i}^2 + s_{\delta_i}^2 & c_{\delta_i}s_{\delta_i} - c_{\delta_i}s_{\delta_i}c_{\Theta_i} & -c_{\delta_i}s_{\Theta_i} \\ c_{\delta_i}s_{\delta_i} - c_{\delta_i}s_{\delta_i}c_{\Theta_i} & c_{\delta_i}^2 + c_{\Theta_i}s_{\delta_i}^2 & s_{\delta_i}s_{\Theta_i} \\ c_{\delta_i}s_{\Theta_i} & -s_{\delta_i}s_{\Theta_i} & c_{\Theta_i} \end{bmatrix} \tag{4.8} $$

For a given segment, the instantaneous forward kinematics can be found by differentiating the forward kinematics for a single segment.

$$ \mathbf{J}_{x\psi_i} = \begin{bmatrix} L\cos(\delta_\text{i})\left(\frac{\cos(\theta_\text{i})}{\Theta_i} - \frac{\sin(\theta_\text{i})-1}{(\Theta_i)^2}\right) & -\frac{L\sin(\delta_\text{i})\,(\sin(\theta_\text{i})-1)}{\Theta_i} \\ L\sin(\delta_\text{i})\left(\frac{\sin(\theta_\text{i})-1}{(\Theta_i)^2} - \frac{\cos(\theta_\text{i})}{\Theta_i}\right) & -\frac{L\cos(\delta_\text{i})\,(\sin(\theta_\text{i})-1)}{\Theta_i} \\ \frac{L\cos(\theta_\text{i})}{(\Theta_i)^2} + \frac{L\sin(\theta_\text{i})}{\Theta_i} & 0 \\ -\sin(\delta_\text{i}) & \cos(\delta_\text{i})\cos(\theta_\text{i}) \\ -\cos(\delta_\text{i}) & -\sin(\delta_\text{i})\cos(\theta_\text{i}) \\ 0 & \sin(\theta_\text{i})-1 \end{bmatrix} \tag{4.9} $$

To obtain the kinematics for the entire snake:

$$ \dot{\mathbf{x}} = \mathbf{J}_{x\psi_a}\dot{\psi}_a, \quad \mathbf{J}_{x\psi_a} = \begin{bmatrix} \mathbf{S}_1\mathbf{J}_{x\psi_1} & \mathbf{S}_2\mathbf{J}_{x\psi_2} \end{bmatrix} \tag{4.10} $$

Where $\mathbf{S}_1$ and $\mathbf{S}_2$ are screw transformation matrices constructed as:

$$\mathbf{S}_1 = \begin{bmatrix} \mathbf{I} & [{}^{\mathbf{0}}\mathbf{p}_{\mathbf{1}} - {}^{\mathbf{0}}\mathbf{p}_{\mathbf{e}}]^{\wedge} \\ \mathbf{0} & \mathbf{I} \end{bmatrix} \tag{4.11}$$

$$\mathbf{S}_2 = \begin{bmatrix} {}^{0}\mathbf{R}_1 & [{}^{\mathbf{0}}\mathbf{p}_{\mathbf{2}} - {}^{\mathbf{0}}\mathbf{p}_{\mathbf{e}}]^{\wedge} \\ \mathbf{0} & {}^{0}\mathbf{R}_1 \end{bmatrix} \tag{4.12}$$

where ${}^{0}\mathbf{p}_2$ and ${}^{0}\mathbf{p}_e$ are the vectors of the end of the 2nd segment and the robot end-effector in frame $\{0\}$, $\mathbf{I} \in \mathbb{R}^{3x3}$ is an identity matrix, and $[\cdot]_{\times}$ is the skew-symmetric cross product matrix of a vector.

4.3 Mixed Feedback Control for Continuum Robot Palpation

To perform semi-automated surgical tasks or to assign virtual fixtures for telemanipulated surgical procedures, accurate correspondence between preoperative and intraoperative organ geometry is required. This section presents the use of force-controlled exploration by a MBCR to update organ geometry using the deformable registration of a pre-operative model to the surgical scene to overcome organ deformation and shift relative to pre-operative images. Since continuum robots can offer deep access into the anatomy, the unique challenges associated with their use to achieve force-controlled exploration are explored. A mixed feedback control law is proposed whereby a combination of joint-level control and end-effector position measurements are used to satisfy a reference motion trajectory. A hybrid force/position controller is presented using sensory input from magnetic tracking and force sensing. Experimental results show that, despite deformation of an organ, the surgical plan can be deformably registered using force-controlled exploration data via an implementation of coherent point drift registration.

Palpation is achieved using the IREP; for this work, only the right arm is used, equipped with a spherical palpation probe end-effector for environment exploration and location feedback from a magnetic tracking marker. Full design and modeling details for the kine-

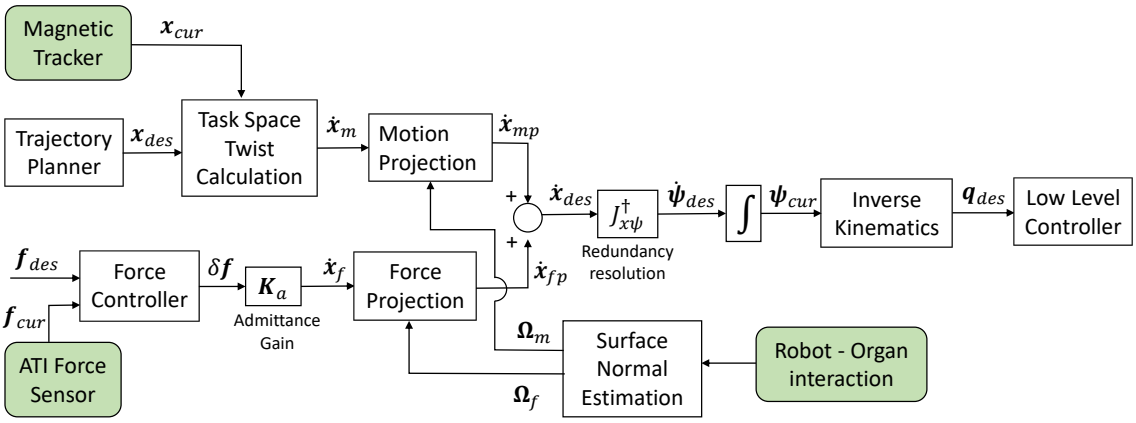

Figure 4.2: IREP control framework including hybrid-force position control, redundancy resolution, and environment estimation.

matics of this robot are available in [166, 167].

A control framework is developed to achieve blind force-controlled exploration and registration with a update of the hybrid-force position law found in [84]. The block diagram of this control framework appears in Fig. 4.2. Prior work on updating virtual fixture geometry by using palpation data [159] is extended by implementing the exploration and registration using a continuum robot, which motivates a change in the framework for motion and force control to allow success of force-controlled organ exploration.

4.3.1 Full Arm Kinematic Model

The instantaneous kinematics of the full IREP arm shown in Fig. (5.1,4.1) was presented in [168] and is an extension of the general MBCR kinematics presented in Section 4.2. Additional configuration variables are added to the robot configuration: the insertion of the arm, b_0, and the x and z positions of the five-bar linkage, b_{1x} and b_{1z}, control the position the base of the continuum segments. These variables form a robot configuration variable $\boldsymbol{\Psi_r}$:

$$\boldsymbol{\Psi_r} \triangleq \begin{bmatrix} b_0 & b_{1x} & b_{1z} & \theta_1 & \delta_1 & \theta_2 & \delta_2 \end{bmatrix}^{\mathrm{T}} \tag{4.13}$$

The instantaneous kinematics are solved in (4.14), using the Jacobian $\mathbf{J}_{\mathbf{x}\Psi_r}$ mapping configuration space and task space velocities as defined in [167]. Following a resolved rates control method, the desired configuration space velocity $\dot{\Psi}_r$ is solved based on the desired task velocity $\dot{\mathbf{x}}$.

$$\dot{\mathbf{x}} = \mathbf{J}_{\mathbf{x}\Psi_r}\dot{\Psi}_r \;\Rightarrow\; \dot{\Psi}_r = \underbrace{\mathbf{W}^{-1}\mathbf{J}_{x\Psi_r}^{\mathrm{T}}\left(\mathbf{J}_{x\Psi_r}\mathbf{W}^{-1}\mathbf{J}_{x\Psi_r}^{\mathrm{T}} + \varepsilon\mathbf{I}\right)}_{\mathbf{J}_{x\Psi_r}^{\dagger}}\dot{\mathbf{x}} \tag{4.14}$$

The configuration space velocity is integrated to determine the current configuration variables. The configuration variables are directly mapped to joint space variables by use of inverse kinematic relationships with actuation compensation from [169] and a coordination control module. A PID controller is then used to control joint positions $\mathbf{q}$.

The singularity robustness parameter ε was defined in accordance with [170] and set to:

$$\varepsilon = \begin{cases} 0 & \theta_1 \leq 87^\circ \\ 0.01 & 87^\circ < \theta_1 < 90^\circ \end{cases} \tag{4.15}$$

This redundancy resolution formulation was shown earlier in [167]. We note that in (4.14), a weighted least norm solution is used to solve for the joint velocities. The matrix $\mathbf{W}$ is a weight matrix used for avoidance joint limits following the method in [171].

4.3.2 Task Space Controller

For a simple environment exploration task (point contact), there is no need to restrict the full orientation of the robot end-effector, so only a select portion of the task space velocity is commanded. Assuming the IREP is placed horizontally, three Cartesian velocities and a single degree of rotational velocity ω_y around the vertical axis (y) are commanded, describing a four degree of freedom task. The specifics of this task are described below. The task subspace velocities, $\dot{\tilde{\mathbf{x}}}$, are converted to configuration space velocities by combining

translational Jacobian and the y-axis row of the orientation Jacobian:

$$\dot{\tilde{\mathbf{x}}} \triangleq \begin{bmatrix} \dot{\mathbf{p}} \\ \omega_y \end{bmatrix} = \underbrace{\begin{bmatrix} \mathbf{J}_{\mathbf{p}\psi_r} \\ \mathbf{J}_{\omega_y\psi_r} \end{bmatrix}}_{\mathbf{J}_{\tilde{x}\Psi_r}} \dot{\Psi}_r, \quad \dot{\tilde{\mathbf{x}}} \in \mathbb{R}^4 \tag{4.16}$$

$\mathbf{J}_{\mathbf{p}\Psi_r}$ designates the rows of the Jacobian relating to Cartesian velocity, and $\mathbf{J}_{\omega_y\Psi_r}$ the row relating to angular velocity about the robot base's y axis. Originally, only Cartesian position was controlled; the control of ω_y was added after early experiments in which side collision between the base of the end-effector and the anatomy was observed.

To control the orientation of the robot tip for the exploration task, we define an auxiliary frame $\{\hat{\mathbf{u}}\hat{\mathbf{v}}\hat{\mathbf{w}}\}$, as shown in Fig. 4.3. This frame has its $\hat{\mathbf{w}}$ axis along the projection of the local tangent to the desired motion path onto the horizontal plane, its $\hat{\mathbf{u}}$ axis along the cross product between $\hat{\mathbf{w}}$ and the upward-pointing vertical axis, and its $\hat{\mathbf{v}}$ axis along the downward-pointing vertical. An angle γ is defined as the angle between the gripper axis $\hat{\mathbf{z}}_g$ and the $\hat{\mathbf{v}} - \hat{\mathbf{w}}$ plane. To facilitate the calculation of γ, we define a projection matrix $\mathbf{\Omega}_{uw}$ to create a projection of $\hat{\mathbf{z}}_g$ onto the $\hat{\mathbf{u}} - \hat{\mathbf{w}}$ plane, designated as $\check{\mathbf{z}}_g$:

$$\check{\mathbf{z}}_g \triangleq \mathbf{\Omega}_{uw}\hat{\mathbf{z}}_g, \quad \mathbf{\Omega}_{uw} \triangleq \mathbf{I} - \hat{\mathbf{v}}\hat{\mathbf{v}}^{\mathrm{T}} \tag{4.17}$$

By replacing $\dot{\mathbf{x}}$ with $\dot{\tilde{\mathbf{x}}}$ and $\mathbf{J}_{\mathbf{x}\Psi_r}$ with $\mathbf{J}_{\tilde{\mathbf{x}}\Psi_r}$ and using (4.14), a reduced-dimension redundancy resolution is solved for $\dot{\Psi}$. The Cartesian velocity, $\dot{\mathbf{p}}$, is commanded as a linear function of position error with a maximal velocity limit. To calculate the desired rotation of the end-effector we keep $\hat{\mathbf{z}}_g$ in the $\hat{\mathbf{v}}$-$\hat{\mathbf{w}}$ plane by minimizing γ to prevent the organ collision problem mentioned above. This is controlled by rotation about the $\hat{\mathbf{v}}$ axis, so only one degree of freedom needs to be commanded for rotational motion, leaving the other degrees free for redundancy resolution or to avoid joint limits and increase the effective workspace of the robot.

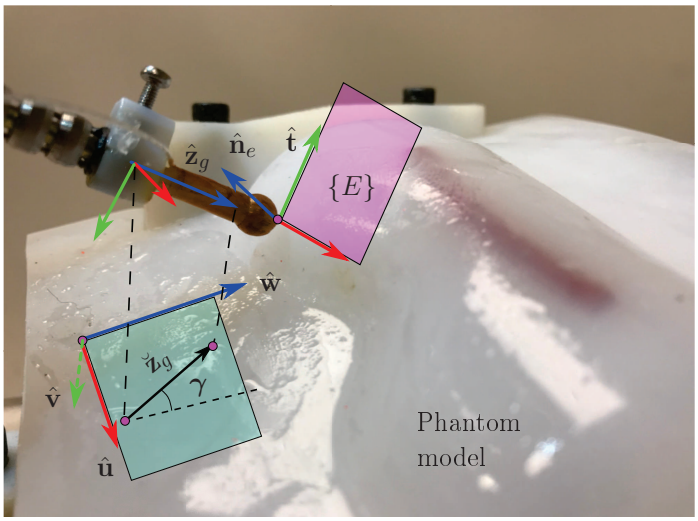

Figure 4.3: The IREP is shown probing an organ at point E. $\hat{\mathbf{n}}_e$ designates the current estimated organ normal at E, and $\hat{\mathbf{t}}$ the current tangential motion direction. The longitudinal axis of the end-effector is shown as $\hat{\mathbf{z}}_g$. Its projection onto the $\hat{\mathbf{u}}$-$\hat{\mathbf{w}}$ plane, $\check{\mathbf{z}}_g$, is used to define the angle γ. The angular velocity of the end-effector is defined to minimize the bending of the end-effector out of plane (γ), to prevent organ collision.

The angular speed ω_y to minimize γ is specified using a proportional gain k_γ:

$$\omega_y = k_\gamma \sin(\gamma) \tag{4.18}$$

While $\hat{\mathbf{u}}$, $\hat{\mathbf{v}}$, and $\hat{\mathbf{w}}$ can be defined in the moving frame of the robot with orientational velocity calculated in the end-effector frame by making use of the body Jacobian of the robot, for these experiments it was kept in the base frame of the robot and aligned with the pre-planned raster trajectory.

4.3.3 Admittance-Based Hybrid Force/Position Control

Fig. 4.2 shows the hybrid force-position controller used for force-controlled exploration. This control framework is a modification of the method presented in [84] to use an indirect admittance controller. A simple PI controller is used to calculate $\delta\mathbf{f}$ based on the errors between the reference and current measured force. Using a constant admittance

gain, a task space velocity is generated.

$$\mathbf{K}_a \delta \mathbf{f} = \dot{\mathbf{x}}_f \tag{4.19}$$

This approach presents two improvements over a previously presented controller for hybrid force/position control of a continuum robot relying on a parametrization of robot joint stiffness [84]. When motion is a function of both flexible continuum segments and the relatively stiff joints of the parallelogram linkage and insertion stage, it is difficult to model and adjust the modeled joint stiffness to achieve coordinated motion of the robot without also estimating and calibrating a continuum stiffness model or iterative tuning of stiffness parameters based on experimental results. Moving the stiffness to task space by using an indirect admittance controller instead of a direct joint-space force controller alleviates this problem.

Additionally, this formulation combines the force and position controllers in task space, creating a unified task space command. The previous formulation used two task-to-configuration space conversions (one for force and one for position), whereas this controller has a single conversion which allows for solving a unified redundancy resolution problem which can be used to avoid joint limits or accomplish other subtasks which would be more difficult to accomplish in the previously presented framework.

A hybrid force-motion controller with task decomposition as proposed in [172] is used to explore the environment. Commands are formulated as the sum of orthogonal force and motion directions, controlled by separate force and motion controllers. Orthogonalization is achieved via the projection matrices $\mathbf{\Omega}_m$ and $\mathbf{\Omega}_f$ used to project the task-space errors in motion and force directions, respectively:

$$\mathbf{\Omega}_f = \begin{bmatrix} \hat{\mathbf{n}}_e \hat{\mathbf{n}}_e^{\mathrm{T}} & 0 \\ 0 & 0 \end{bmatrix}, \quad \mathbf{\Omega}_m = \mathbf{I} - \mathbf{\Omega}_f \tag{4.20}$$

$$\dot{\mathbf{x}} = \mathbf{\Omega}_m \dot{\mathbf{x}}_m + \mathbf{\Omega}_f \dot{\mathbf{x}}_f \tag{4.21}$$

where $\dot{\mathbf{x}}_m$ and $\dot{\mathbf{x}}_f$ are the desired end effector speeds to close the errors in the motion and force control loops, respectively, and $\hat{\mathbf{n}}_e$ is the contact normal along which we control force. The next important question is how to define the contact normal $\hat{\mathbf{n}}_e$ during blind exploration of an unknown organ.

4.3.4 Force Control Direction Update

To traverse non-flat environments before a model is generated, it is necessary to update the force control direction of the hybrid controller during task execution. In a known environment, it is simple to define the force control direction as the local surface normal direction and the motion direction according to (4.20). However, when performing blind exploration where the robot does not know the environment model, the force control direction $\hat{\mathbf{n}}_e$ must be updated online. The method presented here echoes that developed in [159, 173]. The outline of the frames used in our update framework is shown in Fig. 4.3.

The nominal force control direction is estimated as the current direction of the vector describing the force felt on the robot, $\mathbf{f}$. The forces are fed through a 1KHz 25-point moving average to reduce noise and prevent sudden changes in the control direction. We restrict the force controller to only act in the $\hat{\mathbf{v}}$-$\hat{\mathbf{w}}$ plane of the frame defined in Fig. 4.3 to prevent forces in a transverse direction to the desired motion trajectory from pulling the robot off course. This is achieved with the use of a projection matrix $\mathbf{\Omega}_{vw}$, defined similarly as in (4.17), replacing $\hat{\mathbf{v}}$ with $\hat{\mathbf{u}}$. The control direction is calculated as:

$$\hat{\mathbf{n}}_e = \mathbf{\Omega}_{vw} \frac{\mathbf{f}}{||\mathbf{f}||} \tag{4.22}$$

The above estimate of $\hat{\mathbf{n}}_e$ was saturated to prevent it from tilting more than 60° relative to the vertical. This limitation was applied to reflect an *a-priori* guess of the steepest slope in organ geometry. Future work should include an update for simultaneous friction

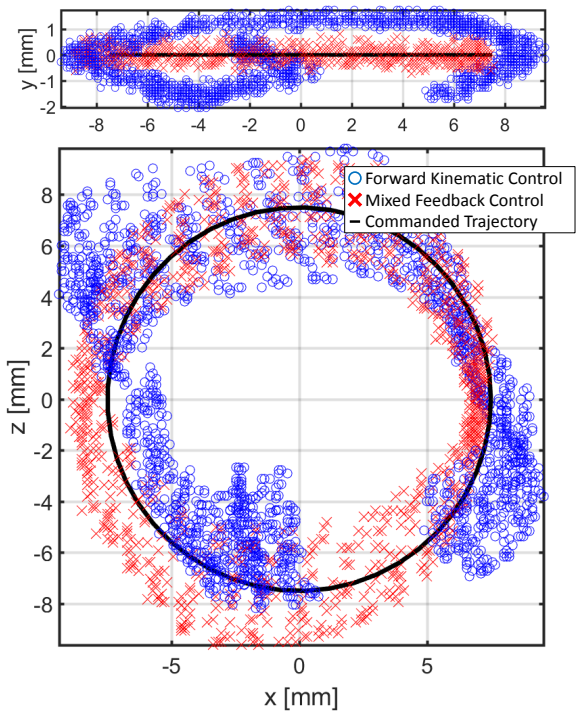

Figure 4.4: Characterization of trajectory-following error under mixed feedback and forward kinematic control. Mixed feedback errors plotted in red, forward kinematic errors in blue. RMS error reduced from 1.89 to 1.12 mm using mixed feedback control

estimation while interacting with unknown flexible geometry.

4.3.5 Mixed Feedback Controller for Closed Loop Control

The IREP was equipped with a magnetic sensing coil to provide feedback about the end-effector tip position during robot-organ interaction. While geometric calibration attempts may help decrease kinematic uncertainty in free space, a full model including large deformations due to environment contact has yet to be developed. Therefore, a "mixed feedback" controller was implemented to provide a desired motion command that is computed based on a mixture of an internally-updated robot Jacobian that relies on integration of the configuration variables and an externally-updated set of position measurements.

This is described as a "mixed" controller because the external commands based on magnetic tracking close a loop in task space, but not in configuration space. The internal model of the geometry of the robot, as known by the current configuration ψ, does not

	Mixed Feedback	Forward Kinematics
RMS Error	1.12	1.89
Max Error	2.72	4.66
Error Standard Deviation	0.52	0.76

Table 4.2: Comparison of error between mixed feedback controller and for the uncalibrated forward kinematics controller. All errors are reported in millimeters.

update to match the deflected pose of the robot as it makes contact. The Jacobian-based velocity relationships derived for a robot in free space are still good enough approximations to control the robot during contact and deflection. This is similar in concept to the idea of "endpoint feedback" or "endpoint control" which has been presented in the literature for other flexible robotic systems [174].

The task description in the trajectory planner and the task space error calculations were all performed using measurements from the tracker to close the loop and calculate the desired configuration velocity as per (4.14). After the configuration space velocity was computed, commands were sent to the joint-level motors using the robot's inverse kinematics. The configuration variables were integrated based on their commanded velocities to update the Jacobians at the next time step. We refer to this framework as a "mixed" controller because the magnetic sensor measurements do not estimate or update the pose of the robot in configuration space, but still drive the desired control velocity in task space.

Free-space trajectory following experiments were carried out to characterize the performance of the mixed feedback controller. The robot was commanded to follow a circle under both mixed feedback control and using forward kinematics to update the robot pose. As shown in Fig. 4.4, the mixed feedback controller reduced trajectory-following errors, calculated as the distance between each point saved by the sensor during the scan and the closest point along the circular trajectory. Errors are reported for a sampling frequency of 125 Hz without any filtering. By adding the mixed feedback control, the root mean square (RMS) errors were reduced from 1.89 mm to 1.12 mm in the circle tracking task. The magnetic tracker itself had significant noise: without any motion, we calculated an RMS

noise level of 1.41 mm in free space. Our measurements showed the sensor noise was larger in the vertical direction, which aligns with the trajectory direction in the side regions of the trajectory in Fig. 4.4. This alignment of noise and trajectory direction explains how the trajectory-following error (1.12 mm) is smaller than the norm sensor noise (1.41 mm).

4.4 Mixed Feedback Organ Exploration

The experimental setup can be seen in Fig. 4.5. A phantom kidney created out of molded silicone was mounted onto a plastic base which is slanted in two non-parallel planes to deform the organ. The silicone kidney was fabricated by casting liquid silicone rubber (Ecoflex 00-30) onto a 3D printed mold. The mold geometry was used to define an a priori map of the undeformed organ geometry. The base was affixed to an ATI Gamma force sensor. An Ascension 3D Guidance trakSTAR magnetic tracking system was used to measure the position of the end-effector of the robot. The quality metric of the trakSTAR 2 system, which reports magnetic interference, was not significantly affected at the site of organ interaction by the presence of the force sensor underneath the organ holder.

The control framework introduced above was used to carry out force-controlled exploration of the organ. A raster path in the base plane of the magnetic tracker was used to create a desired trajectory for the robot to follow. The organ was brushed with glycerin to provide lubrication to mimic the fluids found in a surgical setting. A constant force of 0.3 Newtons was commanded to the robot throughout the scan. Once the scan of the organ was completed, the measurements from the magnetic tracker were used to perform a deformable registration from an *a priori* mesh of the organ to the explored data. A video of this palpation can be seen in Multimedia Extension 1, linked from Appendix A.4.

The raster scan was aligned along the major axes of the magnetic tracker, which also correspond to trajectories that largely follow either an "uphill" or "downhill" direction relative to the silicone organ. This kept the plane of motion aligned with the major required directions of force control. The results of this scan are shown in Fig. 4.6.

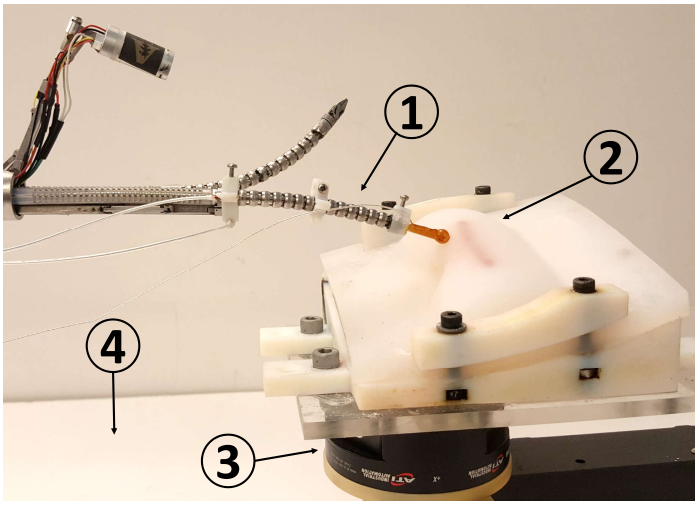

Figure 4.5: The experimental setup of the IREP scanning a silicone phantom. (1) The continuum arm of the IREP with magnetic tracker embedded in the tip (2) silicone phantom kidney (3) ATI gamma force sensor(4) Ascension trackSTAR magnetic tracking base plate

The total scan time for the front of the organ, covering an approximately 5 cm x 3 cm polygon, was approximately 19 minutes. The scan time can be decreased; less dense results with an increased trajectory velocity obtained similar results in less than 10 minutes. Even this is a relatively long scan time: further work will need to be done to decrease scan time to achieve clinically viable scan methods for large areas. For smaller areas, this framework can be used for semi-automation of regulated palpation of specific anatomical regions for further exploration. Such areas may be defined by expert user input or areas obscured by blood or other fluids that may have positional uncertainty when scanned by vision or other imaging modalities.

4.4.1 Organ Deformable Registration

Fig. 4.6 presents the registered data. The a priori model was deformably registered to the magnetically tracked exploration data using a point-based deformable registration method, coherent point drift (CPD) [175]. To compensate for the noisy position measurements of the magnetic sensor, a zero-phase moving average filter of 15 points was applied to all the scan data. In addition, since there were instances when the robot lost contact with

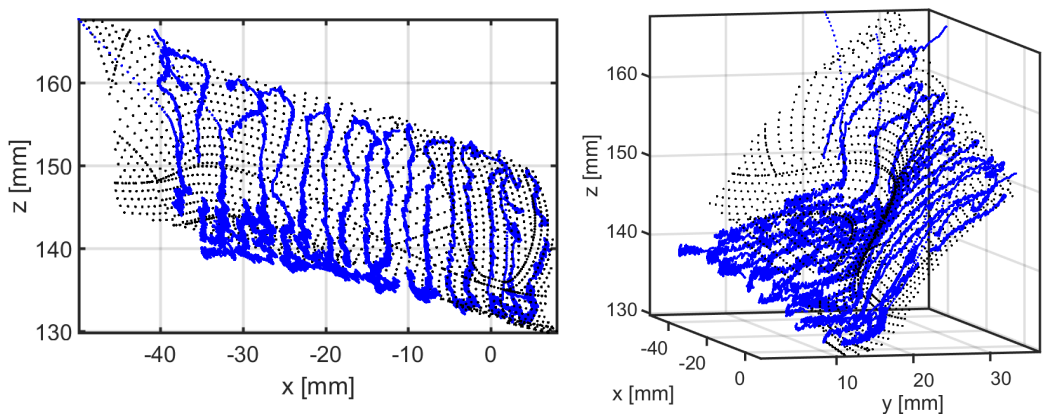

Figure 4.6: Position of the robot while scanning the organ and resulting deformed map of the organ geometry. The positions of the robot during the force-controlled organ scan are shown as the blue lines. The deformable registration using Coherent Point Drift is shown as the black points.

the organ, any points where measured contact force fell below 0.15 N were removed from consideration in the registration dataset.

The CPD algorithm is based on deforming points in one point cloud to positions within a second point cloud, which makes formulating an inverse transform difficult. Since it was desired to perform analysis and task execution in the magnetic tracker frame, the a priori scan of the organ was designated as the "moving" data set, and the magnetic tracking scanned results from the robot as the "target" data set. Since correspondence is required for each of the points in the moving set, the a priori model was trimmed to be approximately the same size and shape as the explored data. Since the algorithm regularizes for deformation energy to reduce overfitting, the trimming did not need to match the explored region exactly, but this manual step in the registration algorithm greatly improved registration from an untrimmed model while also introducing a measure of subjectivity into the registration process.

4.4.2 Ground Truth Comparison

In order to characterize the errors in the registration, we used a FARO Fusion laser scanner to obtain a ground truth measurement of the deformed organ geometry. Spherical

fiducials were placed in the magnetic tracker workspace and scanned with the laser scanner and a tracked probe containing an electromagnetic marker. These fiducials were used to register the frame of the laser scanner to the frame of the magnetic tracker. A small scaling factor between the two measurement systems was found to be necessary to reduce the registration error.

With the registration between the laser scanner and the electromagnetic tracker computed, the deformed map and the laser scan can be compared directly as shown in Fig. 4.7. Comparing the scans, there was an average RMS error between the laser-scanned surface and the deformed a priori model of 1.75 mm. If a rigid registration was used in place of the deformable CPD algorithm, this error increased to 2.33 mm. These errors include registration errors from the laser scanner to the magnetic tracker. This is comparable to results estimated when using a laser-scan endoscope system with errors of 1-1.5 mm in a laparoscopic context [157].

While the estimated surface normal used for control, $\hat{\mathbf{n}}_e$, was projected and filtered to improve performance, it is also useful to see how the direction of the force vector relates to the direction of the surface normal. The angular errors between the unit norm vector of the force felt during the organ scan and the normal vector of the closest point on the registered point cloud from the laser scan were calculated, and the RMS error was found to be 11.88 degrees. This shows that, while not exact, for a well-lubricated surface, the force direction vector is close to the surface normal direction.

4.5 Challenges In Mixed Feedback Palpation

There are a number of challenges that need to be overcome to enable better force-guided robotic palpation and to enable the extraction of more information from such procedures.

There were instances where the robot lost contact with the organ during scanning. One particular cause of this is the elastic energy held in both the robot and the organ. When moving up very steep regions of the phantom, the force controller pushes in a largely

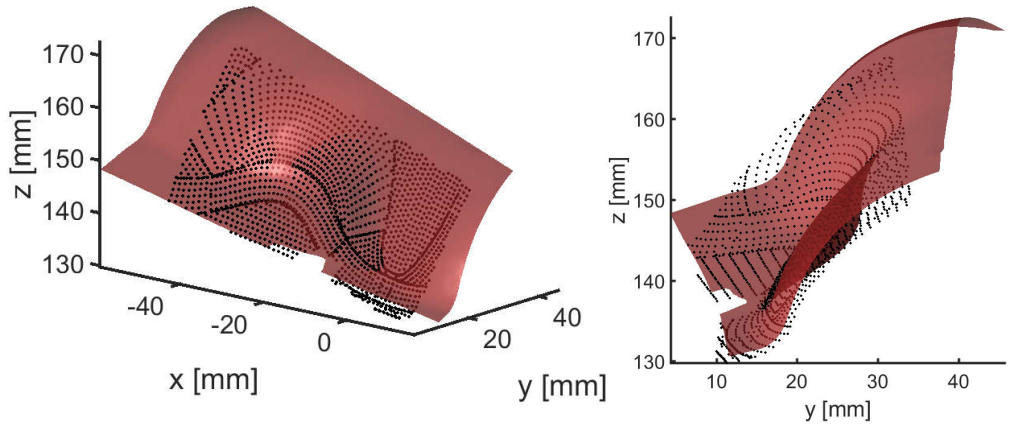

Figure 4.7: A comparison of the deformed a priori map to a laser scan of the deformed organ. The red surface is the result of a laser scan of the deformed organ in place. The black dots are points along the deformed a priori map of the organ calculated using the force-controlled palpation. RMS error between the maps is 1.75 mm

horizontal direction. This bends the continuum structure of the robot which then can "pop" out of the organ as it crests the hill, straightening significantly. The robot subsequently returns to the scanning trajectory, but a more complete compliance framework will need to be formulated and integrated into a control framework to compensate for this stored energy and to prevent rapid changes in robot shape.

The organ palpation in this investigation was carried out both "uphill" while moving away from the robot base and "downhill" while moving toward the robot base. The former motion was much more difficult, causing the afore-mentioned "popping" out of the organ's surface caused by the robot jabbing into the environment surface. To allow time for the force controller to converge and prevent high-force interaction, the lateral scan speed was reduced, causing the scan time to increase significantly. In the experiments in the next chapter, palpation was performed with the robot always moving toward the robot base to avoid this jabbing motion (regardless of environment shape - uphill or downhill) and to allow for faster-speed scans while covering similar-sized or larger areas.

While the presented method was able to traverse even steep areas of the organ, the trajectory followed by the robot often had errors from the planned raster pattern as it moved

up and down the surface. Lack of friction compensation and the flexible nature of the environment contributed to these errors. A more robust exploration framework should estimate relevant parameters to compensate for these effects and reduce these errors during blind exploration.

Additional important areas for exploration include organ stiffness estimation, methods for capturing more complicated physical organ properties, and on-line updates of geometry or registration parameters. Online estimates of the deflected robot shape and identification of multi-point contact will also be useful for broader applicability of this method.

4.6 Conclusions

The palpation control method showed the feasibility of continuum robots to scan unknown geometry elastic environments and to form updated geometry models of the environment using deformable registration. An updated hybrid force-motion and admittance controller for a continuum robot was introduced to improve robot control efficacy for this task. The coherent point drift deformable registration algorithm was shown to be able to update an a priori environment model using the exploration data for the execution of further tasks requiring an updated model such as telemanipulation virtual fixtures or semi-autonomous ablation along a path or in a patch. Results of the deformable registration suggest that force-controlled exploration data may be feasible for updating the geometry of the environment and that the error in estimating the surface normal was less than 12°.

While controlling palpation for continuum robots is itself an advancement of the literature, it is also important to be able to include sensing modalities that can be integrated into the robotic system so as not to have to rely on external force sensing. This problem is explored in the next chapter, leveraging the methods for interaction and control developed in this chapter.

CHAPTER 5
CONTINUUM ROBOT FORCE SENSING AND CONTROL

5.1 Overview

This chapter builds on the method first presented by Xu and Simaan on what was called "intrinsic force sensing" [52, 53] that relies on loadcell readings at the actuators of a multi-backbone continuum robot and a virtual work law. Dealing with uncertainties and model inaccuracies is a key challenge in continuum robot applications, especially in cases where force sensing is required in the presence of friction that can accompany clinically deployable robotic systems. Overcoming these uncertainties is the focus of this chapter.

This chapter has a number of important contributions. Next, an intrinsic force sensing method is presented that can account for nonlinear and path-dependent uncertainties from long, high-friction actuation lines that are more representative of conditions found in clinically deployable systems than previous explorations in the literature. An updated force-sensing formulation is presented as well as model-calibration parameters for higher accuracy sensing. This is validated through automated experiments and a user study of simulated surgical tasks.

This chapter is organized as follows: Section 5.2 describes the motivation for this work, Section 5.3 describes the modeling and control framework for joint-level force sensing. Sections 5.4 and 5.5 present the results of automated experiments and a user study using that joint-level force sensing method for feedback. Sections 5.6 and 5.7 close the chapter with a discussion and concluding remarks.

5.2 Motivation and Prior Art

Many works have investigated the utility of using environment interaction forces to better understand environment properties. Since 2008 [176], researchers have been using

probing [177, 85, 178] and continuous palpation [179, 180] to identify organ geometry, perform registration, and estimate stiffness maps that allow identification of important sub-surface features. Because of the deep reach into the anatomy that continuum structures can provide, vision systems may be partially occluded, and arms may touch the environment in a variety of locations, so force-sensing is especially important in continuum robot systems.

5.2.1 Background for Continuum Force Sensing

Intraoperative force sensing methods can be broadly separated into *direct* and *indirect* methods. Direct methods rely on force sensors held by or attached to the robot's end effector, whereas indirect methods use a model of the robot to estimate the forces from other information sources. Direct methods can provide "drop-in" solutions with high resolution but have disadvantages in tool sterilizablility, cost, and miniaturization. While sensors for direct sensing methods generally must be located *in-situ* (close to the end effector and within the confines of the anatomy), indirect methods can use sensors located *ex-situ* and may use external imaging, tip tracking, or shape measurement for the estimation of applied forces. Indirect methods with ex-situ sensors are attractive since they can help reduce surgical tool cost while overcoming challenges in miniaturization, MRI-compatibility and sterilizability.

Prior works on force sensing for MBCRs have predominantly used indirect *ex-situ* force sensing, referring to estimation of end effector forces via measurement of backbone joint-level forces as "intrinsic force sensing" [52, 53, 181]. Instead of using this restrictive terminology, we will use the term *joint-level ex-situ force sensing* (JEFS).

MBCRs present an opportunity in force sensing due to the larger range of forces they can withstand, but also present serious challenge for JEFS due to force transmission uncertainties. In this work, we focus on two research problems related to the feasibility of JEFS with systems that have large force transmission uncertainties due to friction and hysteresis:

- **Problem 1:** *Uncertainty cancellation in configuration v.s. joint-space:* Methods of

applying uncertainty cancellation terms for frictional losses can be applied at the model-level in joint space or in configuration space for continuum robots[1]. It is not clear whether the application of model correction should be carried out at the joint-space level or configuration-space level.

- **Problem 2:** *Limits of model-based compensation:* It is also unclear to what extent model-based compensation can work without the use of some machine learning methods for capturing nonlinear model uncertainties that are confounded by the presence of multiple hysteresis planes.

These questions are investigated through modeling of kinematics and JEFS and experimentation on the Insertable Robot Effectors Platform (IREP), shown in Fig. 5.1. The IREP is a dual-armed MBCR with a stereo camera system that can be used for single-port surgery [182]. Unlike prototype MBCR designs which have direct routing from joint-level actuators to the continuum segments, the IREP's nitinol backbones must be routed through a number of conduits. They pass through an antisymmetric "cone" which routes the backbones from the linear actuators to their positions within the continuum segment, then through a long stem and a passive segment attached to a workspace-enlarging parallelogram linkage before entering the continuum segments. The cone, stem, and parallelogram linkage, necessary for the realization of a compact system that can be clinically deployable, introduce uncertainties in the static analysis of backbone forces, which motivates the exploration of methods to adapt JEFS to systems with similar actuation line transmission uncertainties. The IREP is actuated by twin-leadscrews to reduce the number of motors in the actuation unit, leading to coupled control of the backbones in each continuum segment.

[1]The *configuration space* of MBCRs is detailed in Section 4.2. It is a vector comprised of pairs of angles used to parameterize the bending shape of each continuum segment.

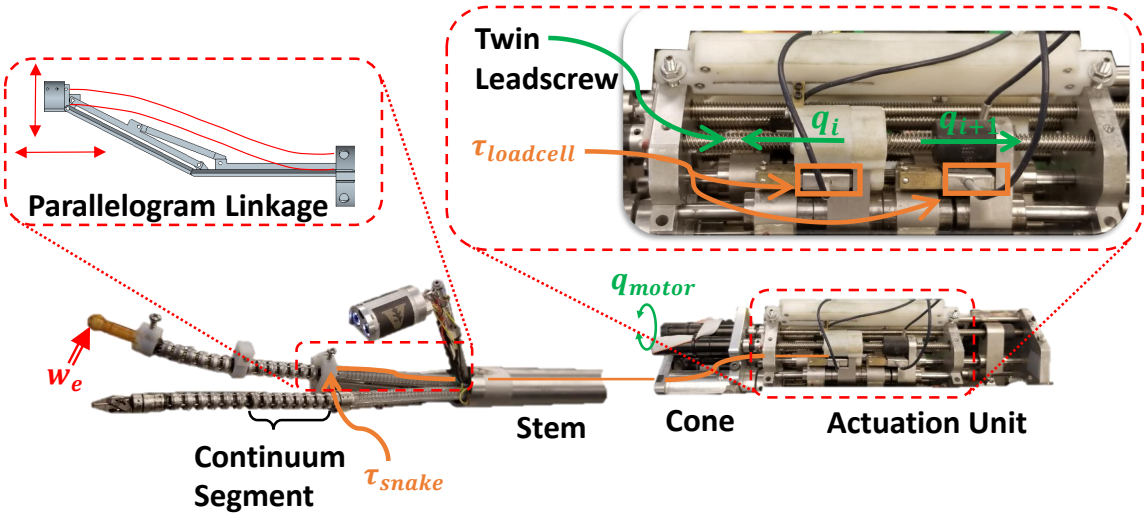

Figure 5.1: Force sensing method for the IREP: measurements of backbone forces in the actuation unit, $\tau_{loadcell}$, are used to estimate backbone forces in the snake, τ_{snake}, to account for losses and uncertainty caused by the routing (shown in orange) of a backbone through the cone, stem, and parallelogram linkage. Backbone forces are used to estimate external tip wrenches, $\mathbf{w}_e$. The secondary backbones of the continuum segments are actuated via q_{motor} turning a twin leadscrew, actuating both q_i and q_{i+1}.

5.2.2 Related Sensing Works

Over the last two decades, a large number of works have focused on enabling force sensing during robot-assisted surgery as reviewed in [32, 183]. This emphasis stems from the fact that the benefits of haptic feedback during surgery as demonstrated in [59, 60, 61, 65] cannot be effectively realized without reliable intraoperative force sensing and feedback. The benefits of intraoperative force sensing have been explored for numerous surgical tasks including suturing [72, 73], catheter insertion [71], cardiac ablation [184], palpation for detection of tumors or hidden anatomy [70], and blunt dissection [64]. Force feedback can also reduce the incidence of adverse events: excessive intraoperative forces can damage sensitive anatomy [185] and improper suturing can damage organs through limited bloodflow [25] or lead to blood leakage due to loose suturing [26].

In [186] indirect control of end-effector stiffness was implemented for a concentric tube continuum robot. The approach relied on a Cosserat rod model of the robot and

tracker measurement of the end effector location. To achieve a desired stiffness, the robot's interaction force was estimated using the static Cosserat-rod model. In this work, we implement JEFS for an MBCR and adopt the indirect force control approach for its robustness of knowledge of the environment's local geometry.

Previous methods for force-sensing in concentric tube robots and catheters have used indirect force sensing methods with sensed loads in many papers not exceeding 0.3 N. A notable outlier is [184] which used a catheter with a combination of a tip-mounted force sensor and ultrasound guidance to maintain tip forces at the level of 1 N. Errors have ranged from 5-20% of maximum reported loads with some papers reporting maximum forces as small as 0.1 N. This includes methods using numerical solvers to estimate a single force at the tip of a flexible beam using shape detection methods ranging from image segmentation [187, 188, 189], combined wire tension and tip position estimation [190], electromagnetic tip tracking [191, 192], or fiber Bragg grating sensors [41].

5.2.3 Contribution

While feasibility of JEFS was demonstrated on bench-top MBCRs with straight backbone routing [52, 53], the constraints of clinically deployable systems often dictate a complex backbone routing which amplifies frictional transmission losses. Previous works on characterizing frictional transmission losses in MBCRs have recently used Support Vector Regression (SVR) [181, 84], or model-based estimation with actuation compensation [193], however these methods have not been adapted to enabling JEFS on less-ideal systems that respect clinical deployability constraints.

Within the broader context of extending JEFS to non-ideal systems, this work presents what we believe is the first effort to explore the two research problems outlined above. In answering these questions posed by these two problems, we also make additional contributions. We present several improvements for accounting for actuation line uncertainties. A previously presented friction regression model is reformulated in joint space instead

of configuration space and we encode hysteretic effects by defining an operator akin to the hysteron operator [194] and including it in an uncertainty regression framework based on support vector regression. Methods for model calibration are presented to improve automated force estimation and task execution.

5.3 Force Sensing Model

JEFS allows continuum robots to sense forces during environment interaction, giving robots the above-mentioned benefits of indirect, ex-situ force sensing. The overall approach is shown in Fig. 5.1: an external wrench on the end-effector, $\mathbf{w}_e$, causes a reaction at the base of the snake that changes the tensions in the backbones. The backbone forces at the base of the snake, $\boldsymbol{\tau}_{snake}$, cannot be directly measured due to space constraints, so instead $\boldsymbol{\tau}_{loadcell}$ is measured inside the IREP actuation unit. However, uncertainty and losses from the backbone routing through the cone, stem, parallelogram linkage, and inside the continuum segments must be accounted for to make sure that load cell measurements can be used to estimate $\mathbf{w}_e$.

The force sensing model is based on the basic force sensing equations introduced in [52]. A virtual work law describes the energy balance under quasi-static conditions:

$$\mathbf{w}_e^{\mathrm{T}} \Delta\mathbf{x} + \boldsymbol{\tau}_{snake}^{\mathrm{T}} \Delta\mathbf{q}_a = \Delta E \tag{5.1}$$

Where $\Delta\mathbf{x}$ is the change in task space end effector pose, $\Delta\mathbf{q}$ is the change in joint space variables, and ΔE is the change in internal energy of the snake. Kinematic Jacobian matrices are used to express $\Delta\mathbf{x}$ and $\Delta\mathbf{q}$ using changes in configuration space, $\Delta\boldsymbol{\psi}$ and ∇E_a (the gradient of the bending energy with respect to $\boldsymbol{\psi}_a$).

$$\mathbf{w}_e^{\mathrm{T}} \mathbf{J}_{x\psi_a} \Delta\boldsymbol{\psi}_a + \boldsymbol{\tau}_{snake}^{\mathrm{T}} \mathbf{J}_{q_a\psi_a} \Delta\boldsymbol{\psi}_a - \nabla E_a^{\mathrm{T}} \Delta\boldsymbol{\psi}_a = \mathbf{0} \tag{5.2}$$

Since (5.2) holds for any arbitrary virtual displacement $\Delta\psi$, we obtain:

$$\mathbf{J}_{x\psi_a}^{\mathrm{T}}\mathbf{w}_e = \nabla E_a - \mathbf{J}_{q_a\psi_a}^{\mathrm{T}}\boldsymbol{\tau}_{snake} \tag{5.3}$$

Equation (5.3) is the fundamental force-sensing equation which, for a single-segment robot, is under-constrained and can be solved by finding the least-norm solution, or by utilizing *a priori* information to estimate the contribution of null-space projection terms [52]. While the approach in (5.3) assumes quasi-static conditions, it was shown in [195] that dynamic motion effects may be neglected for small continuum robots, and a method for including dynamic effects was presented that could be applied to high-friction scenarios as part of potential future work. In [193], adjustments to the static model for multi-segment moment coupling were investigated that would affect this framework. However, due to the complications this presents in the modeling framework and the additional effort involved in solving both moment and frictional coupling effects (the latter of which has not been explored), this work is limited to investigation of force sensing for single segment motion.

In this work, we assume a point contact with the environment since this is a good approximation for tasks such as force-controlled ablation with the robot tip. Therefore, when we estimate the wrench $\mathbf{w}_e$ we use the a-priori knowledge that the moment components should be zero and we seek to only estimate the force vector.

In the following discussion we will use the notion of a generalized force $\mathbf{f}_g$ as used in [181]:

$$\mathbf{f}_g \triangleq \mathbf{J}_{x\psi_a}^{\mathrm{T}}\mathbf{w}_e \tag{5.4}$$

Since the generalized force was defined for a virtual displacement in configuration space, (5.3) shows that this force has the same units as the gradient of the robot's bending energy, i.e. [J/rad].

5.3.1 Joint Space Compensation:

The presence of friction, kinematic uncertainties, backbone extension, and flex inside the actuation lines results in inaccuracies in (5.3). Previously, [181] compensated for uncertainty with generalized forces in configuration space, which do not have a direct physical meaning. An alternate formulation with compensation in joint space is proposed to more directly account for the manifestation of the actuation-level uncertainties without mediating measurements through Jacobians that introduce additional uncertainty. This method reduced fitting errors, especially when investigating the effects of hysteresis.

By rearranging the basic force sensing equation under a no-load condition ($\mathbf{w}_e = 0$), and ignoring uncertainties, (5.3) for an *ideal* single-segment system becomes:

$$\nabla E_a = \mathbf{J}^{\mathrm{T}}_{q_a \psi_a} \boldsymbol{\tau}_{energy} \tag{5.5}$$

where $\boldsymbol{\tau}_{energy}$ represents the backbone forces required to bend the continuum segment at a given pose.

For a non-ideal system (i.e. with friction) (5.5) is modified as the following. A generalized force $\mathbf{f}_g$ is added to the model to represent frictional losses as they manifest in configuration space. Similarly an additional joint-space term $\boldsymbol{\tau}_{friction}$ is added:

$$\nabla E_a + \mathbf{f}_g = \mathbf{J}^{\mathrm{T}}_{q_a \psi_a} \underbrace{\left(\boldsymbol{\tau}_{energy} + \boldsymbol{\tau}_{friction}\right)}_{\boldsymbol{\tau}_{nl}} \tag{5.6}$$

$\boldsymbol{\tau}_{nl}$ is the "no load" measured backbone force, i.e. when $\mathbf{w}_e = 0$. It is assumed to depend on the robot's configuration ψ and its motion history.

If a nonzero $\mathbf{w}_e$ is added to the model, a corresponding increased backbone tension must be added to the model to balance that load, $\boldsymbol{\tau}_{load}$ resulting in the relationship:

$$\mathbf{J}^{\mathrm{T}}_{x \psi_a} \mathbf{w}_e = \nabla E_a + \mathbf{f}_g - \mathbf{J}^{\mathrm{T}}_{q_a \psi_a} \underbrace{\left(\boldsymbol{\tau}_{nl} + \boldsymbol{\tau}_{load}\right)}_{\boldsymbol{\tau}_{measured}} \tag{5.7}$$

where $\tau_{measured}$ is the measured backbone force during an experiment.

In the following, we will assume that an estimate of the no load joint forces (termed $\hat{\tau}_{nl}$) is available through an estimation process as described in Section 5.3.2. During experiments, we have $\tau_{measured}$ and the estimated $\hat{\tau}_{nl}$. We therefore reformulate the statics equations to capture their dependence on the difference between the measured backbone forces and the estimated no-load backbone forces. To achieve this, we substitute $\nabla E_a + \mathbf{f}_g$ from (5.6) into (5.7) to obtain:

$$\mathbf{J}_{x\psi_a}^{\mathrm{T}} \mathbf{w}_e = \mathbf{J}_{q_a\psi_a}^{\mathrm{T}} \tau_{nl} - \mathbf{J}_{q_a\psi_a}^{\mathrm{T}} \tau_{measured} \tag{5.8}$$

Assuming that $\hat{\tau}_{nl}$ is a good approximation of τ_{nl}, we can write:

$$\mathbf{J}_{x\psi_a}^{\mathrm{T}} \mathbf{w}_e = -\mathbf{J}_{q_a\psi_a}^{\mathrm{T}} \tau_r \tag{5.9}$$

where τ_r is defined as the residual backbone measurement capturing the difference in backbone force with and without end effector load:

$$\tau_r \triangleq \tau_{measured} - \hat{\tau}_{nl} \tag{5.10}$$

To implement the single-segment force sensing approach used in this work, a selection matrix $\mathbf{\Lambda}_j$ is defined for the j^{th} segment as:

$$\mathbf{\Lambda}_j \triangleq \begin{bmatrix} \mathbf{I}\delta_{1j}, \mathbf{I}\delta_{2j}, \ldots, \mathbf{I}\delta_{n_s j} \end{bmatrix}^{\mathrm{T}} \tag{5.11}$$

where δ_{ij} is the Kronecker delta function, n_s is the number of segments in the continuum robot ($n_s = 2$ for the IREP) and $\mathbf{I}$ is a 2×2 identity matrix.

Using this definition, we express the single-segment force sensing equation for the j^{th}

segment as:

$$(\mathbf{J}_{x\psi_a}\mathbf{\Lambda}_j)^{\mathrm{T}}\mathbf{w}_e = -(\mathbf{J}_{q_a\psi_a}\mathbf{\Lambda}_j)^{\mathrm{T}}\boldsymbol{\tau}_r \tag{5.12}$$

This equation can be solved for $\mathbf{w}_e$ through a pseudo inverse and the least-norm solution was used estimate the applied wrench. While methods for null-space projection can be used to incorporate *a-priori* information as in [52], we used a simple pseudo-inverse solution for simplicity.

This approach assumes knowledge of $\boldsymbol{\tau}_{measured}$ and $\hat{\boldsymbol{\tau}}_{nl}$. $\boldsymbol{\tau}_{measured}$ is the measured force on the backbones during forceful interaction with the environment. The vector $\hat{\boldsymbol{\tau}}_{nl}$ is estimated from experimental data with $\mathbf{w}_e = \mathbf{0}$ through a support vector regression as described below. This model also assumes that the presence of loading does not change the frictional characteristics or the amount of energy stored in the bent snake, which should hold for small deflections.

5.3.2 Support Vector Regression Compensation:

In order to perform force sensing using (5.9), $\boldsymbol{\tau}_{nl}$ must be estimated at any given robot configuration (since its estimate $\hat{\boldsymbol{\tau}}_{nl}$ is used in (5.10)).

Modeling frictional uncertainties has a number of difficulties because it is a strongly nonlinear function that depends not only on the current pose of the robot but also the history of the motion of the snake. For the IREP in particular, the long actuation line, high backbone forces, and parallelogram linkage add complexity and uncertainty to the backbone routing and frictional losses.

A number of works in the past have sought to find modeling methods to account for hysteretic behavior, with the Preisach model being a foundational work using a series of hysterons to represent directional behavior [194]. Similar to the Preisach model, the Prandtl-Ishlinskii model has been proposed which researchers have generalized to account for asymmetry and non-monotonic hysteresis [196]. Others have generalized the Preisach model to account for multi-dimensional hysteresis [197] or applied simplified models for

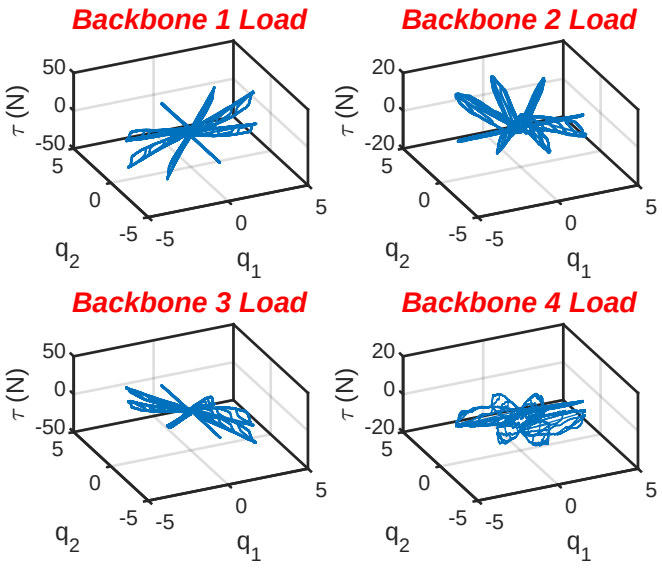

Figure 5.2: Backbone load measurements during free-space movement for the first segment of the IREP. Hysteresis loops can be seen for all the backbones.

vector hysteresis [198]. However, the modeling problem in the JEFS scenario is somewhat unique in that the load is a function of joint velocities and the coupled, hysteretic, two-dimensional joint space configuration. The presence of multidimensional, coupled, hysteretic inputs leaves standard hysteresis modeling techniques insufficient.

Because of these difficulties, a data-based method for compensation is used by collecting free-space information as in [181]. In order to estimate $\boldsymbol{\tau}_{nl}$, measurements of $\boldsymbol{\tau}_{loadcell}$ are taken as the robot moves across the workspace when $\mathbf{w}_e = 0$. This is done through repeated experiments bending and straightening the snake at different values of δ as well as slowly bending and straightening the snake in a spiral. This produces a dense dataset across the workspace of configurations and backbone tensions – a subset of which is shown in Fig. 5.2.

Once a dense dataset is collected, a regression method can be used to estimate $\boldsymbol{\tau}_{nl}$ at any given point in the workspace as a function of the current snake configuration. Because of its ability to quickly compute the regression result of a complicated manifold at a given point in the workspace, support-vector-regression (SVR) was chosen for this particular problem.

SVR allows for a transformation of the training variable into a higher-dimensional space by using some kernel function of the training data, which allows for better fitting on nonlinear data. In this work, a Gaussian kernel is used with standardized kernel parameters through MATLAB's Statistics and Machine Learning Toolbox. The output of the SVR is formulated as a set of support vectors and weights, so the calculation of the regression output at a given point is a linear computation that can be applied for real-time compensation. The estimated backbone force $\hat{\tau}_{nl}$ can be calculated as a function of the feature vector ϕ:

$$\hat{\tau}_{nl_i}(\phi) = \sum_{n=1}^{N} \alpha_n k(\phi_n, \phi) + b_i \quad i \in [1,8] \tag{5.13}$$

Where α_n is the weight to each support vector, ϕ_n, and b_i is a bias term for the i^{th} backbone force. We note that $i \in [1,8]$ since we train over the entire set of backbone forces for the two segments of the IREP dexterous arm where each continuum segment has four backbones. $k(\phi_i, \phi)$ is the Gaussian/radial basis function kernel:

$$k(\phi_i, \phi) = e^{\frac{-1}{\eta^2}||\phi_i - \phi||^2} \tag{5.14}$$

where the scaling factor η was determined using automatic kernel scaling provided by the MATLAB Statistics and Machine Learning Toolbox.

In order to obtain an accurate regression, an intelligent feature vector must be chosen to fit the data. Because of the complex frictional states and hysteretical uncertainty in the losses inside the cone and the actuation lines, historical features are required. A feature vector, ϕ, is defined:

$$\phi \triangleq \left[\mathbf{q}^{\mathrm{T}}, \dot{\mathbf{q}}^{\mathrm{T}}, \mathbf{s}^{\mathrm{T}}\right]^{\mathrm{T}} \tag{5.15}$$

The joint space displacement and speed are represented by $\mathbf{q}$ and $\dot{\mathbf{q}}$, and $\mathbf{s}$ is a hysteron-inspired feature computed as the saturated integral of the joint space velocity, which roughly represents whether the snake is bending or straightening, with an interpolation between

those states. It is important to maintain this historical feature because the frictional state of the robot is path-dependent and may be different even at the same joint position and velocity depending on how the arm arrived to that state. To this end, the hysteresis feature $\mathbf{s}$ is defined at time-step $k+1$ in the digital system as a saturated sum:

$$\mathbf{s}_{k+1} \triangleq \begin{cases} \mathbf{s}_k + \xi \dot{\mathbf{q}} & \text{if} \quad |\mathbf{s}_k + \xi \dot{\mathbf{q}}| < 1 \\ 1 & \text{if} \quad \mathbf{s}_k + \xi \dot{\mathbf{q}} > 1 \\ -1 & \text{if} \quad \mathbf{s}_k + \xi \dot{\mathbf{q}} < -1 \end{cases} \tag{5.16}$$

Where ξ is a parameter determining speed of traversal from one state to the next. The training error was insensitive to changes in ξ, unless it was very small, so a constant $\xi = 4$ was chosen for the datasets below.

In contrast to prior work where configuration-space variables were used in the regression [181], joint-space variables are used for the regression feature vector because they do not have discontinuities within the workspace and form a smoother mapping. The cylindrical workspace represented by the bending plane angle δ (shown in Fig. 4.1) is especially difficult to perform regression on because of the representational difficulties when representing δ measurements separated by 360° which represent the same physical configuration, but are representationally distant from one another. A transformation to joint space covers the same workspace with none of these representational discontinuities and thus produces better regression results.

For better numerical conditioning of the weight optimization problem, a normalization of the feature vectors is carried out before they are input into the SVR regression algorithm [199]. This feature normalization was carried out as:

$$\phi \triangleq 2\left(\frac{\phi_{\text{raw}} - \phi_{\text{min}}}{\phi_{\text{max}} - \phi_{\text{min}}}\right) - 1 \tag{5.17}$$

where ϕ_{raw} is the raw feature data without normalization, and ϕ_{min} and ϕ_{max} are obtained

Table 5.1: Regression results for different SVR estimation techniques based on backbone force measurements while moving the robot without any load at its tip. The middle column shows the average regression error. This error is in generalized force in the first two rows and in joint-level force in the last two rows. The right column shows the regression error when used for compensation in the estimate of end-effector forces.

	Regression Error	**Force Error**
ψ **- no hysteresis**	30.0 J/rad	0.60 N
ψ **- hysteresis**	13.1 J/rad	0.43 N
q - no hysteresis	4.0 N	0.17 N
q - hysteresis	1.7 N	0.06 N

from the training dataset, which represent the vectors of the minimum and maximum value of the training-set vector space. This scales each variable, if it matches the range of the training set, to lie between -1 and 1.

5.3.3 Free-Space Training Result:

After a regression method was chosen, an experiment was performed to collect the data required to estimate τ_{nl}. The IREP was commanded to bend in free space while measuring backbone forces and motion history.

A training dataset was generated by moving the continuum segment $\theta \in [45^\circ, 90^\circ], \delta \in [0^\circ, 360^\circ]$. The complete training dataset included over 32000 configuration samples collected while the continuum arm was moving. These motions were carried out by changing θ while holding δ fixed or in spiral experiments in configuration space wherein the robot was commanded to slowly increase and/or decrease θ and δ simultaneously. This data was collected while the robot was moving slowly with movements taking 9.3 minutes.

The SVR regression over joint-space data is shown in Fig. 5.3 for the case of SVR training using the feature vector defined in (5.15). It can be clearly seen that the SVR is able to capture not only the general shape of the backbone forces during movement, but also the interior hysteresis loops. This figure shows the result for a single backbone and simple experiment for ease of visualization, but separate regressions were performed for

each backbone over more complex motion profiles.

Table 5.1 presents the training error for different regression features and force sensing strategies. The middle column shows the training error in the space of the regression: generalized forces for the first two rows and backbone tension for the last two rows. The right column shows the error in the force estimation when the offset is applied and fed into the force sensing equation. The first row, "Configuration Space - No Hysteresis", shows the results for training an SVR in configuration space for the force sensing method in (5.3) using fitting in configuration space without any hysteresis parameter included in the feature vector except for the sign of the velocity of θ, in accordance with the approach of [181]. The second row, "Configuration Space - Hysteresis", adds a similarly-defined hysteresis feature as in (5.16) on each of the elements of the configurations space vector. The third row, "Joint Space - No Hysteresis" uses the method in (5.9), but only the features $\mathbf{q}$ and $sgn(\dot{\mathbf{q}})$ for regression. The final row, "Joint Space - Hysteresis" uses the same equation and the feature vector from (5.15). The combined use of hysteresis measurements and conversion from representation and regression in configuration space to joint space greatly reduces training error for this dataset, to 0.06 N for the proposed method, reduced from 0.16 N or even 0.62 N in the worst case.

5.3.4 Model Parameter Calibration

The single segment force sensing equation, (5.12), is a function of the residual backbone force τ_r, which is estimated based on backbone force measurements and a regression of no-load backbone forces (5.10). However, when loads are applied to the robot, wire transmission non-linearities may cause the force measured on the loadcell in the actuation unit to differ from the force on the backbones at the distal end of the robot in the continuum segment. To model this nonlinearity, we introduce the correction:

$$\tau_{ri} \rightarrow \tau_{ri}\beta_i \tag{5.18}$$

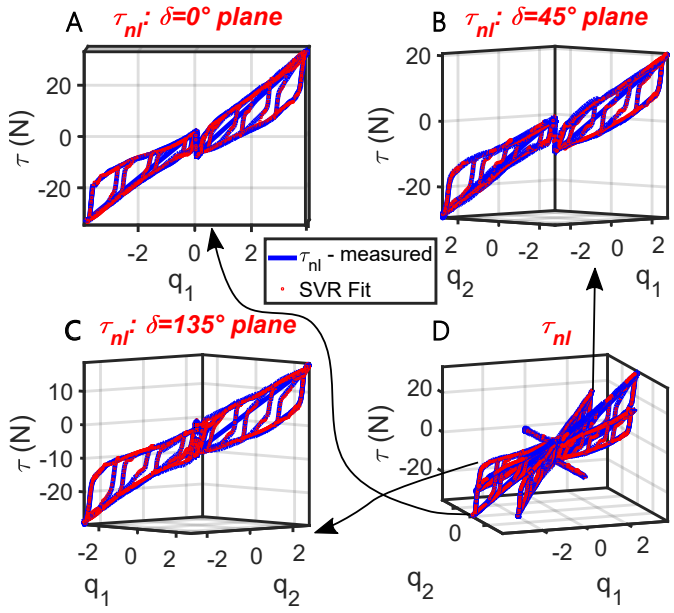

Figure 5.3: Estimation of backbone force for a particular backbone using support vector regression and hysteresis parameters in joint space. The blue traces show the raw data captured during unloaded robot motion, with red dots marking the regression results. Subfigures A-C show sliced planes of the dataset shown in D.

where $i = 1, \ldots, 8$. β_i is a transmission calibration factor that is formulated as dependent on the backbone force.

In the following derivation, we will assume that for each backbone, β_i is expressed as a linear combination of norm-bounded modal functions:

$$\beta_i = \mathbf{b}_i(\widetilde{\tau}_{ri})^{\mathrm{T}}\boldsymbol{\gamma}_i, \quad i = 1, \ldots, 8 \tag{5.19}$$

where $\widetilde{\tau}_{ri} \in [0, 1]$ is the normalized backbone force residual as in (5.20) and $\mathbf{b}_i$ and $\boldsymbol{\gamma}_i$ are the vectors of modal basis functions and modal coefficients for the i^{th} backbone. $\boldsymbol{\gamma}_i$ is sought

as the result of a model calibration process based on experimental data.

$$\widetilde{\tau}_{ri} = \begin{cases} 0 & \tau_{ri} <= \tau_{min} \\ \frac{\tau_{ri}-\tau_{min}}{\tau_{max}-\tau_{min}} & \tau_{min} < \tau_{ri} < \tau_{max} \\ 1 & \tau_{ri} >= \tau_{max} \end{cases} \tag{5.20}$$

The modal basis functions are formulated using Bernstein basis polynomials where the j^{th} element of $\mathbf{b}_i$ is defined as:

$$b_{i,j}(\widetilde{\tau}_{ri}) = \frac{n_b!\,\widetilde{\tau}_{ri}^{j}(1-\widetilde{\tau}_{ri})^{n_b-1}}{j!(n_b!-j!)} \quad j = 0 \ldots n_b \tag{5.21}$$

where $(\cdot)!$ is the factorial operator and the order of the Bernstein polynomial, n_b, was chosen as 4.

We define the full calibration vector $\boldsymbol{\beta}$ as:

$$\boldsymbol{\beta} \triangleq \begin{bmatrix} \beta_1, & \ldots, & \beta_8 \end{bmatrix}^{\mathrm{T}} \tag{5.22}$$

and the full-robot augmented modal coefficient vector $\boldsymbol{\gamma}_a$ is defined as

$$\boldsymbol{\gamma}_a \triangleq \left[\boldsymbol{\gamma}_1^{\mathrm{T}}, \ldots, \boldsymbol{\gamma}_8^{\mathrm{T}}\right]^{\mathrm{T}},\ \boldsymbol{\gamma}_i \in \mathbb{R}^{(n_b+1)\times 1}, i = 1 \ldots 8 \tag{5.23}$$

Using these definitions, $\boldsymbol{\beta}$ may be expressed as:

$$\boldsymbol{\beta} = \mathbf{B}\boldsymbol{\gamma}_a \tag{5.24}$$

Where $\mathbf{B}$ is formulated as a block diagonal matrix:

$$\mathbf{B} = \begin{bmatrix} \mathbf{b}_1(\widetilde{\tau}_{r1})^{\mathrm{T}} & \dots & \mathbf{0} \\ \vdots & \ddots & \vdots \\ \mathbf{0} & \dots & \mathbf{b}_8(\widetilde{\tau}_{r8})^{\mathrm{T}} \end{bmatrix} \in \mathbb{R}^{8\times(8n_b+8)} \tag{5.25}$$

The values $\tau_{max} = 15N$ and $\tau_{min} = -15N$ were used in (5.20). These bounds were conservatively chosen to bound experimentally observed data.

Using this formulation, the single segment force sensing equation for the j^{th} segment (5.12) becomes:

$$(\mathbf{J}_{x\psi_a}\mathbf{\Lambda}_j)^{\mathrm{T}}\mathbf{w}_e = -(\mathbf{J}_{q_a\psi_a}\mathbf{\Lambda}_j)^{\mathrm{T}} Diag(\boldsymbol{\tau}_r)\mathbf{B}\boldsymbol{\gamma}_a \tag{5.26}$$

where $Diag(\boldsymbol{\tau}_r)$ creates a diagonal matrix with $\boldsymbol{\tau}_r$ as its main diagonal.

A two-part process was used to solve for $\boldsymbol{\gamma}_a$, the vector of unknowns in (5.26). First, no-load experiments were conducted and a support vector regressor was constructed to be able to estimate $\hat{\boldsymbol{\tau}}_{nl}$. Then, during a second experiment where $\boldsymbol{w}_e \neq \mathbf{0}$, the SVR and experimental data were used to obtain $\widetilde{\boldsymbol{\tau}}_r$ and estimate nominal wrenches. Using measurements of the actual forces, measured with a force sensor, errors in this nominal estimate were minimized by updating $\boldsymbol{\gamma}_a$.

A linear least squares problem was solved to find $\boldsymbol{\gamma}_a$ using the 'trust-region-reflective' algorithm from MATLAB's Optimization Toolbox with upper and lower bounds of 2 and 0.2 for each element of $\boldsymbol{\gamma}_a$. Because Bernstein polynomials are non-negative and sum to 1, bounding the coefficients also bounds the polynomials they represent. By keeping these bounds positive and not much larger than one, this bounds the transmission correction parameter $\boldsymbol{\beta}$ so that it adjusts $\boldsymbol{\tau}_r$, but avoids non-physical modeling where directions of backbone forces are reversed or large gains that would override nominal model behavior.

The least squares problem to be solved for $\boldsymbol{\gamma}_a$ is formed from a set of equations as (5.26)

for m values of $\mathbf{w}_e$ and at varying robot configurations:

$$\min_{\gamma_a} \frac{1}{2}||\mathbf{C}\gamma_a - \mathbf{d}||_2^2, \quad 0.2 \leq \gamma_a \leq 2 \tag{5.27}$$

$$\mathbf{C} \triangleq \begin{bmatrix} \vdots \\ -(\mathbf{J}_{q_a \psi_a,k} \mathbf{\Lambda}_j)^{\mathrm{T}} Diag(\boldsymbol{\tau}_{r,k}) \mathbf{B}_k \\ \vdots \end{bmatrix} \quad k = 1..m \tag{5.28}$$

$$\mathbf{d} \triangleq \begin{bmatrix} \vdots \\ (\mathbf{J}_{x \psi_a,k} \mathbf{\Lambda}_j)^{\mathrm{T}} \mathbf{w}_{e,k} \\ \vdots \end{bmatrix} \quad k = 1..m \tag{5.29}$$

where k denotes the k^{th} data point for $\mathbf{w}_e$.

5.3.5 JEFS Feedback Hybrid Controller

For an additional set of experiments, the controller from section 4.3 is updated to incorporate JEFS feedback and use direct kinematics in the place of a mixed feedback framework. The control framework followed the architecture shown in Fig. 5.4.

While the insertion of the arm, b_0, and the parallelogram control, b_{1x} and b_{1z}, were included for these experiments, only single-segment motion was implemented because multi-segment motion affects backbone forces. Therefore, this adjusted controller only controlled the first (proximal) segment by commanding $\psi_1 = [\theta_1, \delta_1]^{\mathrm{T}}$ and holding the distal segment straight. To capture the entire configuration of this movement, the robot configuration variable from (4.13) is reformulated as:

$$\psi_{\boldsymbol{r}} \triangleq \begin{bmatrix} b_0 & b_{1x} & b_{1z} & \theta_1 & \delta_1 \end{bmatrix}^{\mathrm{T}} \tag{5.30}$$

In the experiments below, only position and force control were desired, so the robot

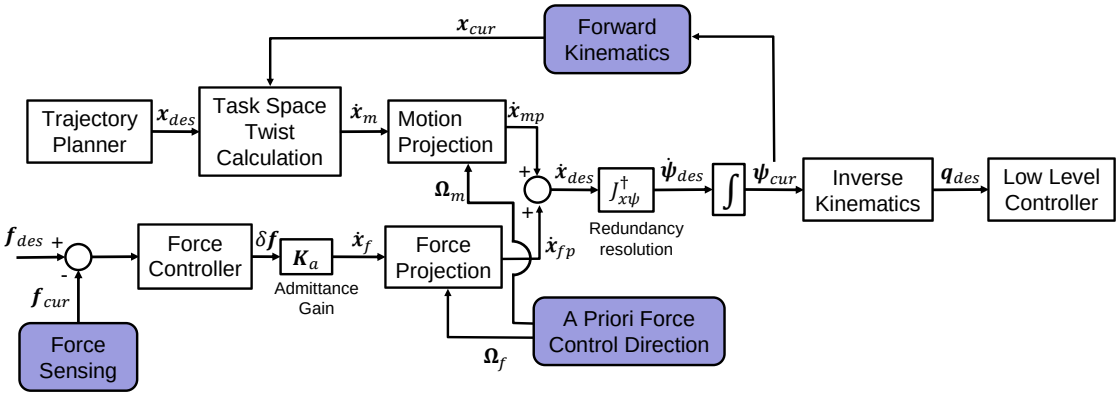

Figure 5.4: Block diagram for a hybrid admittance/position controller using JEFS feedback and a priori environment information to regulate environment interaction forces.

was commanded only in Cartesian space with a velocity $\dot{\mathbf{p}} \in \mathbb{R}^{3\times 1}$. With these changes, a truncated $\mathbf{J}_{x\psi_r}$ is used to find $\dot{\mathbf{p}}$ following (4.14) and the same hybrid controller as (4.21) and admittance law from (4.19).

5.4 Automated Experiments

The above force sensing and control framework was used for automated experiments in regulating environment interaction forces. Before experiments were carried out, the robot was commanded to bend to a "warmup" pose and then return to the straight home position. This gave consistency to the internal friction states of the arm when starting any given experiment. Experiments were performed across the robot workspace using a rotary stage, in mock organ palpation, knot-tightening, and a simulated ablation task; the experimental setup for this task is shown in Figs. 5.5, 5.8. The force estimation and regulation errors for these experiments is displayed in Table 5.2.

For each experiment type, the model parameter correction method from Section 5.3.4 was applied, however care had to be taken when fitting γ_a - the training experiment had to be similar in the area of the workspace and nature of applied forces as the test experiment. For the rotary stage, palpation, and ablation experiments, model-parameter training was performed using data from interaction with the rotary stage combined with data from a

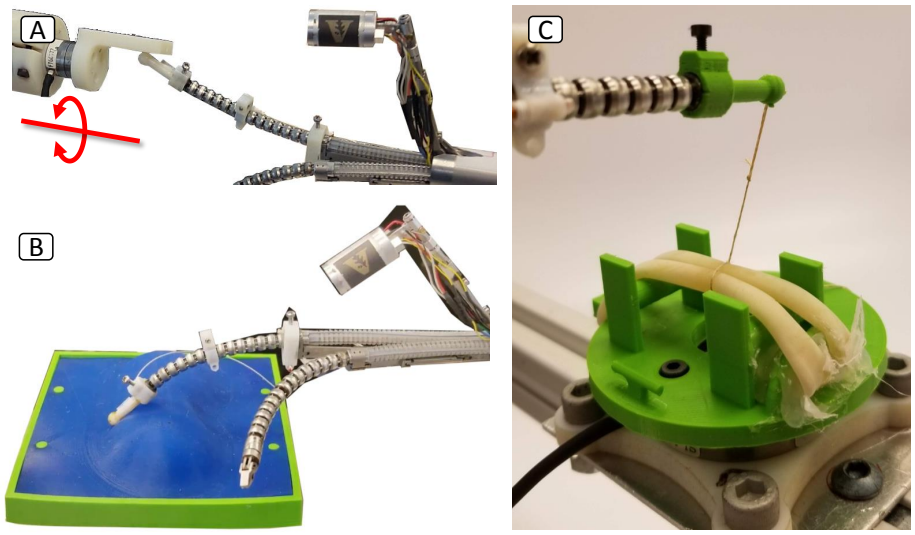

Figure 5.5: Setup of automated environment interaction experiments A) Flat environment interaction across robot workspace B) Organ palpation under autonomous control C) Knot-tightening experiment

preliminary palpation experiment. This training experiment contained over 12000 datapoints collected over 20 minutes of forceful interaction with a mean force of 0.4 N and a maximum force applied of 2.2 N. Originally, only data from the rotary stage had been used as the training data for the model parameters, but that experiment, $\delta = (0°, 45°, ...360°)$, contained insufficiently rich loading data to reduce estimation errors in other experiments.

A separate model parameter was used for the knot-tightening experiments which were trained in a similar knot-tightening task on the same experimental setup with over 6000 datapoints and a mean force of 0.7 N and a maximum force of 1.6 N over a total training experimental length of 9.7 minutes.

No set of model correction parameters were found that could reduce errors for all the tasks, even if fit to data from a combination of all types of experiments. In all scenarios, experiments were feasible using only SVR compensation and no model parameters, but at the expense of increased force estimation errors and more inaccurate force regulation.

The middle-right column of Table 5.2 has elements in parenthesis showing the force estimation errors using SVR estimation only, not with the use of model parameters. While

	Mean Force	Estimate Error	Regulation Error
Rotary Stage	(0.75)	0.32* (0.43)	(0.33)
Organ Palpation	0.82	0.21 (0.24)	0.31
Knot-Tightening	0.62	0.21 (0.26)	0.17
Mock Ablation	0.86	0.21 (0.38)	0.14

Table 5.2: Average applied forces, force estimation errors, and force regulation errors for automated experiments. All measurements reported in Newtons. () denote experimental results using SVR without model parameter correction, * denotes that estimation included measurements of training set data for model parameters.

these errors were larger, using JEFS feedback with this level of sensing error may still be useful for certain surgical applications (e.g. tightening sutures with multi-Newton levels of required maximum tension, as has been shown as standard practice [185]).

5.4.1 Rotary Stage

In the rotary stage experiment, the IREP was commanded to push against a flat environment at eight angles spaced consistently around the IREP in the experiment setup shown in 5.5A. Forces were measured with an ATI (Apex, North Carolina) Nano17 force/torque sensor which was rotated around the robot. At each rotation direction, the IREP was commanded to move toward the flat surface in position control until contact was detected by JEFS. After contact was made, the hybrid admittance controller was used to regulate to a desired force of 0.75 N in the direction of the environment.

As this experiment was meant to be a source for model parameters for other experiments (although this was later proved to be insufficient), the experiment was not repeated both with and without model parameter assistance. For this reason, the mean force and regulation error for this experiment were both found only with SVR assistance. During contact with the surface, the mean force regulation error in the force-control direction of

the hybrid controller was 0.33 N. The average interaction force in the force-controlled plane was 0.75 N. When training model parameters on this data, the use of model parameters reduced mean force estimation errors in the plane where forces were controlled from 0.43 N to 0.32 N across the entire experiment.

5.4.2 Organ Palpation

The IREP was commanded to palpate an Ecoflex^{TM} silicone rubber (Smooth-On, Macungie, Pennsylvania) phantom kidney mounted on an ATI Nano 43 force sensor as shown in Fig. 5.5B. The robot was commanded to scan the organ with a series of line scans pulling from the "far" end of the organ towards the robot base. For each scan line, a 0.75 N vertical force along the y axis of the robot's base frame was commanded throughout the experiment. The robot was not used to palpate while moving away from the base of the robot, because when moving towards the organ there is a risk of the robot jabbing into the organ, causing an increase in interaction forces. Keeping the motion direction toward the robot base during contact prevented this. A video of this palpation can be seen in Multimedia Extension 3, linked from Appendix A.4.

An NDI (Ontario, Canada) trakSTAR 2 magnetic tracking system was used to measure the robot movement, which has a measured RMS sensor noise in position measurements of 1.4 mm. These measurements were used to obtain the shape of the scanned section of the organ. The point cloud of scanned points found as "in contact" with the organ according to JEFS was registered using the rigid form of the coherent point drift algorithm [175] to an STL of the silicone organ, generated from the mold the organ was created from. The result of this registration is shown in Fig. 5.6. The RMS error between the scanned points and the registered organ was 2.2 mm.

The palpation experiment had an RMS force-regulation error of 0.31 N compared to the desired interaction force of 0.75 N in the vertical direction. In force estimation, JEFS was able to achieve an RMS estimation error of 0.21 N of error in that same direction.

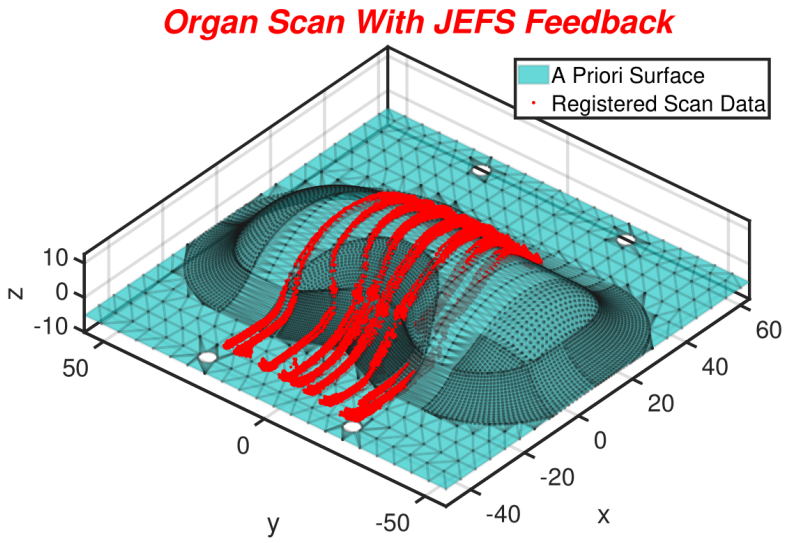

Figure 5.6: Organ geometry estimate from palpation under JEFS feedback with RMS shape error of 2.2 mm

5.4.3 Knot-Tightening

The IREP was commanded to pull on a string to tighten a simple overhand knot tied around a set of rubber tubes, similar to the setup of surgical training simulators used by medical trainees. The robot was commanded in admittance control to 9 directions in the robot's XY plane - the plane normal to the major axis of the robot arm when straight. An example experiment setup is shown in Fig. 5.5C.

Model parameters from similar knot-tightening experiments in the same area of the workspace were used to reduce estimation errors. SVR estimation errors in the force interaction plane of 0.26 N were reduced to 0.21 N using the model parameters. Using the model parameters for estimation during an experiment reduced steady-state admittance errors of the force control to 0.17 N, down from 0.22 N when using only SVR compensation. The measured and estimated interaction forces from one experiment when using model parameters for online JEFS are shown in Fig 5.7. These errors are within the range of acceptable forces for suture-tightening for surgical applications – for example, [72] found, for thick sutures, a mean tension of 2.4 N with a standard deviation of 0.58 N in hand-tied

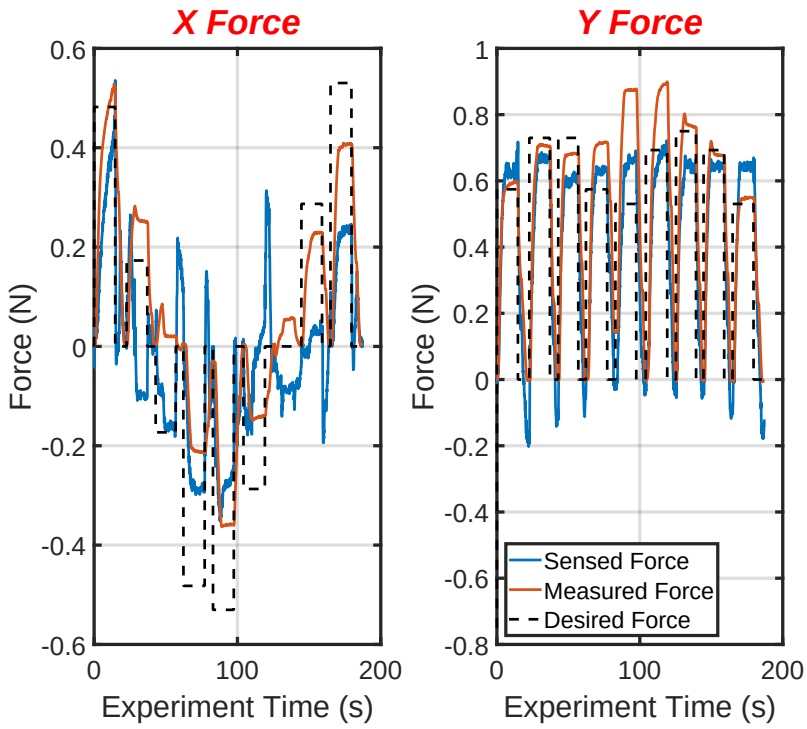

Figure 5.7: Force regulation and sensing results for automated admittance control for knot-tightening. 'Sensed' forces in blue are from the ATI force sensor, and the 'Measured' forces in orange are estimated using JEFS.

knots by surgeons.

5.4.4 Mock Ablation

On a silicone phantom with a rubber tube embedded visibly below the surface, the robot was commanded to follow the path of the tube at a constant vertical interaction force of 0.75 N. The experiment setup is shown in Figs. 5.8A, 5.9. This simulates an ablation or blunt dissection task as might be accomplished in a cholescystectomy procedure. Similar to the palpation task, the robot was commanded to follow the path from the "far" end of the tube to the "close" end. This was performed 20 times consecutively.

The mean estimation error in the direction of the force controller was 0.21 N and the mean applied vertical force of the trials was 0.86 N. The force regulation error for a single trial was calculated as the mean absolute difference between the interaction force in

the force-controlled vertical direction and the reference force, 0.75 N. The average force regulation error across all the trials was 0.14 N.

5.5 Telemanipulated User Study

A user study of 8 individuals was designed to test the use of JEFS as a feedback modality during the completion of surgically relevant tasks. Non-expert users were recruited from the Vanderbilt University student population in an IRB-approved study and were asked to telemanipulate the right arm of the IREP using a Force Dimension (Nyon, Switzerland) Omega.7 haptic device while also receiving stereo vision feedback through the surgeon console from the da Vinci Research Kit [200]. An EX8029 stereo camera from eYs3D (Taipei, Taiwan) with a 3cm baseline was used to capture the images used in the console view. The stereo viewer attached to the IREP has a small field of view, so this replacement camera was chosen for simplicity of control for the users to be able to easily see the full task workspace without requiring any motion of the camera. The experimental setup can be seen in Fig. 5.8 and a video of the user study process can be seen in Multimedia Extension 2, linked from Appendix A.4.

Two tasks were chosen for this protocol: knot-tightening and simulated ablation along a path. These used the same experimental setups as the automated experiments in sections 5.4.3 and 5.4.4. In each task, the users had to complete the task in three modes: a mode with no haptic feedback, a mode with JEFS feedback, and a mode with feedback from the Nano 43 force sensor (termed "sensor" feedback). Force feedback was given kinesthetically through the Omega.7 in the vertical direction and visually using an overlaid color-bar as in Fig. 5.9. The color bar showed the level of forces turning from red to green as the target force reached the center of the bar where there was a horizontal white line indicating the level of desired force. The feedback method was identical in both modes using feedback, with the only difference being the source of the forces sent to the Omega.7 and visual overlay (either from JEFS or the sensor). As no set of model parameters were found that

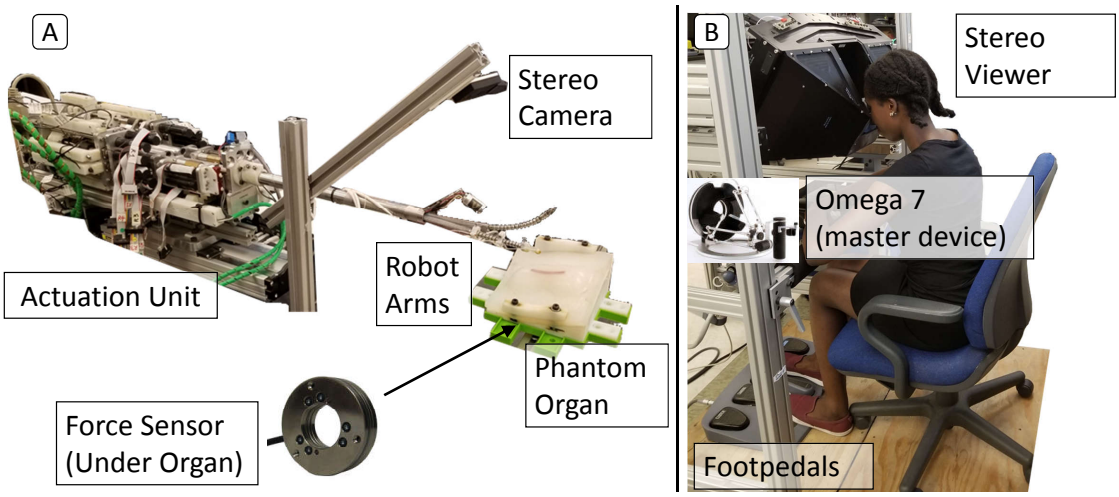

Figure 5.8: User study experimental setup. A) IREP arm for interacting with phantom anatomy mounted on a Nano 43 force sensor with stereo imaging of the environment for user feedback. B) Omega.7 master device mounted on a stereo viewer with footpedals for user control and visual feedback.

could reduce errors in both tasks, no model parameters were used during the execution of these experiments. This kept the sensing and control conditions consistent throughout all the tasks in the study.

Each user was given an opportunity to telemanipulate the robot for approximately 5 minutes as a warm-up period to understand how to control the robot's motion and feel example haptic feedback. After the warm-up period, each user performed the ablation experiments and then the knot-tightening experiments. The order of modes in each experiment was randomized for each user.

5.5.1 Mock Ablation

Users were instructed to follow the same path from section 5.4.4 as seen in Fig. 5.9 with a constant vertical interaction force of 0.75 N while moving towards the base of the robot. Each user completed 5 trials in each experimental condition, with a single trial consisting of following the path from its far end to its near end. After each trial, the user pressed a footpedal to indicate they had completed that trial, and the robot autonomously moved

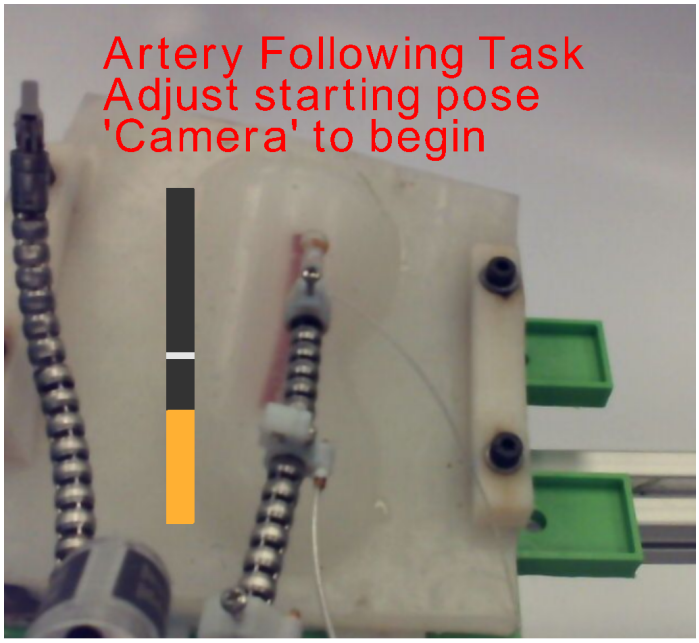

Figure 5.9: View in user study from a single eye of the stereo viewer of the mock ablation environment.

to the starting position of the curve for the next trial to begin when the user was ready to proceed.

Immediately preceding the trials with no force feedback, users performed a training task to learn how to apply the desired interaction force. No visual or kinesthetic force feedback was given to the user who was instructed to start the mock ablation task. At any time, the user could push a footpedal to show the current force level on screen. The user was instructed to repeatedly attempt the task, intermittently pressing the pedal to see the forces, until the task could be completed to the user's satisfaction while maintaining the desired force without needing the footpedal for guidance. The no-feedback mode experiment was then started.

5.5.2 Knot-Tightening

Using the same setup as the automated knot-tightening task in section 5.4.3, users were asked to tighten an overhand knot. Unlike the automated task which pulled in different di-

rections, to accommodate the relative inexperience of naive users, each user was instructed to pull vertically on the string until reaching 0.75 N for 10 trials. In the JEFS and sensor feedback modes, the forces were shown visually using the color bar and the users felt direct haptic feedback on their hands of the currently estimated vertical force.

In the mode without force feedback, users were trained in completing the task before attempting the 10 trials without assistance. Users were first asked to pull on the knot and were shown the force bar to understand how motions affected the forces. The bar was subsequently removed and the users were tested at attempting to find the desired force without the force bar visible. In between the training trials, the force bar would appear and the users would be notified if the force of their last attempt was too large, too small, or correct. Users were considered fully trained and instructed to exit the training mode and start the no-feedback experiment when able to achieve forces at the correct force level in 3 out of 5 consecutive trials.

5.5.3 User Study Results

The force-regulation results of the user study are shown in Fig 5.10, along with comparable automated results from section 5.4.4. For a direct comparison of similar results, an additional unidirectional knot-tightening trial was run, pulling vertically on a knot for 40 trials.

On the left of Fig. 5.10, boxplots of the interaction forces for the mock ablation task are plotted for each of the 3 user-interaction modes. A single data point represents the mean interaction force of a user during a single trial of the experiment. For 8 users and 5 trials per user, $N = 40$ for these plots. Results from the automated ablation experiment using JEFS with model parameters from section 5.4.4 are shown in the 4th boxplot where $N = 20$.

There were mean absolute errors between the recorded force levels and the desired force level of 0.75 N of 0.35 N, 0.31 N, 0.27 N, and 0.14 N during the unaided, JEFS feedback, sensor feedback, and automated experiments, respectively. The mean absolute error for a

single trial was calculated as the mean absolute error between the applied force and the desired force. This "per-trial" metric was averaged to find the mean absolute error for each experiment mode.

The force regulation errors were compared using Tukey's honest significant difference (HSD) criterion using MATLAB's Statistics and Machine Learning Toolbox. The HSD test showed a significant reduction in force regulation error in the automated experiment compared to all the other experiments ($p < 0.0001$), and a significant reduction in error in the sensor feedback mode when compared to the unaided mode($p = 0.005$). There were no other significant differences in the mean absolute errors of the other modes.

The variance of the mean applied force in the unaided mode, 0.05 N, was larger than that of the JEFS mode 0.03 N or the sensor-feedback mode 0.013 N. Using a 2-sample Brown-Forsythe test, both the unaided and JEFS feedback modes were shown to have larger variances than the sensor feedback mode ($p = 0.003$, $p = 0.034$), but there was not a statistically significant difference between the unaided and JEFS feedback modes ($p = 0.12$). The automated experiment had a smaller variance of mean applied force (0.0004 N) than all the other groups ($p < .00001$) using the same test.

The knot-tightening forces are shown on the right side of Fig. 5.10. Each data point represents the force selected by the user in a single trial. With 10 trials per mode per user and 8 users, each box plot has $N = 80$ datapoints within it. The far right boxplot shows the results from an automated experiment run in the same configuration as the user study knot-tightening experiment for $N = 40$ trials, using model parameter assistance to reduce errors.

The sensor feedback experiments and the automated experiment both had mean pulling forces across their trials of 0.76 N. The next closest mean force was in the unaided mode at 0.87 N. The JEFS feedback force mode showed a larger error with 1.07 N of mean applied force. Except for the sensor and automated experiments, the difference in means was statistically significant using HSD ($p < 0.007$).

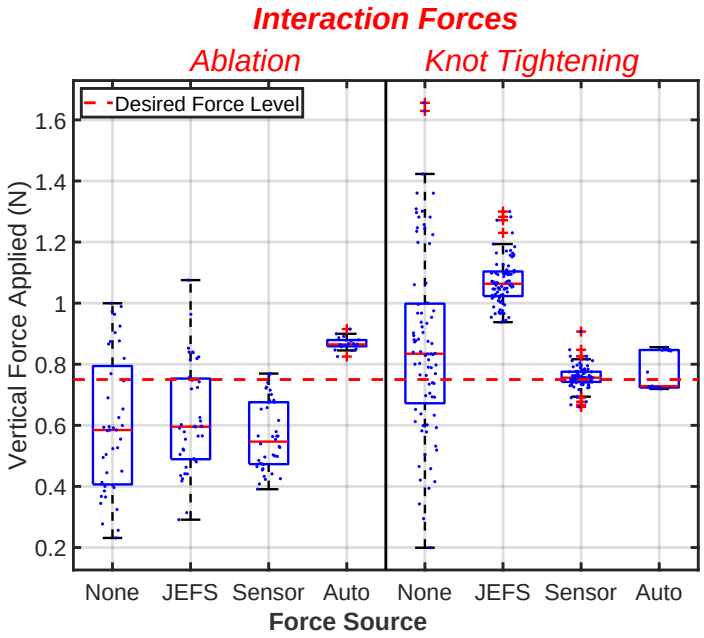

Figure 5.10: User interaction forces under different feedback modes. In simulated ablation, no force feedback allowed better force regulation except for the introduction of automated mock ablation under JEFS feedback. In knot-tightening, JEFS user feedback lowered variability but could not match the exact forces without model-parameter estimation.

The variance of the pulling forces were compared using two-sample Brown-Forsythe tests. The unaided mode variance, 0.091 N, was statistically larger than that of the JEFS feedback mode, 0.0059 N, the sensor feedback mode, 0.0014 N, and the automated mode, 0.0026 N ($p < 1e-6$). The sensor feedback mode exhibited a smaller variance than the JEFS mode ($p < 1e-6$), but not the automated mode ($p = 0.2$).

Users were given a set of questions on the effort required to complete each task during the study using a NASA/TLX score [201]. This evaluated the mental and physical effort required by the task; higher scores indicated a more demanding task requiring a large amount of focus and difficulty. These scores were compared using HSD. For the ablation tasks, there were no significant difference in the levels of user effort with mean effort levels of 12.9, 10.6, 8.5 for the unaided, JEFS feedback, and sensor feedback modes. For the knot-tightening experiments, a significant difference was found between the unaided mode with a score of 13.3 compared to both the JEFS and sensor feedback modes with scores of

5.3 and 1.9 which did not show a significantly different level of effort from one another.

When users were asked, there was no strong trend in which mode was preferred - as many preferred JEFS feedback as compared to ATI sensor feedback in the ablation task, and some users reported no difference between any of the modes including the unaided mode. Users were similarly split in the knot-tightening task, with 2 users indicating they had no preference between the JEFS and sensor feedback modes, 2 preferring JEFS feedback, and 4 preferring sensor feedback.

5.6 Discussion

5.6.1 Summary of Results

The use of JEFS can assist users in task completion, and when used with a priori knowledge of the sort of task desired to accomplish, can perform similarly to sensor-based feedback for accurate force regulation tasks.

In automated tasks, regulation errors ranged from 0.14 N to 0.33 N with estimation errors from 0.2 N to 0.3 N. It is important to note that, in some experiments, steady state errors in force control counteracted regulation errors, resulting in regulation errors smaller than the estimation errors. Positive estimation errors and negative steady-state regulation errors led to more accurate regulation. In different loading conditions where these errors compounded on each other, regulation errors could be larger.

In a user study comparing the use of JEFS feedback to force sensor feedback, JEFS feedback was useful, but not completely comparable to sensor feedback. In a mock ablation experiment, there was not a significant difference in the regulation error between sensor feedback and JEFS feedback, but sensor feedback reduced error when compared to no feedback at all whereas JEFS feedback did not show this improvement. JEFS feedback also showed more variability in the forces applied than sensor feedback.

Similar results were obtained in knot-tightening experiments. JEFS feedback without model-parameter correction reduced the variability of force regulation results when com-

pared to user performance with no force feedback, but it introduced a bias to the results. Average force errors were larger with JEFS feedback than when users were given no force feedback and relied only on visual cues.

While JEFS feedback had some setbacks to consistently improve task execution, the combination of JEFS feedback with task automation was able to perform similarly to sensor-based feedback and improve certain metrics. In mock ablation, both the mean force regulation error and the variance in forces applied were reduced when using automated task completion with JEFS feedback over sensor feedback in the user study. In knot-tightening, the automated experiment was statistically indistinguishable from sensor feedback in both the mean error and variance of applied forces over multiple trials.

It is notable that users in the mock ablation task were not able to consistently maintain forces very close to the desired force of 0.75 N regardless of the feedback method. This is most likely due to a slight angling of the organ so that users started to leave the surface as they followed the path and the difficulty of controlling the flexible robot while in contact with a flexible surface. The use of automated following using JEFS decreased force-regulation errors and the force variance, even when compared to sensor feedback, showing the utility of task automation with even imperfect sensing methods.

5.6.2 Model Assumptions and Improvements

There are a number of assumptions in the presented JEFS framework that leave room for future research to generalizing the applicability of this method.

The presented JEFS framework was presented for single-segment motion; adjustments may be required to apply the approach to multi-segment force estimation. A number of obstacles exist: moment coupling between segments may affect wrench estimation; the frictional states of multi-segment robots may be coupled, increasing the complexity of internal frictional states; the estimation of $\hat{\tau}_{nl}$ requires data from no-load experiments spanning the robot workspace, which may be difficult to practically accomplish with robots

across a higher dimensional workspace.

The model parameter calibration approach using γ_a was unable to be fit to generalized robot interaction states and was fit to particular sub-tasks. Because of this restriction, in practice it would be necessary to have automated methods for detecting surgical tasks - this can be done manually or through Markov modeling to detect surgical task signatures and apply the particular set of parameters in realtime [202].

The experiments in this investigation were performed with the robot pushing on the environment, not the inverse. Since the robot was not build to be backdrivable, it is likely that forces applied to a static robot or outside the movement direction of the robot would be more difficult to detect.

In most tasks presented, the robot was either pulling mostly vertically on a string ($\delta \approx 90^\circ$) or palpating vertically in the opposite direction ($\delta \approx -90^\circ$). This takes advantage of the fact that sensing was found to be best in this area of the workspace - frictional states were less repeatable when bending in a direction not aligned with one of the "primary axes" of the robot along one of the 4 backbones located along the x and y axes of the base frame. Although the robot was not commanded exactly along the y axis in these experiments, experiments located in areas of the workspace between the backbone locations (e.g $\delta = 45^\circ$) would be more difficult.

5.7 Conclusion

This chapter has presented work on continuum robot palpation and intrinsic force sensing methods for robot-environment interaction. The use of continuum robots in surgical domains is an important component for next-generation surgical systems that can reach deeper into the anatomy, interact dextrously with the environment, and sense interaction forces.

We have herein presented work on JEFS for force regulation using a continuum robot with a hybrid admittance/position controller. This work further enables practical continuum

robot designs to safely interact with their environment as they are used more frequently for next-generation surgical systems that can reach deeper into the anatomy while regulating forces safely.

Updated methods for force sensing were presented to better deal with uncertainty. A new JEFS formulation in robot joint space was presented that improves force estimation for systems with substantial actuation line friction. A hysteresis feature was developed to better account for history-dependent frictional losses. These methods were used for force sensing experiments during robot-environment interaction along with model parameters that were shown to increase force regulation repeatability and reduce estimation errors in automated experiments.

In robotic palpation, the presented methods showed the feasibility of using continuum robots to leverage JEFS to scan unknown geometry elastic environments and estimate environment geometry with an average scan accuracy of approximately 2mm and a force regulation accuracy around 0.3 N. Force estimation errors in a variety of experiments were able to be achieved at a level of 0.2 N with force regulation errors ranging from 0.14 N to 0.33 N depending on the experimental context.

Future work should investigate methods for addressing coupling effects for multi-segment results and the applicability of these methods to similar robot architectures. Workspace-dependence can also be investigated in greater depth for better generalizability of these results to robots which need to be able to execute tasks of a variety of types with a single set of model parameters.

CHAPTER 6
USER ASSISTANCE IN FORCEFUL TELEMANIPULATION

6.1 Motivation and Prior Art

The introduction of robotics to MIS has offered surgeons increased precision and multi-instrument manipulation capabilities. These benefits were accompanied with the disruption of the natural sensory feedback available to surgeons during manual open surgery. Complex interactions that can occur seamlessly during manual open surgery (e.g. digital palpation, organ retraction, and force-controlled ablation) are difficult during RAMIS due to this sensory disruption.

To address this deficit, methods for giving surgeons greater sensory presence have included direct force feedback [203], sensory substitution [204, 72, 70, 68], and virtual/augmented reality [205, 89] in applications such as force regulation in knot-tying [203], blunt dissection, [64] or palpation and environment stiffness exploration [206, 83, 94, 205]. However, there are limited works that have explored shared control with an autonomous agent during RAMIS [207, 208].

Emerging surgical approaches such as single port access surgery and natural orifice endoscopic transluminal surgery are driving the need for complex high-degree-of-freedom robotic systems that operate under strict manipulation and perception constraints [1]. Such systems challenge existing approaches for haptic feedback due to manipulator-master asymmetry and because these robots are expected to enable complex interaction with the anatomy despite severe perception barriers. Given the amount of information needed to be interpreted, direct force feedback using a bilateral telemanipulation scheme cannot convey all the information required to the surgeon and more sophisticated approaches are needed. To address this need, collaborating researchers have put forth the concept of *Complementary*

Situational Awareness (*CSA*) which uses a High-Level Controller (HLC) to update a virtual environment model using *in-vivo* sensory cues and to control certain aspects of the physical interaction with the anatomy while allowing the surgeon to retain control of the key task [18, 1]. For example, using the CSA framework, a robot can use *in-vivo* palpation information to offer an update of the geometry of a virtual fixture (VF) in the presence of organ shift and deformation or perform guided stiffness exploration [177, 209, 210, 159].

The ability of the CSA framework to map stiffness across the surface of an organ when palpating can augment surgeons' perception and allow them to localize and delineate boundaries of subsurface disease/anatomy like tumors or arteries. Incorporating stiffness information alongside geometric information can also improve the registration of pre-operative imaging to the intraoperative scene in RAMIS [177].

Previous works to estimate intraoperative stiffness information have traditionally required either specialized instrumentation or offline processing after the tissue has been probed or scanned. Approaches have included mechanical imaging [81], tactile arrays [77, 78, 79, 80], robotic probing [53, 82, 83, 178] and tissue excitation for mechanical impedance estimation [85]. While there have been some initial results in e.g. visual tracking of applied forces during organ manipulation [23], there is a need for approaches that allow a user to understand organ stiffness without additional hardware or effort in performing palpation motion and interpreting visual or motion cues during robot-organ interaction.

To allow semi-autonomous behaviors and improve stability, the CSA framework uses model-mediated telemanipulation where control is mediated through a virtual environment model. In this framework, one challenge is that mismatched contact states can occur between the virtual model and the physical robot. Previous methods have updated the surface location for interaction in a single direction [211, 212] or the orientation of a constraint frame during cutting operations in satellite servicing tasks [213]. When using model-mediation and hybrid control, as in [214], updates to the virtual contact state have

to be performed carefully to avoid discontinuities in the forces applied to the user's hand.

As noted in Chapter 1, RAMIS with soft tissue interaction has a number of difficulties due to deficiencies in sensing interaction forces and feedback methods for regulating forceful interaction and assisting in task completion. This chapter reports evaluation of several assistive approaches in the context of model-mediated telemanipulation for force regulation and force-guided exploration. Evaluation was carried out in collaboration with researchers at Johns Hopkins and Carnegie Mellon Universities, with the concomitant collaboration in the development of methods/software and experimental setups. In regulation, we used semi-autonomous force control alongside VFs for force-controlled mock ablation along a path. In exploration, we used assistive palpation and stiffness mapping methods to enable the detection of mock tumors embedded in phantom anatomy. We hypothesized that assistive feedback and semi-autonomous control can limit cognitive load and improve user performance. We designed an evaluation study that compares our assistive framework to standard telemanipulation approaches.

Two particular surgical tasks were chosen to evaluate this framework. The first was ablation along a path, as might be found during electrocautery in epicardial ablation. The second was the identification of subsurface features through palpation as may occur in the resection of liver tumors or the identification of artery locations when operating on other soft organs. A user study was carried out to assess the utility of our assistive framework compared to unassisted or naive approaches for assistance.

This chapter focuses on the interaction of RAMIS systems with soft organs for a number of reasons. While high-resolution preoperative imaging can often identify important structures and generate a surgical plan, such organs will shift and deform from their preoperative state to the intraoperative state, and may even shift during surgery as resection takes place or as different organs are moved or pushed by the surgeon. Deformable registration must be undertaken which requires intraoperative geometric data to be taken and intelligent deformable registration problems to be solved. Additionally, force-controlled interaction

Table 6.1: Table of Terminology

Term	Description
RAMIS	Robot-Assisted Miminally Invasive Surgery
HLC	High-Level Controller
MTM	Master Tool Manipulator (master device)
PSM	Patient-Side Manipulator (slave device)
VF	Virtual Fixture
PVF	Path Virtual Fixture
FRMM	Force-Regulated Model-Mediated Telemanipulation
$\mathbf{p}, \widetilde{\mathbf{p}}$	Robot position, virtual "proxy" robot position
$\mathbf{c}, \mathbf{s}$	Closest point to the robot on a curve, on a surface
$\tilde{\mathbf{c}}, \widetilde{\mathbf{s}}$	Closest point to the proxy on a curve, on a surface

for robots in low-stiffness environments remains a challenge. However, there is also an opportunity for increased information about the anatomy to be gained when dealing with soft organs because organ palpation can be used to identify subsurface features which have different stiffness than surrounding tissue.

The remainder of this chapter is organized as follows: Section 6.2 describes the robot control architecture and implementation of the model-mediated telemanipulation structure, along with the stiffness estimation algorithms and visual feedback assistance modes for users. Section 6.3 presents the experimental setup for a user study of mock ablation and palpation, the details of which are described in Section 6.4. We then summarize the results of the user study in Section 6.5 and present a discussion and concluding remarks in sections 6.6 and 6.7. Table 6.1 lists the terminology used in this chapter.

6.2 System Control Architecture

We evaluated our methods on the da Vinci Research Kit (dVRK) [200, 215] utilizing the Johns Hopkins University "Surgical Assistant Workstation (SAW)" software environment [216]. The users controlled one dVRK Patient Side Manipulator (PSM) to interact with a phantom organ model of a kidney by grasping the right arm of the dVRK Master Tool Manipulator (MTM) with a stereo viewer to provide visual feedback.

The control architecture follows that presented in [3], with some modifications. The general framework is shown in Fig. 6.1. The HLC is responsible for the type of telemanipulation connection between the MTM and PSM and uses a number of sub-components: telemanipulation feedback modes; model updates to account for differences between the environment model and the real robot; a wrist-alignment VF; a path-guidance VF; and stiffness estimation using Gaussian processes. Telemanipulation motion scaling is applied in all modes with a $\frac{2}{5}$ positional scaling to increase positional accuracy and a one-to-one orientational scaling for intuitive control.

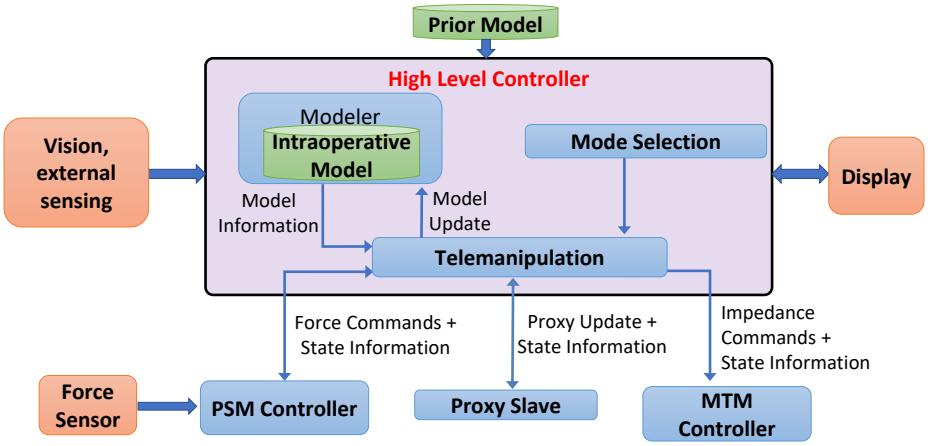

Figure 6.1: Control diagram of the CSA framework, figure adapted from [3].

6.2.1 High-Level Telemanipulation Feedback Modes

The HLC, whose general structure was developed by collaborators at Johns Hopkins University, was designed to allow three control/feedback modes for robot-environment interaction: unilateral telemanipulation, bilateral telemanipulation, and force-regulated model-mediated telemanipulation (FRMM).

In unilateral telemanipulation, the controller does not have any knowledge of the environment geometry or robot-environment interaction forces. This mode is similar to that of current commercial systems that have no force sensing or force feedback. Velocity commands from the MTM are directly sent to the PSM resulting in pure position control.

No forces are felt by the user at the MTM, which uses the gravity compensation method of [217], but no other active control. The only safety feature is in the low-level control of the PSM, which turns off the motors if a high current or tracking error are detected.

In bilateral telemanipulation, PSM-environment interaction forces are sent directly to the MTM using an impedance controller. To reduce oscillatory behavior due to time delays, the forces were scaled with a gain of 0.75 before being sent to the user on the MTM. Like unilateral telemanipulation, velocity commands of the MTM are sent directly to the PSM, which operates in position control.

In FRMM, a model-mediated framework allows independent PSM-organ interaction and MTM feedback. The user's hand movements control the position of a "proxy PSM", which interacts with a virtual model of the environment [3]. The interaction between the virtual environment and the proxy PSM generates the forces sent to the MTM using an *a-priori* environment model in the form of a triangular mesh with an assigned stiffness normal to the surface.

When the proxy PSM is above the model surface, the MTM controls the position of the proxy PSM, which directly updates the PSM position reference - mimicking unilateral telemanipulation. When in contact, a hybrid position-force controller regulates forces on the PSM, independent of the proxy. At any given location of the proxy PSM, the local surface normal $\hat{\mathbf{n}}$ is calculated from the model and used to calculate two projection matrices for the force and position controllers, $\mathbf{\Omega}_f$ and $\mathbf{\Omega}_p$, such that:

$$\mathbf{\Omega}_f = \hat{\mathbf{n}}\hat{\mathbf{n}}^{\mathrm{T}}, \quad \mathbf{\Omega}_p = \mathbf{I}_3 - \hat{\mathbf{n}}\hat{\mathbf{n}}^{\mathrm{T}} \tag{6.1}$$

where $\mathbf{I}_3 \in \mathbb{R}^{3\times 3}$ is the identity matrix. At each control time step, the desired PSM velocity, $\dot{\mathbf{p}}$, is calculated as:

$$\dot{\mathbf{p}} = \mathbf{\Omega}_p \dot{\tilde{\mathbf{p}}} + \mathbf{\Omega}_f \mathbf{K}_f (\mathbf{f}_{ref} - \mathbf{f}_{cur}) \tag{6.2}$$

and input into a resolved-rates algorithm to produce a joint position reference to a PD joint

position controller. The first term $\mathbf{\Omega}_p\dot{\tilde{\mathbf{p}}}$ takes into account the current velocity of the proxy PSM $\dot{\tilde{\mathbf{p}}}$ and produces a velocity command in the local tangent plane of the environment model. The second term $\mathbf{\Omega}_f\mathbf{K}_f(\mathbf{f}_{ref} - \mathbf{f}_{cur})$ uses an admittance gain $\mathbf{K}_f$ to produce a velocity command in the direction normal to the surface of the local environment model using the current and desired forces on the robot, $\mathbf{f}_{cur}$ and $\mathbf{f}_{ref}$.

The model-mediated framework allows assistive actions without disrupting the user. While the user retains control over the lateral motion of the MTM and feels intuitive feedback through interaction with the model environment, the PSM maintains independent force control. This enables high-performance force regulation while retaining intuitive user control.

6.2.2 Contact State Mismatch Between the Proxy and Real PSM

When using FRMM telemanipulation, the contact state of the real PSM with the environment and the contact state of the proxy PSM with the model environment may develop a mismatch. Real contact is detected when interaction forces exceed 0.1N, and proxy contact when the proxy intersects the environment mesh. Accounting for this mismatch was presented in [3], but has been slightly updated in this work for the particular implementation required for the desired tasks. A set of scenarios must be accounted for:

- When both the PSM and the proxy PSM are in contact, the hybrid position-force controller is engaged.
- If neither are in contact, the MTM motion controls the position of the proxy PSM in unilateral telemanipulation, directly updating the position reference for the PSM.
- If only the proxy is in contact, the hybrid position-force control is engaged to push the PSM onto the surface. This assumes that registration errors are small; model updates could be used to reduce errors if required [212].
- If only the PSM is in contact, the hybrid position-force control is engaged to prevent

the user from imparting unsafe forces to the surface without noticing (since no forces will be reflected on the MTM as long as the proxy PSM is not in contact with the environment model).

In order to allow the user to leave the surface, there must be a way to turn off the hybrid position-force controller as the user commands motions off of the organ. Therefore, when the PSM is in contact, but the proxy is more than 2mm away from the organ, the hybrid position-force controller is disengaged and unilateral telemanipulation is engaged as long as the PSM is moving away from the organ or until the proxy comes within the 2mm band again. This 2mm threshold was determined based on the experimentally characterized average fiducial localization error of approximately 1.0 mm when using the PSM as a digitizer [218, 219]. This maintains safe and intuitive control while still allowing users to leave and enter contact smoothly.

Algorithm 1 shows the control mode selection based on the contact states. $\widetilde{\mathbf{p}}$ denotes the proxy PSM position and $\widetilde{\mathbf{s}}$ the closest point on the environment model to the proxy PSM.

Algorithm 1 Contact State Control Modes

Mode Selection:

if (Proxy Contact) **then**
  Hybrid position-force control ▷ Full Contact or Proxy Contact
else (Proxy in Freespace)
  if (Slave Contact) **then**
    if ($||\widetilde{\mathbf{p}} - \widetilde{\mathbf{s}}|| > 2mm$ & $\dot{\widetilde{\mathbf{p}}} \cdot \hat{\mathbf{n}} > 0$) **then**
      Position control ▷ Leaving Slave Contact
    else
      Hybrid position-force control ▷ Slave Contact
    end if
  else
    Position control ▷ No Contact
  end if
end if

6.2.3 Position Discrepancy Between the Proxy and Real PSM

The proxy PSM is always in direct position control while the real PSM switches from a position control law to a hybrid position-force control law when contact is detected.

In the hybrid control mode, independent motions from the force controller can lead to positional discrepancies between the proxy and real PSM after prolonged interaction. If this discrepancy is not rectified, forces felt on the MTM (based on the current position of the proxy PSM) may be substantially different in magnitude and direction relative to those experienced by the PSM. These erroneous forces can confuse the user and cause undesirable motion. Therefore, the proxy PSM position must be updated to match that of the PSM.

If the HLC instantaneously updates the position of the proxy PSM to the current PSM position, the model-mediated nature of the controller is compromised. For example, if the interaction force between the proxy PSM and the model environment is larger than that of the PSM on the real environment, the position update will place the proxy PSM higher than it was before the update. The user, trying to regulate forces, will feel a decrease in the force feedback, and will push down again. However, the next update will again replace the proxy PSM higher, effectively resulting in users feeling like they can "fall through" the model environment. Therefore, a simple continuous update should be avoided.

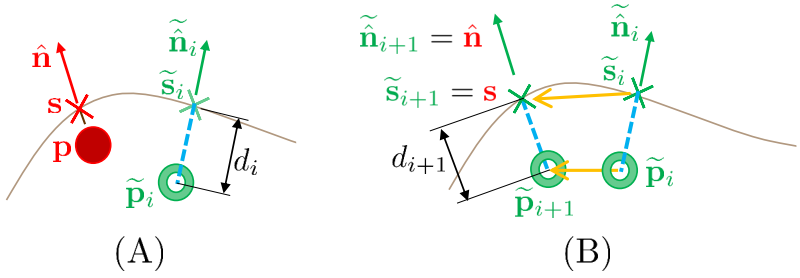

Figure 6.2: Achieving a haptically continuous proxy PSM update: (A) proxy and real PSM discrepancy before the update, (B) proxy PSM position update.

A more complete update strategy is shown in Fig. 6.2 which allows model interaction while also preserving *haptic continuity*, i.e., no jumps in the MTM interaction forces during nominal operation. In Fig. 6.2A, the current position of the PSM, its local surface normal and closest point to the model surface are represented as $\mathbf{p}$, $\hat{\mathbf{n}}$, and $\mathbf{s}$, respectively. The current position of the proxy PSM, $\widetilde{\mathbf{p}}_i$ corresponds to a closest point $\widetilde{\mathbf{s}}_i$ on the model surface,

with a penetration depth d_i along the local surface normal $\widetilde{\hat{\mathbf{n}}}_i$. In Fig. 6.2B, the updated proxy PSM position, $\widetilde{\mathbf{p}}_{i+1}$, is given by:

$$\widetilde{\mathbf{p}}_{i+1} = \mathbf{s} - d_{i+1}\hat{\mathbf{n}} \tag{6.3}$$

Assuming that location $\widetilde{\mathbf{s}}_i$ has an associated normal stiffness k_i then the magnitude of the force calculated by the model is $f_i = k_i d_i$. After the proxy update, the magnitude of this force should be constant, i.e. $f_{i+1} = f_i$. Therefore, assuming the normal stiffness at location $\mathbf{s}$ is k_{i+1}, then the penetration depth, d_{i+1}, should be:

$$d_{i+1} = \frac{d_i k_i}{k_{i+1}} \tag{6.4}$$

In this study, the environment had a constant stiffness, so $d_{i+1} = d_i$. This resolves the issue of keeping a constant force magnitude during the update. For the general case of a probe moving across a surface with minimum local curvature ρ at some maximum velocity v_{max}, the maximal angular disturbance $\delta\theta_{max}$ (change in direction between $\hat{\mathbf{n}}_i$ and $\hat{\mathbf{n}}_{i+1}$) caused by an update running with a period of δt will be:

$$\delta\theta_{max} \approx \frac{v_{max}\delta t}{\rho} \tag{6.5}$$

This shows that if the position discrepancy update is run slowly, or the user moves very quickly, or the surface has sudden changes in surface normal, the update will introduce some haptic discontinuity as the update changes the direction of forces on the MTM.

The update cycle time δt can be reduced to maintain fidelity of proxy and real PSM positions. However this cycle time should be significantly larger than the telemanipulation cycle time of the HLC to avoid having the repetitive updates conflict with intended motions of the user. In the experiments below using an environment model without surface discontinuities, an HLC telemanipulation loop frequency of 200Hz, and a position discrepancy

update frequency of 1Hz, the update was not noticeable to the users.

6.2.4 Wrist Alignment Virtual Fixture

Large pitch angles of the PSM wrist are not ideal for forceful interaction with the environment due to the resulting large moments. To resolve this problem and to help the users in tasks of ablation and palpation, we applied an orientational VF to the MTM. The desired orientation for the VF was derived from the environment local surface normal at the point closest to the PSM end effector. The user was free to rotate the tool about the local surface normal, but a nonlinear stiffness prevented the axis of the tool from deviating far from the local normal.

To calculate the torques applied on the MTM wrist by the orientational VF, we defined a frame {s} having its z axis aligned with the local environment surface normal at the point closest to the PSM tip and its x axis parallel to that of the PSM end effector frame {p}. Denoting the orientation of this frame as $\mathbf{R}_s$ and the orientation of the PSM wrist as $\mathbf{R}_p$, the torque applied to the MTM, τ_{vf}, was calculated as:

$$\tau_{vf} = \mathbf{K}_\theta \hat{\mathbf{m}} \theta_e^2 \tag{6.6}$$

$$\theta_e = \cos^{-1}\left(\frac{tr(\mathbf{R}_s^{\mathrm{T}}\mathbf{R}_p) - 1}{2}\right) \tag{6.7}$$

$$\hat{\mathbf{m}} = \frac{[(\mathbf{R}_s^{\mathrm{T}}\mathbf{R}_p) - (\mathbf{R}_s^{\mathrm{T}}\mathbf{R}_p)^{\mathrm{T}}]^\vee}{2\sin(\theta_e)} \tag{6.8}$$

$$\mathbf{K}_\theta = diag(k_\theta, k_\theta, 0) \tag{6.9}$$

where $\hat{\mathbf{m}}$ and θ_e are the axis-angle parametrization of the orientation error of {s} relative to {p}. The operators $[*]^\vee$, $tr(*)$, and $diag(*)$ extract the vector from a skew-symmetric matrix, compute the trace of a matrix, and make a diagonal matrix with the elements of $*$ on the main diagonal, respectively.

When the user is far from the surface, the closest point on the environment may jump

between different locations and introduce discontinuities in $\mathbf{R}_s$. To maintain haptic continuity, an interpolated frame {i} was used in place of {s} in the above equations. $\mathbf{R}_i$ was initialized equal to $\mathbf{R}_s$ and constantly moved toward $\mathbf{R}_s$ using an axis-angle interpolation. A rotational error matrix $d\mathbf{R}$ was calculated using the interpolated rotation at the previous timestep, $\mathbf{R}_{i-1}$

$$d\mathbf{R} = \mathbf{R}_{i-1}^{\mathrm{T}} \mathbf{R}_s \tag{6.10}$$

Using (6.7) and (6.8), $d\mathbf{R}$ was broken down into its axis-angle representation with axis $\hat{\boldsymbol{\omega}}$ and angle γ. These components were used to rotate the current orientation $\mathbf{R}_i$ toward $\mathbf{R}_s$ by k_i radians per time-step.

$$\mathbf{R}_i = \begin{cases} \mathbf{R}_s, & \text{if } \gamma < 0.01 \\ \mathbf{R}_{i-1} e^{k_i \hat{\boldsymbol{\omega}}} & \text{otherwise.} \end{cases} \tag{6.11}$$

This broadly aligned the VF with {s}, but prevented sudden changes in $\mathbf{R}_s$ from causing large changes in $\boldsymbol{\tau}_{vf}$.

6.2.5 Path-Guidance Virtual Fixture

A path virtual fixture (PVF) was used to guide the user's hand to follow some desired path on the surface of the environment. This was achieved through a soft barrier VF on the MTM that restricted movement transverse to the path. A diagram of the PVF is shown in Fig. 6.3.

At any given position of the proxy PSM tip, a local VF compliance frame $\{\widetilde{c}\}$ was calculated. The origin of this frame was chosen as the point closest to the proxy PSM tip and on the ablation path. The x axis of this frame was set to be the local tangent to the ablation path and the z axis was the outward-pointing local surface normal. The force of the PVF applied by the MTM in the PSM base frame {b} was set as:

$$\mathbf{f}_{vf} = \left({}^{\widetilde{c}}\mathbf{R}_b\right)^{-1} \mathbf{K}_p {}^{\widetilde{c}}\mathbf{R}_b (\widetilde{\mathbf{c}} - \widetilde{\mathbf{s}}) \tag{6.12}$$

where $\widetilde{\mathbf{c}}$ and $\widetilde{\mathbf{s}}$ are the origin of frame $\{\widetilde{c}\}$ and the point on the model environment surface that is closest to the proxy PSM, and $\mathbf{K}_p$ is the VF stiffness gain matrix. The rotation ${}^{\widetilde{c}}\mathbf{R}_b$ rotates a vector in frame {b} to be represented in frame $\{\widetilde{c}\}$.

A nonzero stiffness in the x direction of the compliance frame was applied when the user was outside the finite length of the curve. Two imaginary planes were defined in the y-z plane of the VF compliance frame $\{\widetilde{c}\}$ at either end of the ablation path, Fig. 6.3. A point $\widetilde{\mathbf{s}}$ was determined to belong to the curve (i.e. $\widetilde{\mathbf{s}} \in curve$) if it was between these planes. The VF stiffness matrix was defined as:

$$\mathbf{K}_p = diag(k_x, k_y, 0) \tag{6.13}$$

$$k_x = \begin{cases} 0, & \text{if } \widetilde{\mathbf{s}} \in curve \\ k_y, & \text{otherwise.} \end{cases} \tag{6.14}$$

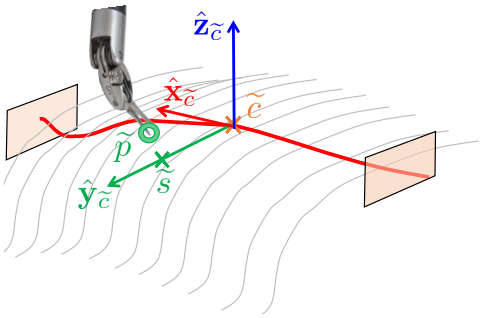

Figure 6.3: Path virtual fixture to push user's hand toward the closest point on the desired fixture curve.

6.2.6 Stiffness Estimation Using Gaussian Processes

As part of the *CSA* framework, a stiffness estimation module was included to semi-autonomously palpate the environment and create a stiffness map of the surface. Using software and methods developed by [179], a force-based sinusoidal palpation motion was superimposed over the user's movement commands during surface exploration. A sinu-

soidal force reference (in Newtons) was set into the controller in (6.2) as

$$\mathbf{f}_{ref} = 2\sin(5\pi t) + 2 \tag{6.15}$$

The motion and force information collected during palpation were used to define a Gaussian Process model of the interaction force as a function of the probe location. Using this model, the local stiffness can be calculated along the palpation direction by dividing the force difference by the distance between deep and shallow interaction points. Surface locations are estimated by calculating the zero-intercept of a linear fit of the interaction forces as a function of the palpation positions in a given palpation cycle.

In order to increase computational efficiency, local Gaussian process models were used to estimate forces within different areas of the surface. Two spatial hash grids were defined: one for the training set data and another for prediction data. By fitting models to local areas of the stiffness map, greater computational efficiency was achieved for online stiffness estimation. Additionally, because Gaussian process regression is sensitive to redundant data points, the hashing process prevented excess data from corrupting the regression. Details of the method are available in [179].

6.3 Experimental Setup

The experimental setup is shown in Fig. 6.4. Alongside the dVRK system explained in Section 6.2, an eYs3D (Taipei, Taiwan) EX8029 stereo camera with a 3cm baseline captured images for user feedback. Depending on the site, either a Nano 17 or a Gamma 6-axis force sensor from ATI (Apex, North Carolina) was mounted below the phantom kidney, as a stand-in for any of a number of force-sensing methods that could be integrated into a clinical system, as reviewed in [32, 183]. The PSM end-effector gripped a probe with a teflon sphere on its tip and optical tracking markers attached to the sides for position measurements using the Claron Technology (Ontario, Canada) MicronTracker 2 optical

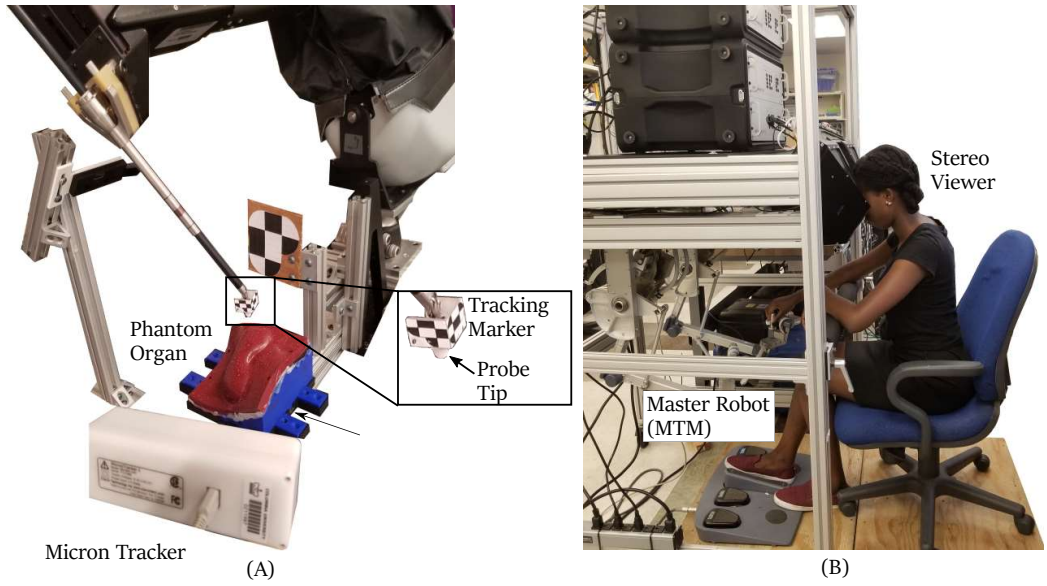

Figure 6.4: (A) Experimental setup for a user study, replicated at 3 universities (B) User grasping the MTM while looking into the stereo viewer

tracking system. The optical tracking of the end-effector was used to obtain as accurate an estimate of the PSM end effector motion as possible for the purpose of characterizing the actual motions of the end effector when telemanipulated by the users. This overcomes the lateral deflection of the probe when interacting forcefully with the environment. The RMS tooltip tracking error was 0.7mm in position and 2.3° as determined from a Monte Carlo simulation based on the manufacturer-reported accuracy of 0.2mm for a given tracked point.

6.3.1 Silicone Model Preparation

Two sets of silicone phantom organs were made for ablation and palpation tasks. The molding and mounting process can be seen in Fig. 6.5. The body of these phantoms were made of Ecoflex^{TM} silicone rubber (Smooth-On, Macungie, Pennsylvania). Fig. 6.5F shows the phantom organs glued to a 3D-printed platform with digitization divots to consistently deform them from their "preoperative" state of the mold geometry. The ablation phantoms were kept transparent and a red curved silicone rubber rod (durometer 40A) was

set into the ablation phantoms to represent a desired ablation path. The palpation phantoms were made of the same silicone, but dyed red to be opaque. A set of 2 or 3 hard teflon spheres were embedded below the surface where they could be felt, but not seen.

To find the location of the stiff features, CT scans of the organs were taken using a Xoran xCAT® ENT scanner (Xoran Technologies, Ann Arbor, MI) with isotropic voxels resolution of 0.3mm. These scans were manually segmented using intensity thresholding in 3D Slicer [220]. For the ablation phantom, the centroid of slices of the feature along the curve were used to define the center of the path. Because this results in a location beneath the surface of the organ, the points were projected onto the organ surface and refit on the surface with a cubic spline to ensure smoothness. For the palpation phantom, the center of the spherical inclusions were chosen as the ground truth location of the mock tumors.

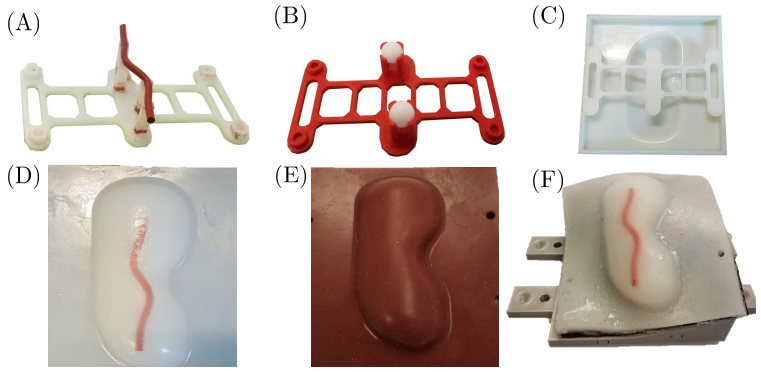

Figure 6.5: Example phantom kidneys created from silicone with embedded stiff features: A) Ablation phantom feature holder B) Palpation phantom feature holder C) Holder placed in organ mold D) Final ablation phantom E) Final palpation phantom F) Deformed phantom used in experiment was mounted to a base with digitization divots.

6.3.2 Organ and Stereo Registration

The use of a model-mediated controller requires an accurate model of the environment that is properly registered to the robot during telemanipulation. The location of the 3D printed base with respect to robot frame was obtained by using the PSM to digitize the centers of the divots in 3D printed base. The locations of the divot centers and the embedded spheres were also obtained in the CT frame through segmentation using 3D Slicer. Using

a fiducial localization error of 1mm when using the PSM to digitize the divots [218], the expected average target registration error (TRE [221]) for the points along the ablation path was 0.8 mm.

Because the focus of this study was not on intraoperative registration, we used the CT scans of the deformed organs as seen in Fig. 6.5F as inputs into the coherent point drift deformable registration algorithm [222] to generate the in-experiment environment surface models. The geometry of the silicone mold was used as the "preoperative" model to create a unique model for each phantom. This assumes more information than would typically be available in a surgical scenario, but could be replaced with some visual mapping method or previous methods we have presented using palpation for intraoperative registration [177, 159, 223]. Such intraoperative registration steps were excluded to maintain a reasonable experimental protocol duration.

A variety of image overlays were included in the experiment including a force bar that moves with the PSM tip and an STL model of the mock organ that was colored to display stiffness information obtained during palpation (note: the software for image overlay in a stereoscopic view was developed by collaborators at Carnegie Mellon University). To successfully achieve these overlays, the stereo camera was also registered to the robot frame. The spherical palpation tip attached to the PSM gripper shown in Fig. 6.4 was painted red and segmented using color segmentation. The stereo image to robot registration used paired-point rigid registration [224]. The point pairs were obtained by moving the PSM end-effector to a number of points in the robot workspace and collecting end-effector locations in robot frame and stereo frame. This registration was used directly for the force-bar overlay, but was not sufficiently accurate for the overlay of the model organ on the visible silicone phantom since small errors in registration orientation meant that portions of the overlay would intersect the real organ. This was overcome with manual adjustment of the model organ overlay to minimize user confusion.

	Unaided	Visual	Bilateral	FRMM
Control Mode	Unilateral	Unilateral	Bilateral	FRMM
Wrist VF	On	On	On	On
PVF	Off	Off	On	On
Overlay	None	Force Bar	Force Bar	Force Bar

Table 6.2: Assistance modes for mock ablation experiments.

6.4 User Study

A multi-site user study was carried out to characterize the effect of different assistance modes on the mock execution of two basic surgical tasks: ablation and palpation. 26 individuals were enrolled in an IRB-approved study. These participants were recruited from the student and local community populations at Vanderbilt, Johns Hopkins, and Carnegie Mellon Universities. Two users were removed from consideration due to data corruption, permitting a full analysis of 24 users. The same hardware and software setup was replicated at each site to show the cross-compatibility of this software framework. An example run-through of the user study can be found in Multimedia Extension 4, linked from Appendix A.4.

On arriving, after being consented, each user was given approximately 10 minutes to get familiarized with the system and how to use the robot. The user was then guided while carrying out the tasks in the following sections. After each section of the experiment, the user was asked to fill out a survey to subjectively evaluate their experience and the differences between the assistance modes.

In all modes, an orientational VF (Section 6.2.4) was applied to the user's wrist to assist in aligning the user with the local surface normal of the phantom organ. In preliminary experiments, inexperienced users often allowed the wrist to tilt very far from the surface normal unless assisted, so this assisted in maintaining proper probe orientation.

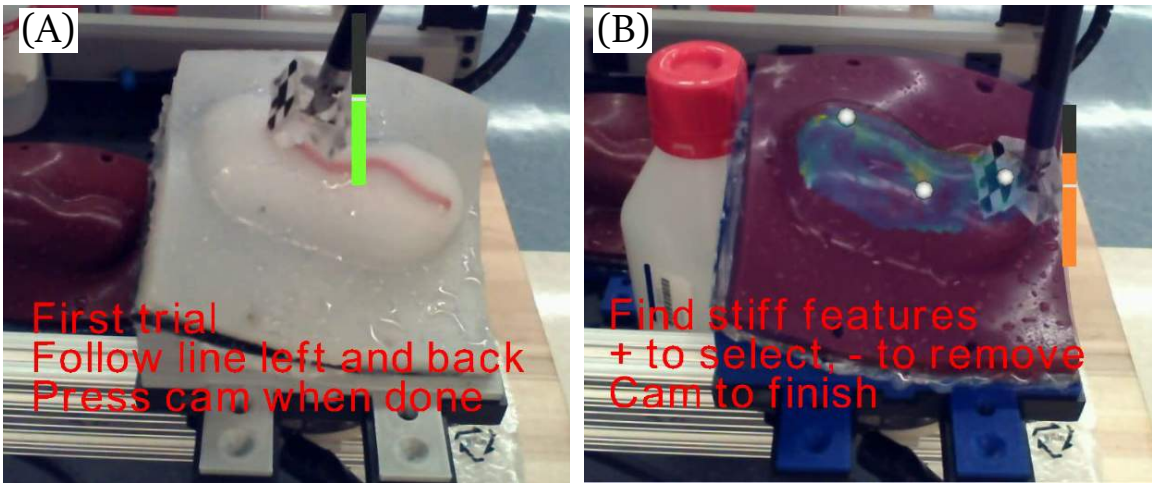

Figure 6.6: (A) Image from stereo viewer of user view during an ablation experiment. Force feedback measurement shown in the vertical bar, overlay text assists in giving instructions to the user. (B) Augmented reality view during palpation experiment of stiffness map overlaid on top of an organ with points selected by the user displayed on the organ's surface.

6.4.1 Mock Ablation Task

The mock ablation experiment consisted of following a visible path from one side of a silicone kidney phantom to the far side and back while maintaining a constant interaction force of 3 N. The path-following task was repeated for four different types of feedback modes as outlined in Table 6.2. For each mode, the task was completed three times, consecutively.

In the first mode, termed the "Unaided" mode, the user relied only on visual feedback through the MTM stereo viewer (i.e. no force feedback). This mode is comparable to current capabilities of commercial robotic surgical systems. To train each user to apply a constant target ablation force, they were instructed to slowly press into a bulk region of the phantom organ (i.e. not above a stiff feature) until the desired force was reached. Visual feedback about the force was presented to the user only during this training phase and it consisted of a color bar overlay as shown in 6.6A. A smooth color interpolation between red and green was used to indicate levels of force error. Pure green indicated the force was at the desired level and red indicated a force error was at or larger than 3N. After training

with the color bar overlay, each user was asked to reach the target force without the bar's assistance. Before commencing the ablation experiments, each user was expected to repeat their training and validation with/without the color bar until they were able to reach the desired force of 3N at least 3 times out of a set of 5 consecutive attempts.

In the second "Visual" mode, the user still had no haptic assistance in completing the task, but was aided by the color overlay of ablation force. This visual force feedback was also present in all the subsequent modes.

In the third mode, the user operated using bilateral telemanipulation. In addition, a PVF was added to the MTM such that the user's hand was pushed to follow the shape of the desired curve. The bilateral telemanipulation provided direct force feedback on the master in order for the user to attempt to apply a consistent desired contact force in the normal direction of the organ surface under both kinesthetic feedback from the master and visual guidance using the force bar.

In the fourth mode, the user operated using FRMM alongside the same tangential alignment PVF as the previous mode. Using FRMM, the master interacted with a constant-stiffness virtual environment model while the PSM independently was under hybrid position-force control. This allowed the user to maintain control of the telemanipulation direction and when to make/leave contact, but severed the direct link between master and slave allowing the slave to independently control interaction forces to increase safety and improve force regulation.

6.4.2 Organ Palpation Task

The second benchmark task was organ palpation to find hidden subsurface features. We therefore investigated the reliability and efficacy of detecting hidden subsurface features using robot-assisted telemanipulation.

The two feedback modes used for telemanipulated palpation are summarized in Table 6.3. In the first mode, the user had only direct force feedback through bilateral telemanipu-

	Bilateral	FRMM + Overlay
Control Mode	Bilateral	FRMM + Sinusoid
Wrist VF	On	On
PVF	Off	Off
Overlay	Force Bar	Force Bar, Stiffness Map

Table 6.3: Assistance modes for mock organ palpation experiments.

lation and they were also aided by the same colorbar overlay as in the ablation experiments.

In the second mode, "FRMM+Overlay" the same palpation task was carried out, but under FRMM control. A sinusoidal profile used as the reference force in the force controller to provide an exciting motion was used for stiffness estimation. The measured forces were not relayed back to the user directly and instead were fed into the GP stiffness mapping method presented in Section 6.2.6. This stiffness map was visually overlaid on top of the organ in the stereo viewer for the user to see where potential locations of high stiffness might exist. Users could at any time digitize the location of stiff features by pressing a footpedal. Digitized locations were overlaid with a sphere on the organ surface as shown in Fig. 6.6B.

For each mode, users attempted to find stiff subsurface features in 2 phantom organs, repeating each organ once, for a total of 4 trials per control mode. The order of organs was randomized for each user and the users were blinded to the order in which the organs were presented to them.

6.5 Results

6.5.1 Mock Ablation

The performance of users was evaluated based on the performance metrics shown in Table 6.4. The key metrics were the lateral path following error calculated as the mean norm lateral error from the path, the mean force regulation error along the path, the average completion time for each back-and-forth pass over the ablation path, and the path

coverage, which is defined as the percentage of path length during which contact between the end-effector tip and the mock anatomy was registered by the load cell. This metric was calculated by discretizing the desired path and calculating the closest segment for each position of the robot while in contact.

Referring to Table 6.4 for the mock ablation experimental results, it can be seen that the users were able to complete the task best in all metrics using the fourth mode under FRMM control. Statistical comparisons of metrics between the 4 groups was performed via Tukey's honest significant difference criterion using MATLAB's statistical toolbox. This gives an estimate for significant difference of the means between the 4 groups while accounting for the additional errors brought by testing differences among all the groups.

The path coverage metric was calculated by cutting the desired path into discrete segments and calculating the closest segment for each position of the robot in contact. The proportion of these segments identified as closest to a point on the robot path characterizes the "coverage". If users frequently lost contact with the organ during task execution, this metric captures those effects. The average coverage for the unassisted mode (97%) was significantly less than the coverage in all the other modes ($p < 0.002$).

Force regulation errors were calculated as the mean difference between the contact force and the desired regulation force of 3 N. This was only calculated when the user made contact with the organ. This metric had 3 groups of results, shown in Fig. 6.7A. The unaided results had significantly worse force regulation errors than all other groups with a group mean error of 1.63 N. The results with direct feedback in the Visual and Bilateral modes had lower errors with means of 0.68 N and 0.67 N, respectively. There was no significant difference between these two groups. Outperforming all these results was the FRMM mode with a mean error of 0.30 N, which significantly improved force regulation over all other methods. For all these comparisons, ($p < 0.0001$).

Path-following errors were calculated by projecting the current robot position into a plane fit to the desired path and calculating the distance between the projected current point

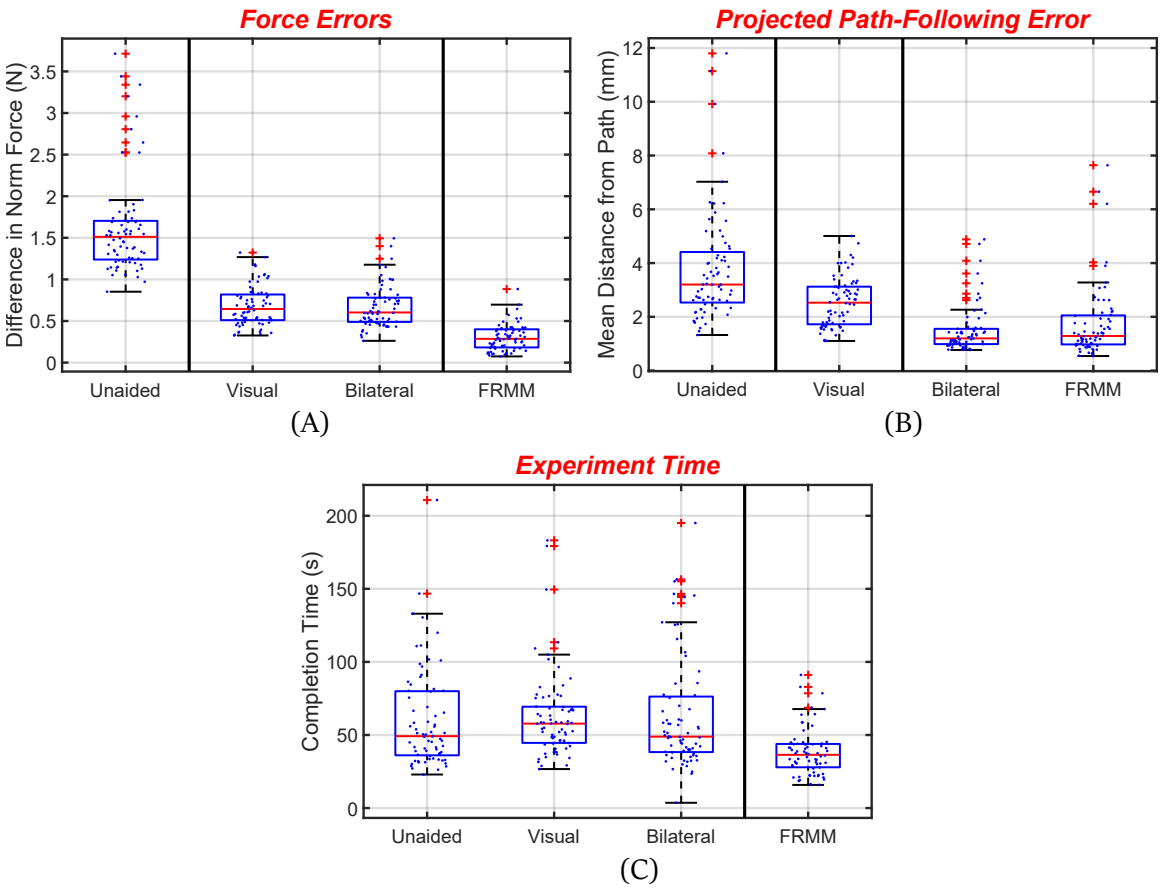

Figure 6.7: Boxplots of results in mock ablation tasks - the central red line is the median, with the box covering the 25th to 75th percentiles of the data. Outliers, plotted with a cross, are outside 2.7 standard deviations from the mean, assuming normality. Small dots represent all the experimental data points. Vertical bars separate groups with significantly different means. (A) Force regulation errors (B) Path-following errors (C) Completion time

	Unaided	**Visual**	**Bilateral**	**FRMM**
Path Coverage (%)	97	99	99	100
Force Error (N)	1.61	0.69	0.67	0.31
Path Error (mm)	3.8	2.5	1.5	1.7
Completion Time (s)	60	63	64	38

Table 6.4: Results for ablation experiments. Refer to Table 6.2 for the definition of user assistance modes and control modes used.

to the projected curve points. This separates path-following errors from force errors so that errors in the surface normal direction are not double-counted as both force errors and path-following errors. As shown in Fig. 6.7B, the final two modes using a PVF significantly improved path-following over the first two modes ($p < 0.004$). The Visual mode also had reduced errors when compared to the Unaided mode ($p < 0.0001$).

The completion time, in Fig. 6.7C, was calculated as the total time required to complete one cycle of ablation (moving from one end of the path and back) and was found to be significantly reduced in FRMM compared to all other modes, ($p < 0.0002$), which were not significantly different from each other.

6.5.2 Organ Palpation

The palpation experiments did not have as many strong differences as the ablation experiments. The metrics for these experiments are shown in Table 6.5. To determine selection accuracy, each point selected by the user as a possible location for a hard “mock tumor" was marked as either being “close to” one of the subsurface features or not. If multiple points were selected close to an actual feature, the closest point was taken as the only accepted point and the other points were designated as additional selected points, not belonging to any feature. As shown in Fig. 6.8, each tumor had some minimum distance to the surface d_{min}. When a user digitized a point, the closest point to the surface, $\mathbf{s}$, was found and its distance to the center of the tumor was calculated as d_{select}. If $d_{select} - d_{min} < 0.8mm$, the selected point was designated as “close” to that particular tumor. This metric, rather than the pure distance across the surface of the organ from $\mathbf{s_{min}}$ to $\mathbf{s}$ better captured closeness to a tumor on curved surfaces.

Boxplots of the experimental results are shown in Fig. 6.9. For both methods, many excess points were found by users - on average 1.9 excess points were selected by users in the bilateral experiments and 1.5 in the FRMM+Overlay experiments, but the distribution had a high variance and this difference had weak statistical significance ($p = 0.0715$). At

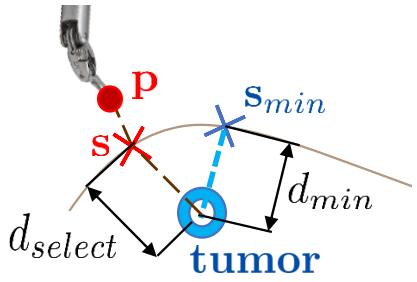

Figure 6.8: User-selected locations were determined "close" to a particular mock tumor if d_{select} was within 0.8 mm of d_{min}

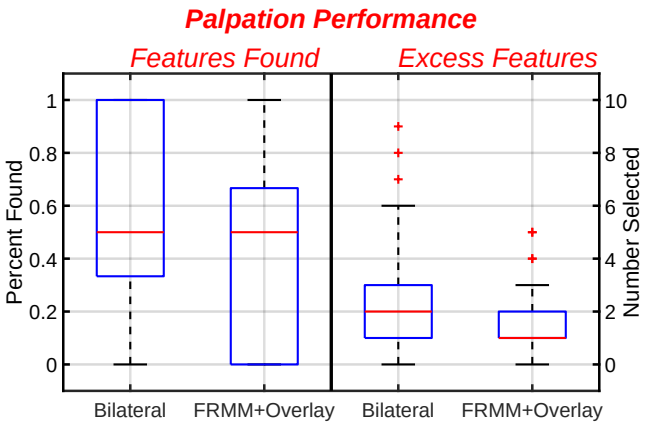

Figure 6.9: Percent of features found and excess features found in palpation modes. Fig. 6.7 details boxplot formulation.

the same time, many points were missed - on average users only found 54% of the features in an organ in the haptic experiments and 43% in the GP-guided experiments. This result was statistically significant ($p = 0.0235$).

Users were able to complete experiments with haptic feedback in the Bilateral mode more quickly than when using the visual stiffness data (333 vs. 268 seconds, $p = 0.013$ using a 2-sample t-test).

6.5.3 Subjective Results

A questionnaire was given to each user enrolled in the study. A series of questions were asked of each user before, after, and during the experiments. For both tasks, the mode with the most assistance (FRMM) was preferred by a majority of users and users reported

	Bilateral	FRMM+Overlay
Excess Features	1.9	1.5
Features Found (%)	54	43
Total Time (s)	268	333

Table 6.5: Results of palpation experiments: similar feature-finding accuracy was found for both modes with reduced time using bilateral telemanipulation.

significantly reduced effort in that mode.

For the ablation experiments, a majority (69% of users) preferred the FRMM mode, with 7% preferring the Bilateral mode and 27% preferring the Visual mode. No users preferred the Unaided mode. In the palpation task, 84% of users preferred FRMM+Overlay over Bilateral assistance.

After completing each experimental mode, users were asked a series of questions on a scale of 1 to 7 using the NASA/TLX scale evaluating mental/physical effort and difficulty of the task they had just completed where higher scores indicate a demanding task that requires a large amount of focus and difficulty [201]. The results of these questions are charted in Fig. 6.10. In ablation, the FRMM mode significantly reduced TLX effort scores over all the other groups ($p < 0.006$) with a mean of 9.4 compared to the other modes with mean scores above 14. In the palpation experiments, the FRMM+Overlay mode was also associated with significantly reduced aggregate TLX effort scores ($p = 0.002$) with a mean score of 13.3 compared to a mean score of 18.3 using haptic feedback.

6.6 Discussion

We found that our model-mediated telemanipulation framework with assistance modes greatly increased the ability of users to regulate positions and forces during a path-following task and reduced user effort during palpation.

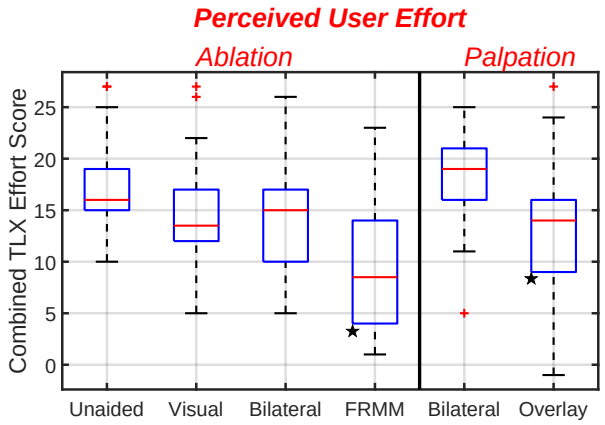

Figure 6.10: NASA/TLX scores from users in all experimental conditions: ablation experiments on the left, palpation on the right. Stars indicate a significant difference in mean effort from other modes in that experiment type. Fig. 6.7 details boxplot formulation.

6.6.1 Ablation Task

The reduction in path coverage in the Unaided control mode indicated that users tended to lose contact in that mode when there was no force feedback, as would be expected. As the coverage still had an average of 97%, most users did not lose a very large amount of contact with the path, but the difference still may be important depending on the clinical context.

The difference in quality of contact is more pronounced in force regulation errors. When completely unaided, force regulation errors were much higher than when some form of guidance was added. The Visual and Bilateral modes were indistinguishable, indicating that the addition of kinesthetic feedback in the Bilateral mode was not useful in better force regulation. Since both tasks used visual feedback, that may be sufficient in completing similar tasks. The use of semi-automated force regulation using the FRMM mode allowed further reductions in force regulation errors, showing the utility of shared control for accurate forceful interaction tasks.

In the success of path-following, the Bilateral and FRMM modes both had the least errors due to the use of a PVF pushing the users to follow the path closely. Also, even

though no feedback about path-following was introduced between the Unaided and Visual modes, the Visual mode also presented reduced path-following errors over the Unaided mode. It can be hypothesized that the additional contact information helped users reduce mental effort spent on regulating contact forces, allowing them to focus more on the line-following task, reducing path-following errors.

Only the FRMM mode showed a decrease in completion time. While other feedback methods improved performance via some of the other metrics, it appears that either a certain threshold of assistance is necessary before time can be reduced, or that the force-regulation task is much more complicated and slows users without semi-automated assistance. This result indicates that speed does not have to be compromised in order to improve task-completion performance, as the FRMM mode also improved the other metrics as well.

Subjective responses indicated that the majority of users preferred the FRMM mode. Also, the use of the FRMM did not impede telemanipulation intuitiveness and improvements in task execution metrics did not diminish user comfort.

The presence of a subgroup preferring no force feedback suggests that visual feedback may be more useful or intuitive for enabling users to control robot motion and make intelligent decisions regarding interaction forces. It may be instructive to further elucidate exactly how visual perception compares to force feedback, as in this study there was no difference in a user's ability to perform a force-regulation task when force feedback was added in addition to a visual cue.

In this experiment, a constant interaction force was desired throughout the entire experiment. Other control options would need to be presented to the user to adapt this framework to allow for user-controlled changes in the regulation forces.

6.6.2 Palpation Task

The results from the palpation experiments were more mixed than those of the ablation experiments. Although the semi-automated palpation mode did not show improvement in

the identification of subsurface features compared to direct haptic feedback in the Bilateral mode, users preferred more assistance during palpation tasks, suggesting the proposed method's potential utility, pending further development.

We believe there are a number of reasons why palpation was difficult in both modes. The long probe grasped by the gripper in order to allow for optical tracking for better ground truth measurement was a challenge in that it extended the lever arm of the wrist, which is somewhat compliant during high-force interaction events. While the wrist alignment VF assisted users in reducing the effects of this problem, it was likely still a source of reduced efficacy.

An issue in the results using direct force feedback of the MTM of the dVRK is that the MTM, while capable of providing force feedback, was not designed to be a high-fidelity haptic device. The utility of future haptic feedback systems using force feedback may be improved by investigating alternative haptic feedback devices that may allow for better user understanding of probe-environment interaction forces than the MTM.

6.7 Conclusion

We presented a framework for model-mediated telemanipulation and the assessment of various haptic and visual feedback methods for assistance in task completion during forceful interaction with simulated surgical tasks.

In the regulation of forces, we showed that our model-mediated control method with visual feedback, semi-autonomous force control, and VF assistance could improve accuracy in path following, reduce errors in force regulation, decrease experiment time, and also reduce users' mental burden. This is a promising result indicating that future research could benefit from using elements of this interaction scheme to improve surgical quality and reduce mental load on surgeons.

In the exploration of palpation, we found that visual feedback provided less stress and more comfort and confidence of users while performing palpation tasks. However, while

users preferred the assistive mode, they did not perform better than when using kinesthetic feedback in a standard bilateral telemanipulation architecture.

Future work should include further investigation of palpation methods for improving the ability to find subsurface features in a rapid and accurate manner. Further exploration of semi-automated force regulation should be pursued both for other tasks within MIS and in other environments requiring force regulation during task execution in telemanipulated systems.

CHAPTER 7
CONCLUSIONS

In MIS and RAMIS, surgeons are faced with manipulation, sensing and perception challenges that impede their ability to understand the surgical environment and appropriately manipulate the surgical system to accomplish their desired tasks. This dissertation explored means for overcoming some of these challenges within the context of deep and narrow surgical fields and ways for providing complementary perception where normal human sensing would normally fall short. To allow surgeons to safely interact with anatomy this dissertation explored the question of how to collect useful intraoperative data to improve surgeons' situational awareness and how to present useful feedback methods or semi-autonomous task execution to assist surgeons in task completion.

7.1 Summary of Findings

This dissertation has presented works toward assisting the future of robotic surgery and assistive features in a number of domains and research areas.

In the middle ear, methods were explored for robotic disease removal. The proposed method could improve stability and fine manipulation control while also expanding the available workspace available for disease removal. While this is a useful result, there are a number of obstacles to the implementation of a system for robotic middle-ear surgery in practice. A unified method for controlling both robotic motion and endoscopic visualization would greatly improve usability, especially if collision avoidance between these two components can be achieved. Additionally, the lack of force sensing and meaningful feedback about the state of the robot's interaction with the environment posed a challenge to surgeons when using this system. This particular challenge motivated the work in the subsequent chapters of this thesis on improving feedback modalities for better understand-

ing of the surgical scene and for information collection during surgery.

During cochlear implant insertion, this dissertation investigated the utility of visual inspection combined with tool tracking for more repeatable surgical execution. The intracochlear inspection method did not appear to significantly change surgeons' behavior compared to using extracochlear microscopic visualization; either different inspection modalities or additional training would be required to generate a better sense of the anatomy before starting a procedure. However, the use of tracked instruments and guidance was able to improve surgeons' ability to follow a planned insertion method repeatably. This motivates future work in combining tool tracking and guidance with additional inspection and imaging methods that can create accurate and repeatable electrode insertion practices.

Because one of the main difficulties of robotic manipulation and information extraction in RAMIS is in the forceful interaction of robots with their environment, the next chapter of this dissertation explored the ability of continuum robots to scan their environment and sense forces. A hybrid position-force controller was used, updating prior work, for continuum robots to assist in blind environment palpation. This used both a mixed-feedback controller with external force sensing and blind exploration utilizing joint-level ex-situ force sensing for guidance without requiring any external sensing. New methods were developed to allow for friction compensation in force sensing using compensation in joint-space with hysteresis-accounting features. Model calibration parameters were developed and used to improve force regulation performance in semi-automated task execution using JEFS for force feedback during the execution of a variety of tasks.

In domains beyond continuum robot environment interaction, there are many problems to be solved in regulating forceful environment interaction and extracting information from force sensing in RAMIS. To this end, work was completed on the use of feedback methods in an assistive telemanipulation framework to improve user comfort and increase performance measured via a number of task execution metrics.

Within a model-mediated telemanipulation framework, methods were developed for

increased user assistance and model-updates during prolonged environment interaction. This included the development of assistive virtual fixtures for better force regulation and a hybrid control framework that allowed for automated force regulation during environment interaction and updates of the model-interaction to maintain haptic continuity during long periods of interaction.

The methods developed in this thesis are able to support the development of future surgical systems capable of deep anatomical access while providing both sensing and guidance techniques. This will provide surgeons with better situational awareness to carry out tasks more safely and accurately. The use of partial task autonomy can relieve surgeons from the mental burden of regulating interaction forces and tight path following during key tasks such as force-controlled ablation while also relieving their mental burden, letting them be more free to concentrate on high-level surgical planning and evaluation instead of low-level task execution.

7.2 Future Research Directions

The work presented in this thesis opens the door for future exploration in a variety of avenues. Much of this research has been on how to bridge the gap between unassisted surgical interventions and fully autonomous motion. In the future, pending technological developments and regulatory permissions, it may be possible to transition these technologies to allow for fully autonomous surgical procedures. However, in the meantime, a number of developments are required.

As mentioned above, a deployable middle-ear surgical system would require the combination of robotic manipulation and some form of non-manual visualization. The integration of an endoscope into the robotic system would allow easier use by a surgeon as well as collision-free execution without the user needing to control the position of the robot and the visualization method. Additionally, the use of simultaneous visualization would allow for visual servoing so that the surgeon could control the end-effector in the image frame,

not in the frame of the robot itself. Finally, for the ability to remove disease and perform more complex procedures, a more varied tool armamentarium would need to be developed, including more powerful grippers that would be able to pull off the skin growth associated with cholesteatoma or similar disease states.

In cochlear implant insertion, the combination of tool tracking with preoperative imaging would make a powerful next step in improving surgeons' ability to create surgical plans and execute them accurately during surgery. Additionally, as new electrode designs are being tested, new methods for tracking and guidance will be useful for future development of closed loop implant insertion. The correlation of particular surgical practices and tool motions with electrode placement results and hearing outcomes can also lead to the development of better best practices in implant insertion surgery.

Force sensing in continuum and surgical robots is still at an incipient phase and there are a number of directions in which future research can be explored. Next steps that could directly extend the work presented here include extended models that include inter-segment coupling for frictional effects and internal moments and alternate methods for friction regression. Alternate machine learning techniques using neural networks and memory blocks may be able to further reduce the errors in joint level force regression and estimation in the presence of hysteretical behavior. More robust model parameters should be developed that can capture transmission behavior across varied loading conditions - this may require alternate formulations or more dense loading datasets to capture less easily modeled nonlinearities.

In the physical embodiment of continuum arms for force sensing, lower friction guides and bearings could be added to the wire-routing cone for similar designs. This could reduce overall transmission load losses and decrease uncertainties in the force sensing equations. The development of low-cost, miniature loadcells would also facilitate the placement of measurements closer to the continuum segments, allowing estimation with fewer uncertainties.

In the use of continuum robots to scan soft environments, it was found that particular scanning directions caused interactions that resulted in unstable force regulation and led to the robot jabbing into the environment. The reasons for why this occurs when moving "away" from the robot base are a function of the deformed kinematics of the robot and its environment. A more elaborate robot-environment interaction model would be able to anticipate these possibilities in a unified way for a range of continuum robot geometries.

In order to achieve better telemanipulation guidance in Chapter 6, a combination of virtual fixtures and model-mediated guidance were used to assist the user in the performance of a force regulation task and a forceful exploration task. Since both of these methods rely on well-registered environment models, an important piece of the next research step is establishing methods for intraoperative deformable registration pipelines.

Additionally, while the assistive methods for force regulation were successful in improving all measured metrics, the palpation-guided stiffness estimation did not present such improvement. Potential methods to increase the accuracy of palpation-guided exploration include the use of nonlinear stiffness models or the capture of more complex surface features through mechanics models of the environment. Additionally, the flexibility of the robot wrist impeded robotic palpation, so performance may also be improved through more rigid robot design.

This research did not yet integrate intraoperative sensing methods inside a model-mediated telemanipulation framework. Evaluation of the proposed assistance modes using clinically deployable sensing methods such as JEFS or other estimation based on embedded sensors or deflection tracking are required to translate this technology into practically useful technology for RAMIS. This may require adjustments to the model-mediated framework due to the additional uncertainties introduced by online force estimation techniques.

This thesis has proposed a number of methods for the improvement of obtaining information during surgery and using that additional information to assist surgeons in accomplishing a variety of surgical tasks. These stepping stones should be useful for future

researchers and engineers to improve surgical quality by improving task precision and integrating more areas of intraoperative sensing and partial task automation.

Appendices

A.1 Journal Publications

Yasin, R., Simaan, N. Joint-level force sensing for indirect hybrid force/position control of continuum robots with friction. Submitted to *International Journal of Robotics Research*.

Yasin, R., Chalasani, P., Zevallos N., Shahbazi M., Li, Z., Deguet, A., Kazanzides, P., Choset, H., Taylor, R.H., Simaan, N. Evaluation of Hybrid Control and Palpation Assistance for Situational Awareness in Telemanipulated Task Execution. Submitted to *IEEE Transactions on Robotics*.

Yasin, R., Dedmon, M, Dillon, N, Simaan, N. (2019) Investigating Variability in Cochlear Implant Electrode Array Alignment and the Potential of Visualization Guidance. *International Journal of Medical Robotics and Computer Assisted Surgery*.

Simaan, N., **Yasin, R.** M., Wang, L. (2018). Medical Technologies and Challenges of Robot-Assisted Minimally Invasive Intervention and Diagnostics. *Annual Review of Control, Robotics, and Autonomous Systems*, 1, 465-490.

Chalasani, P., Wang, L., **Yasin, R.**, Simaan, N., Taylor, R. H. (2018). Preliminary Evaluation of an Online Estimation Method for Organ Geometry and Tissue Stiffness. *IEEE Robotics and Automation Letters*, 3(3), 1816-1823.

Wang, L., Chen, Z., Chalasani, P., **Yasin, R.** M., Kazanzides, P., Taylor, R. H., Simaan, N. (2017). Force-controlled exploration for updating virtual fixture geometry in model-mediated telemanipulation. *Journal of Mechanisms and Robotics*, 9(2).

Yasin, R., O'Connell, B. P., Yu, H., Hunter, J. B., Wanna, G. B., Rivas, A. et al. (2017). Steerable Robot-assisted Micromanipulation in the Middle Ear: Preliminary Feasibility Evaluation. *Otology & Neurotology*, 38(2), 290-295.

A.2 Conference Publications

Yasin, R., Wang, L., Abah, C., Simaan, N. (2018). Using continuum robots for force-controlled semi autonomous organ exploration and registration. *International Symposium on Medical Robotics (ISMR)* (pp. 1-6).

Salman, H., Ayvali, E., Srivatsan, R.A., Ma, Y., Zevallos, N., **Yasin, R.**, Wang, L., Siman, N. and Choset, H. (2017). Trajectory-optimized sensing for active search of tissue abnormalities in robotic surgery. *IEEE Conference on Robotics and Automation (ICRA)*.

Yasin, R., Aiello, G., Simaan, N (2017). Exploring Reflected Light Intensity to Estimate Depth of the Basal Turn in Cochlear Implant Surgery. *The Hamlyn Symposium on Medical Robotics.*

O'Connell, B., Yu, H., Rivas, A., Hunter, J., **Yasin, R.**, Wanna, G., Simaan, N. Steerable Robot Assisted Micro-Manipulation in the Middle Ear: Preliminary Feasibility Evaluation. *Combined Otolaryngology Society Meeting (COSM)*. Chicago, Illinois.

A.3 Publications in Preparation

Shihora, N., **Yasin, R.**, Simaan, N. Feasibility of Robotic Cricothyrotomy Localization. In Preparation For *2020 IEEE/RSJ International Conference on Intelligent Robots and Systems.*

A.4 List of Multimedia Extensions

There are four multimedia extensions that are available online for understanding of additional content. These have been made available on the ARMA lab website at: http://arma.vuse.vanderbilt.edu/index.php?option=com_content&view=article&id=196&catid=2

1. Multimedia Extension 1: IREP Palpation Using Mixed Feedback
2. Multimedia Extension 2: Joint-Level Force Sensing of the IREP System
3. Multimedia Extension 3: Joint-Level Force Sensing for Palpation

4. Multimedia Extension 4: dVRK User Study for Telemanipulation Assistance

BIBLIOGRAPHY

[1] Nabil Simaan, Rashid M. Yasin, and Long Wang. Medical Technologies and Challenges of Robot-Assisted Minimally Invasive Intervention and Diagnostics. *Annual Review of Control, Robotics, and Autonomous Systems*, 1(1):465–490, may 2018.

[2] Henry Gray. *Anatomy of the human body*, volume 8. Lea & Febiger, 1878.

[3] Preetham Chalasani, Anton Deguet, Peter Kazanzides, and Russell H Taylor. A computational framework for complementary situational awareness (csa) in surgical assistant robots. In *2018 Second IEEE International Conference on Robotic Computing (IRC)*, pages 9–16. IEEE, 2018.

[4] C Cao, Christine L MacKenzie, and Shahram Payandeh. Task and motion analyses in endoscopic surgery. In *Proceedings ASME Dynamic Systems and Control Division*, pages 583–590. Citeseer, 1996.

[5] Frank Tendick, Russell W Jennings, Gregory Tharp, and Lawrence Stark. Sensing and manipulation problems in endoscopic surgery: experiment, analysis, and observation. *Presence: teleoperators & virtual environments*, 2(1):66–81, 1993.

[6] Ori Ben-Porat, Moshe Shoham, and Joachim Meyer. Control design and task performance in endoscopic teleoperation. *Presence: Teleoperators & Virtual Environments*, 9(3):256–267, 2000.

[7] Valentina Vitiello, Su-Lin Lee, Thomas P Cundy, and Guang-Zhong Yang. Emerging robotic platforms for minimally invasive surgery. *IEEE reviews in biomedical engineering*, 6:111–126, 2012.

[8] Andrew L Orekhov, Colette Abah, and Nabil Simaan. Snake-like robots for minimally invasive, single port, and intraluminal surgeries. In Rajni Patel, editor,

The Encyclopedia of Medical Robotics, volume 1, chapter 8, pages 203–243. World Scientific Publishing Co, 2018.

[9] R. J. Hendrick, C. R. Mitchell, S. D. Herrell, and R. J. Webster. Hand-held transendoscopic robotic manipulators: A transurethral laser prostate surgery case study. *The International Journal of Robotics Research*, 34(13):1559–1572, 2015.

[10] Nima Sarli, Giuseppe Del Giudice, Smita De, Mary Dietrich, S Duke Herrell, and Nabil Simaan. Turbot: a system for robot-assisted transurethral bladder tumor resection. *IEEE/ASME Transactions on Mechatronics*, 2019.

[11] Andrea Bajo, Ryan B. Pickens, S. Duke Herrell, and Nabil Simaan. Constrained motion control of multisegment continuum robots for transurethral bladder resection and surveillance. *Proceedings - IEEE International Conference on Robotics and Automation*, pages 5837–5842, 2013.

[12] Young-Sik Kwon, Kyung Tae, and Byung-Ju Yi. Suspension laryngoscopy using a curved-frame trans-oral robotic system. *International journal of computer assisted radiology and surgery*, 9(4):535–540, 2014.

[13] Patrick S Jensen, Kenneth W Grace, Rajpaul Attariwala, J Edward Colgate, and Matthew R Glucksberg. Toward robot-assisted vascular microsurgery in the retina. *Graefe's archive for clinical and experimental ophthalmology*, 235(11):696–701, 1997.

[14] Hari Das, Haya Zak, Jason Johnson, John Crouch, and Don Frambach. Evaluation of a telerobotic system to assist surgeons in microsurgery. *Computer Aided Surgery*, 4(1):15–25, 1999.

[15] Russell Taylor, Pat Jensen, Louis Whitcomb, Aaron Barnes, Rajesh Kumar, Dan Stoianovici, Puneet Gupta, ZhengXian Wang, Eugene Dejuan, and Louis Kavoussi.

A steady-hand robotic system for microsurgical augmentation. *The International Journal of Robotics Research*, 18(12):1201–1210, 1999.

[16] Cameron N Riviere, Wei Tech Ang, and Pradeep K Khosla. Toward active tremor canceling in handheld microsurgical instruments. *IEEE Transactions on Robotics and Automation*, 19(5):793–800, 2003.

[17] H. Yu, J. Shen, K. M. Joos, and N. Simaan. Calibration and integration of b-mode optical coherence tomography for assistive control in robotic microsurgery. *IEEE/ASME Transactions on Mechatronics*, 21(6):2613–2623, Dec 2016.

[18] Nabil Simaan, Rusell H Taylor, and Howie Choset. Intelligent surgical robots with situational awareness. *Mechanical Engineering Magazine Select Articles*, 137(09):S3–S6, 2015.

[19] Austin Reiter and Peter K Allen. An online learning approach to in-vivo tracking using synergistic features. In *Intelligent Robots and Systems (IROS), 2010 IEEE/RSJ International Conference on*, pages 3441–3446. IEEE, 2010.

[20] Matthew Baumann, Simon Leoonard, Elizabeth A. Croft, and James J. Little. Path planning for improved visibility using a probabilistic road map. *IEEE Transactions on Robotics*, 26(1):195–200, 2010.

[21] S. LÃl'onard, E. A. Croft, and J. J. Little. Planning collision-free and occlusion-free paths for industrial manipulators with eye-to-hand configuration. In *2009 IEEE/RSJ International Conference on Intelligent Robots and Systems*, pages 5083–5088, Oct 2009.

[22] Nima Sarli and Nabil Simaan. Minimal visual occlusion redundancy resolution of continuum robots in confined spaces. In *2017 IEEE/RSJ International Conference on Intelligent Robots and Systems (IROS)*, pages 6448–6454. IEEE, 2017.

[23] Nazim Haouchine, Winnie Kuang, Stephane Cotin, and Michael Yip. Vision-based force feedback estimation for robot-assisted surgery using instrument-constrained biomechanical three-dimensional maps. *IEEE Robotics and Automation Letters*, 3(3):2160–2165, 2018.

[24] Masaya Kitagawa, Allison M Okamura, Brian T Bethea, Vincent L Gott, and William A Baumgartner. Analysis of suture manipulation forces for teleoperation with force feedback. In *International Conference on Medical Image Computing and Computer-Assisted Intervention*, pages 155–162. Springer, 2002.

[25] Gregory S Fischer, Takintope Akinbiyi, Sunipa Saha, Jason Zand, Mark Talamini, Michael Marohn, and Russell Taylor. Ischemia and force sensing surgical instruments for augmenting available surgeon information. In *Biomedical Robotics and Biomechatronics, 2006. BioRob 2006. The First IEEE/RAS-EMBS International Conference on*, pages 1030–1035. IEEE, 2006.

[26] Antonio Garcia-Ruiz, Michel Gagner, Jeffrey H Miller, Charles P Steiner, and Joseph F Hahn. Manual vs robotically assisted laparoscopic surgery in the performance of basic manipulation and suturing tasks. *Archives of surgery*, 133(9):957–961, 1998.

[27] C. R. Wagner, N. Stylopoulos, and R. D. Howe. The role of force feedback in surgery: analysis of blunt dissection. In *Proceedings 10th Symposium on Haptic Interfaces for Virtual Environment and Teleoperator Systems. HAPTICS 2002*, pages 68–74, 2002.

[28] Christopher R Wagner, Nicholas Stylopoulos, Patrick G Jackson, and Robert D Howe. The benefit of force feedback in surgery: Examination of blunt dissection. *Presence: teleoperators and virtual environments*, 16(3):252–262, 2007.

[29] Anand Pillarisetti, Maxim Pekarev, Ari D Brooks, and Jaydev P Desai. Evaluating

the role of force feedback for biomanipulation tasks. In *Haptic Interfaces for Virtual Environment and Teleoperator Systems, 2006 14th Symposium on*, pages 11–18. IEEE, 2006.

[30] Gregory Tholey, Jaydev P Desai, and Andres E Castellanos. Evaluating the role of vision and force feedback in minimally invasive surgery: New automated laparoscopic grasper and a case study. In *International Conference on Medical Image Computing and Computer-Assisted Intervention*, pages 198–205. Springer, 2003.

[31] Katherine J Kuchenbecker, Netta Gurari, and Allison M Okamura. Quantifying the value of visual and haptic position feedback during force-based motion control. In *EuroHaptics Conference, 2007 and Symposium on Haptic Interfaces for Virtual Environment and Teleoperator Systems. World Haptics 2007. Second Joint*, pages 561–562. IEEE, 2007.

[32] Pinyo Puangmali, Kaspar Althoefer, Lakmal D Seneviratne, Declan Murphy, and Prokar Dasgupta. State-of-the-art in force and tactile sensing for minimally invasive surgery. *IEEE Sensors Journal*, 8(4):371–381, 2008.

[33] Ulrich Seibold, Bernhard Kubler, and Gerd Hirzinger. Prototype of instrument for minimally invasive surgery with 6-axis force sensing capability. In *Robotics and Automation, 2005. ICRA 2005. Proceedings of the 2005 IEEE International Conference on*, pages 496–501. IEEE, 2005.

[34] Peter J Berkelman, Louis L Whitcomb, Russell H Taylor, and Patrick Jensen. A miniature microsurgical instrument tip force sensor for enhanced force feedback during robot-assisted manipulation. *IEEE Transactions on Robotics and Automation*, 19(5):917–921, 2003.

[35] Arianna Menciassi, Anna Eisinberg, Maria Chiara Carrozza, and Paolo Dario. Force

sensing microinstrument for measuring tissue properties and pulse in microsurgery. *IEEE/ASME transactions on mechatronics*, 8(1):10–17, 2003.

[36] Hiroki Takahashi, Shin'ichi Warisawa, Mamoru Mitsuishi, Jumpei Arata, and Makoto Hashizume. Development of high dexterity minimally invasive surgical system with augmented force feedback capability. In *Biomedical Robotics and Biomechatronics, 2006. BioRob 2006. The First IEEE/RAS-EMBS International Conference on*, pages 284–289. IEEE, 2006.

[37] Gregory Tholey and Jaydev P Desai. A modular, automated laparoscopic grasper with three-dimensional force measurement capability. In *Robotics and Automation, 2007 IEEE International Conference on*, pages 250–255. IEEE, 2007.

[38] Dong-Hyuk Lee, Uikyum Kim, Tauseef Gulrez, Woon Jong Yoon, Blake Hannaford, and Hyouk Ryeol Choi. A laparoscopic grasping tool with force sensing capability. *IEEE/ASME Trans. Mechatronics*, 21(1):130–141, 2016.

[39] Murat Cenk ÇavuÅ§oÇğlu, Frank Tendick, Michael Cohn, and S. Shankar Sastry. A laparoscopic telesurgical workstation. *IEEE Transactions on Robotics and Automation*, 15(4):728–739, 1999.

[40] Mark P Ottensmeyer and J Kenneth Salisbury. In vivo data acquisition instrument for solid organ mechanical property measurement. In *International Conference on Medical Image Computing and Computer-Assisted Intervention*, pages 975–982. Springer, 2001.

[41] Fouzia Khan, Roy J Roesthuis, and Sarthak Misra. Force sensing in continuum manipulators using fiber bragg grating sensors. In *2017 IEEE/RSJ International Conference on Intelligent Robots and Systems (IROS)*, pages 2531–2536. IEEE, 2017.

[42] Roy J Roesthuis, Sander Janssen, and Sarthak Misra. On using an array of fiber bragg grating sensors for closed-loop control of flexible minimally invasive surgical instruments. In *2013 IEEE/RSJ International Conference on Intelligent Robots and Systems*, pages 2545–2551. IEEE, 2013.

[43] Jan Peirs, Joeri Clijnen, Dominiek Reynaerts, Hendrik Van Brussel, Paul Herijgers, Brecht Corteville, and Sarah Boone. A micro optical force sensor for force feedback during minimally invasive robotic surgery. *Sensors and Actuators A: Physical*, 115(2):447–455, 2004.

[44] Pinyo Puangmali, Hongbin Liu, Kaspar Althoefer, and Lakmal D Seneviratne. Optical fiber sensor for soft tissue investigation during minimally invasive surgery. In *Robotics and Automation, 2008. ICRA 2008. IEEE International Conference on*, pages 2934–2939. IEEE, 2008.

[45] Kotaro Tadano and Kenji Kawashima. Development of 4-dofs forceps with force sensing using pneumatic servo system. In *Robotics and Automation, 2006. ICRA 2006. Proceedings 2006 IEEE International Conference on*, pages 2250–2255. IEEE, 2006.

[46] Luca Ascari, Cesare Stefanini, Arianna Menciassi, Sambit Sahoo, Pierre Rabischong, and Paolo Dario. A new active microendoscope for exploring the sub-arachnoid space in the spinal cord. In *Robotics and Automation, 2003. Proceedings. ICRA'03. IEEE International Conference on*, volume 2, pages 2657–2662. IEEE, 2003.

[47] Hiroki Takahashi, ShinâĂŹichi Warisawa, Mamoru Mitsuishi, Jumpei Arata, and Makoto Hashizume. Development of high dexterity minimally invasive surgical system with augmented force feedback capability. In *Biomedical Robotics and*

Biomechatronics, 2006. BioRob 2006. The First IEEE/RAS-EMBS International Conference on, pages 284–289. IEEE, 2006.

[48] Ankur Kapoor, Nabil Simaan, and Peter Kazanzides. A system for speed and torque control of dc motors with application to small snake robots. In *Mechatronics and Robotics*, 2004.

[49] Hongqiang Sang, Jintian Yun, Reza Monfaredi, Emmanuel Wilson, Hadi Fooladi, and Kevin Cleary. External force estimation and implementation in robotically assisted minimally invasive surgery. *The International Journal of Medical Robotics and Computer Assisted Surgery*, 13(2):e1824, 2017.

[50] Gregory Tholey, Anand Pillarisetti, William Green, and Jaydev Desai. Design, development, and testing of an automated laparoscopic grasper with 3-d force measurement capability. *Medical Simulation*, pages 38–48, 2004.

[51] Daisuke Haraguchi, Kotaro Tadano, and Kenji Kawashima. A prototype of pneumatically-driven forceps manipulator with force sensing capability using a simple flexible joint. In *Intelligent Robots and Systems (IROS), 2011 IEEE/RSJ International Conference on*, pages 931–936. IEEE, 2011.

[52] Kai Xu and Nabil Simaan. An investigation of the intrinsic force sensing capabilities of continuum robots. *IEEE Transactions on Robotics*, 24(3):576–587, 2008.

[53] Kai Xu and Nabil Simaan. Intrinsic wrench estimation and its performance index for multisegment continuum robots. *IEEE Transactions on Robotics*, 26(3):555–561, 2010.

[54] Daniel T Wallace, Gregory Stahler, Alex Goldenberg, Gene Reis, Robert G Younge, Mathew Clopp, David Camarillo, and Toby St John King. Method of sensing forces on a working instrument, November 8 2011. US Patent 8,052,621.

[55] Low Soon Chiang, Phee Soo Jay, Pietro Valdastri, Arianna Menciassi, and Paolo Dario. Tendon sheath analysis for estimation of distal end force and elongation. In *2009 IEEE/ASME International Conference on Advanced Intelligent Mechatronics*, pages 332–337. IEEE, July 2009.

[56] Timothy R Coles, Dwight Meglan, and Nigel W John. The role of haptics in medical training simulators: A survey of the state of the art. *IEEE Trans. Haptics*, 4(1):51–66, 2011.

[57] Anthony R Lanfranco, Andres E Castellanos, Jaydev P Desai, and William C Meyers. Robotic surgery: a current perspective. *Annals of surgery*, 239(1):14, 2004.

[58] DM Herron, M Marohn, et al. A consensus document on robotic surgery. *Surgical endoscopy*, 22(2):313–325, 2008.

[59] Nima Enayati, Elena De Momi, and Giancarlo Ferrigno. Haptics in robot-assisted surgery: challenges and benefits. *IEEE reviews in biomedical engineering*, 9:49–65, 2016.

[60] Min Li, Jelizaveta Konstantinova, and Kaspar Althoefer. *Soft and Stiffness-controllable Robotics Solutions for Minimally Invasive Surgery: The STIFF-FLOP Approach*, chapter Haptic Feedback Modalities for Minimally Invasive Surgery, page 229. River Publishers, 2018.

[61] Jelizaveta Konstantinova, Allen Jiang, Kaspar Althoefer, Prokar Dasgupta, and Thrishantha Nanayakkara. Implementation of tactile sensing for palpation in robot-assisted minimally invasive surgery: A review. *IEEE Sensors Journal*, 14(8):2490–2501, 2014.

[62] Blake Hannaford, Laurie Wood, Douglas A McAffee, and Haya Zak. Performance evaluation of a six-axis generalized force-reflecting teleoperator. *IEEE Trans. Syst., Man, Cybern.*, 21(3):620–633, 1991.

[63] Leonardo Meli, Claudio Pacchierotti, and Domenico Prattichizzo. Sensory subtraction in robot-assisted surgery: fingertip skin deformation feedback to ensure safety and improve transparency in bimanual haptic interaction. *IEEE Trans. Biomed. Eng.*, 61(4):1318–1327, 2014.

[64] C. R. Wagner, N. Stylopoulos, and R. D. Howe. The role of force feedback in surgery: analysis of blunt dissection. In *Proceedings 10th Symposium on Haptic Interfaces for Virtual Environment and Teleoperator Systems. HAPTICS 2002*, pages 68–74, March 2002.

[65] Allison M Okamura. Haptic feedback in robot-assisted minimally invasive surgery. *Current opinion in urology*, 19(1):102, 2009.

[66] Claudio Pacchierotti, Domenico Prattichizzo, and Katherine J Kuchenbecker. Displaying sensed tactile cues with a fingertip haptic device. *IEEE Trans. Haptics*, 8(4):384–396, 2015.

[67] Michael J Massimino and Thomas B Sheridan. Teleoperator performance with varying force and visual feedback. *Human factors*, 36(1):145–157, 1994.

[68] Domenico Prattichizzo, Claudio Pacchierotti, Stefano Cenci, Kouta Minamizawa, and Giulio Rosati. Using a fingertip tactile device to substitute kinesthetic feedback in haptic interaction. In *Proceedings of the 2010 International Conference on Haptics: Generating and Perceiving Tangible Sensations, Part I*, EuroHaptics'10, pages 125–130, Berlin, Heidelberg, 2010. Springer-Verlag.

[69] Eleanora P Westebring-van der Putten, Richard HM Goossens, Jack J Jakimowicz, and Jenny Dankelman. Haptics in minimally invasive surgery–a review. *Minimally Invasive Therapy & Allied Technologies*, 17(1):3–16, 2008.

[70] Claudio Pacchierotti, Domenico Prattichizzo, and Katherine J Kuchenbecker.

Cutaneous feedback of fingertip deformation and vibration for palpation in robotic surgery. *IEEE Trans. Biomed. Eng.*, 63(2):278–287, 2016.

[71] Arif Kazi. Operator performance in surgical telemanipulation. *Presence: Teleoperators & Virtual Environments*, 10(5):495–510, 2001.

[72] Brian T Bethea, Allison M Okamura, Masaya Kitagawa, Torin P Fitton, Stephen M Cattaneo, Vincent L Gott, William A Baumgartner, and David D Yuh. Application of haptic feedback to robotic surgery. *Journal of Laparoendoscopic & Advanced Surgical Techniques*, 14(3):191–195, 2004.

[73] Louise Moody, Chris Baber, Theodoros N Arvanitis, et al. Objective surgical performance evaluation based on haptic feedback. *Studies in health technology and informatics*, pages 304–310, 2002.

[74] Danilo De Lorenzo, Elena De Momi, Ilya Dyagilev, Rudy Manganelli, Alessandro Formaglio, Domenico Prattichizzo, Moshe Shoham, and Giancarlo Ferrigno. Force feedback in a piezoelectric linear actuator for neurosurgery. *The International Journal of Medical Robotics and Computer Assisted Surgery*, 7(3):268–275, 2011.

[75] Septimiu E Salcudean, S Ku, and G Bell. Performance measurement in scaled teleoperation for microsurgery. In *CVRMed-MRCAS'97*, pages 789–798. Springer, 1997.

[76] Momen Abayazid, Claudio Pacchierotti, Pedro Moreira, Ron Alterovitz, Domenico Prattichizzo, and Sarthak Misra. Experimental evaluation of co-manipulated ultrasound-guided flexible needle steering. *The International Journal of Medical Robotics and Computer Assisted Surgery*, 12(2):219–230, 2016.

[77] AM Galea and RD Howe. Tissue stiffness from tactile imaging. In *Engineering in Medicine and Biology, 2002. 24th Annual Conference and the Annual Fall Meeting*

of the Biomedical Engineering Society EMBS/BMES Conference, 2002. Proceedings of the Second Joint, volume 2, pages 935–936. IEEE, 2002.

[78] Samuel B Kesner and Robert D Howe. Discriminating tissue stiffness with a haptic catheter: Feeling the inside of the beating heart. In *World Haptics Conference (WHC), 2011 IEEE*, pages 13–18. IEEE, 2011.

[79] Vladimir Egorov, Heather Van Raalte, and Armen P Sarvazyan. Vaginal tactile imaging. *IEEE Trans. Biomed. Eng.*, 57(7):1736–1744, 2010.

[80] Andrew P Miller, William J Peine, Jae S Son, and MD Zane T Hammoud. Tactile imaging system for localizing lung nodules during video assisted thoracoscopic surgery. In *Proceedings 2007 IEEE International Conference on Robotics and Automation*, pages 2996–3001. IEEE, 2007.

[81] Hongbin Liu, David P Noonan, Benjamin J Challacombe, Prokar Dasgupta, Lakmal D Seneviratne, and Kaspar Althoefer. Rolling mechanical imaging for tissue abnormality localization during minimally invasive surgery. *IEEE Trans. Biomed. Eng.*, 57(2):404–414, 2010.

[82] Kirk Nichols, Allison M Okamura, et al. Autonomous robotic palpation: Machine learning techniques to identify hard inclusions in soft tissues. In *Robotics and Automation (ICRA), 2013 IEEE International Conference on*, pages 4384–4389. IEEE, 2013.

[83] Mohsen Mahvash, Jim Gwilliam, Rahul Agarwal, Balazs Vagvolgyi, Li-Ming Su, David D Yuh, and Allison M Okamura. Force-feedback surgical teleoperator: Controller design and palpation experiments. In *2008 Symposium on Haptic Interfaces for Virtual Environment and Teleoperator Systems*, pages 465–471. IEEE, 2008.

[84] Andrea Bajo and Nabil Simaan. Hybrid motion/force control of multi-backbone continuum robots. *The International journal of robotics research*, 35(4):422–434, 2016.

[85] Roger E Goldman, Andrea Bajo, and Nabil Simaan. Algorithms for autonomous exploration and estimation in compliant environments. *Robotica*, 31(1):71–87, 2013.

[86] Allison M Okamura. Methods for haptic feedback in teleoperated robot-assisted surgery. *Industrial Robot: An International Journal*, 31(6):499–508, 2004.

[87] Jan Hergenhan, Jacqueline Rutschke, Michael Uhl, Stefan Escaida Navarro, Bjorn Hein, and Heinz Worn. A haptic display for tactile and kinesthetic feedback in a chai 3d palpation training scenario. In *Robotics and Biomimetics (ROBIO), 2015 IEEE International Conference on*, pages 291–296. IEEE, 2015.

[88] Melissa T Perri, Ana Luisa Trejos, Michael D Naish, Rajni V Patel, and Richard A Malthaner. Initial evaluation of a tactile/kinesthetic force feedback system for minimally invasive tumor localization. *IEEE/ASME Trans. Mechatronics*, 15(6):925–931, 2010.

[89] Anatole Lécuyer, Jean-Marie Burkhardt, and Chee-Hian Tan. A study of the modification of the speed and size of the cursor for simulating pseudo-haptic bumps and holes. *ACM Transactions on Applied Perception (TAP)*, 5(3):14, 2008.

[90] Min Li, Hongbin Liu, Jichun Li, Lakmal D Seneviratne, and Kaspar Althoefer. Tissue stiffness simulation and abnormality localization using pseudo-haptic feedback. In *2012 IEEE International Conference on Robotics and Automation*, pages 5359–5364. IEEE, 2012.

[91] Shervin Ehrampoosh, Mohit Dave, Michael A Kia, Corneliu Rablau, and Mehrdad H Zadeh. Providing haptic feedback in robot-assisted minimally invasive surgery:

A direct optical force-sensing solution for haptic rendering of deformable bodies. *Computer Aided Surgery*, 18(5-6):129–141, 2013.

[92] Michel Franken, Stefano Stramigioli, Rob Reilink, Cristian Secchi, Alessandro Macchelli, et al. Bridging the gap between passivity and transparency. In *Robotics: Science and Systems*, 2009.

[93] Michel Franken, Stefano Stramigioli, Sarthak Misra, Cristian Secchi, and Alessandro Macchelli. Bilateral telemanipulation with time delays: A two-layer approach combining passivity and transparency. *IEEE Trans. Robot.*, 27(4):741–756, 2011.

[94] Leonardo Meli, Claudio Pacchierotti, and Domenico Prattichizzo. Experimental evaluation of magnified haptic feedback for robot-assisted needle insertion and palpation. *The International Journal of Medical Robotics and Computer Assisted Surgery*, 13(4):e1809, 2017.

[95] Marc L. Bennett, Dongqing Zhang, Robert F. Labadie, and Jack H. Noble. Comparison of Middle Ear Visualization With Endoscopy and Microscopy. *Otology & Neurotology*, page 1, mar 2016.

[96] Daniel L. Rothbaum, Jaydeep Roy, Dan Stoianovici, Peter Berkelman, Gregory D. Hager, Russell H. Taylor, Louis L. Whitcomb, Howard W. Francis, and John K. Niparko. Robot-assisted stapedotomy: Micropick fenestration of the stapes footplate. *Otolaryngology - Head and Neck Surgery*, 127(5):417–426, 2002.

[97] P. N. Brett, D. A. Baker, L. Reyes, and J. Blanshard. Automatic technique for micro-drilling a stapedotomy in the flexible stapes footplate. *Proceedings of the Institution of Mechanical Engineers, Part H: Journal of Engineering in Medicine*, 209(4):255–262, 1995.

[98] Mathieu Miroir, Yann Nguyen, Jérôme Szewczyk, Stéphane Mazalaigue, Evelyne Ferrary, Olivier Sterkers, and Alexis Bozorg Grayeli. RobOtol: From design to evaluation of a robot for middle ear surgery. *IEEE/RSJ 2010 International Conference on Intelligent Robots and Systems*, pages 850–856, 2010.

[99] Mathieu Miroir, Yann Nguyen, Jérôme Szewczyk, Olivier Sterkers, and Alexis Bozorg Grayeli. Design, Kinematic Optimization, and Evaluation of a Teleoperated System for Middle Ear Microsurgery. *The Scientific World Journal*, 2012, 2012.

[100] Guillaume Kazmitcheff, Yann Nguyen, Mathieu Miroir, Fabien Péan, Evelyne Ferrary, Stéphane Cotin, Olivier Sterkers, and Christian Duriez. Middle-Ear Microsurgery Simulation to Improve New Robotic Procedures. *BioMed Research International*, 2014, 2014.

[101] Thomas Maier, Gero Strauss, Markus Scholz, Thomas Berger, Anne Kielhorn, Konrad Entsfellner, Christian Willim, Wolfgang Buscher, Andreas Dietz, and Tim C Lueth. A new evaluation and training system for micro-telemanipulation at the middle ear. In *Annual International Conference of the IEEE Engineering in Medicine and Biology Society.*, volume 2012, pages 932–5, San Diego, CA, jan 2012.

[102] T. R. McRackan, W. M. Abdellatif, G. B. Wanna, A. Rivas, N. Gupta, M. S. Dietrich, and D. S. Haynes. Evaluation of Second Look Procedures for Pediatric Cholesteatomas. *Otolaryngology – Head and Neck Surgery*, 145(1):154–160, 2011.

[103] J. B. Hunter, M. G. Zuniga, A. D. Sweeney, N. M. Bertrand, G. B. Wanna, D. S. Haynes, C. T. Wootten, and A. Rivas. Pediatric Endoscopic Cholesteatoma Surgery. *Otolaryngology – Head and Neck Surgery*, 2016.

[104] Haoran Yu, Jin Hui Shen, Karen M. Joos, and Nabil Simaan. Design, calibration and preliminary testing of a robotic telemanipulator for OCT guided retinal surgery.

Proceedings - IEEE International Conference on Robotics and Automation, pages 225–231, 2013.

[105] Doug Stewart. A platform with six degrees of freedom. *Proceedings of the Institution of Mechanical Engineers*, 180(1965):371–386, 1965.

[106] V E Gough and S. G. Whitehall. Universal Tyre Test Machine. *Proc. FISITA 9th Int. Technical Congress*, pages 117–137, 1962.

[107] Yair Lotan, Jeffrey A. Cadeddu, and Matthew T. Gettman. The New Economics of Radical Prostatectomy: Cost Comparison of Open, Laparoscopic and Robot Assisted Techniques. *The Journal of Urology*, 172(4):1431–1435, 2004.

[108] Joshua A. Waters, David F. Canal, Eric A. Wiebke, Ryan P. Dumas, Joal D. Beane, Juan R. Aguilar-Saavedra, Chad G. Ball, Michael G. House, Nicholas J. Zyromski, Attila Nakeeb, Henry A. Pitt, Keith D. Lillemoe, and C. Max Schmidt. Robotic distal pancreatectomy: Cost effective? *Surgery*, 148(4):814–823, 2010.

[109] Jeffrey A. Morgan, Barbara A. Thornton, Joy C. Peacock, Karen W. Hollingsworth, Craig R. Smith, Mehmet C. Oz, and Michael Argenziano. Does robotic technology make minimally invasive cardiac surgery too expensive? A hospital cost analysis of robotic and conventional techniques. *Journal of Cardiac Surgery*, 20(3):246–251, may 2005.

[110] H. W R Schreuder, R Wolswijk, R. P. Zweemer, M. P. Schijven, and R. H M Verheijen. Training and learning robotic surgery, time for a more structured approach: A systematic review, jan 2012.

[111] Adele M. Goman and Frank R. Lin. Prevalence of hearing loss by severity in the United States. *American Journal of Public Health*, 106(10):1820–1822, oct 2016.

[112] National Institutes of Health (NIH). Cochlear Implants. Technical report, National Institute of Health, 2016.

[113] Susan D Emmett and Howard W Francis. The socioeconomic impact of hearing loss in U.S. adults. *Otology & neurotology: official publication of the American Otological Society, American Neurotology Society [and] European Academy of Otology and Neurotology*, 36(3):545–50, mar 2015.

[114] Penny E Mohr, Jacob J Feldman, Jennifer L Dunbar, Amy McConkey-Robbins, John K Niparko, Robert K Rittenhouse, and Margaret W Skinner. The societal costs of severe to profound hearing loss in the United States. *International Journal of Technology Assessment in Health Care*, 16(4):1120–1135, 2000.

[115] N. E. Morton. Genetic Epidemiology of Hearing Impairment. *Annals of the New York Academy of Sciences*, 630(1):16–31, sep 1991.

[116] André L L Sampaio, Mercêdes F S Araújo, and Carlos A C P Oliveira. New Criteria of Indication and Selection of Patients to Cochlear Implant. *International Journal of Otolaryngology*, 2011:1–13, 2011.

[117] Thomas J Balkany, Sarah S Connell, Annelle V Hodges, Stacy L Payne, Fred F Telischi, Adrien A Eshraghi, Simon I Angeli, Ross Germani, Sarah Messiah, and Kristopher L Arheart. Conservation of residual acoustic hearing after cochlear implantation. *Otology and Neurotology*, 27(8):1083–1088, 2006.

[118] Patricia A Leake, Gary T Hradek, and Russell L Snyder. Chronic electrical stimulation by a cochlear implant promotes survival of spiral ganglion neurons after neonatal deafness. *Journal of Comparative Neurology*, 412(4):543–562, 1999.

[119] Matthew L Carlson, Colin L W Driscoll, René H Gifford, Geoffrey J Service, Nicole M Tombers, Becky J Hughes-Borst, Brian a Neff, and Charles W Beatty.

Implications of minimizing trauma during conventional cochlear implantation. *Otology & neurotology : official publication of the American Otological Society, American Neurotology Society [and] European Academy of Otology and Neurotology*, 32(6):962–8, aug 2011.

[120] Pooyan Rohani, Jason Pile, Lueder A Kahrs, Ramya Balachandran, Grégoire S Blachon, Nabil Simaan, and Robert F Labadie. Forces and trauma associated with minimally invasive image-guided cochlear implantation. *Otolaryngology–Head and Neck Surgery*, 150(4):638–645, 2014.

[121] J H Frijns, J J Briaire, and J J Grote. The importance of human cochlear anatomy for the results of modiolus-hugging multichannel cochlear implants. *Otology & neurotology : official publication of the American Otological Society, American Neurotology Society [and] European Academy of Otology and Neurotology*, 22(3):340–9, may 2001.

[122] Brendan P. O'Connell, Jacob B Hunter, and George B Wanna. The importance of electrode location in cochlear implantation. *Laryngoscope Investigative Otolaryngology*, 1(6):169–174, 2016.

[123] George B Wanna, Jack H Noble, Matthew L Carlson, René H Gifford, Mary S Dietrich, David S Haynes, Benoit M Dawant, and Robert F Labadie. Impact of electrode design and surgical approach on scalar location and cochlear implant outcomes. *The Laryngoscope*, apr 2014.

[124] Stanley Pelosi, Jack H Noble, Benoit M Dawant, and Robert F Labadie. Analysis of intersubject variations in intracochlear and middle ear surface anatomy for cochlear implantation. *Otology and Neurotology*, 34(9):1675–1680, dec 2013.

[125] Jian Zhang, Kai Xu, Nabil Simaan, and Spiros Manolidis. A pilot study of robot-assisted cochlear implant surgery using steerable electrode arrays. In *International*

Conference on Medical Image Computing and Computer-Assisted Intervention, pages 33–40. Springer, 2006.

[126] Jason Pile and Nabil Simaan. Modeling, design, and evaluation of a parallel robot for cochlear implant surgery. *IEEE/ASME Transactions on Mechatronics*, 19(6):1746–1755, dec 2014.

[127] Jian Zhang, Wei Wei, Jienan Ding, J Thomas Roland Jr, Spiros Manolidis, and Nabil Simaan. Inroads toward robot-assisted cochlear implant surgery using steerable electrode arrays. *Otology & neurotology*, 31(8):1199–1206, 2010.

[128] Andreas Hussong, Thomas S. Rau, Tobias Ortmaier, Bodo Heimann, Thomas Lenarz, and Omid Majdani. An automated insertion tool for cochlear implants: Another step towards atraumatic cochlear implant surgery. *International Journal of Computer Assisted Radiology and Surgery*, 5(2):163–171, mar 2010.

[129] Daniel Schurzig, Robert F. Labadie, Andreas Hussong, Thomas S. Rau, and Robert J. Webster. Design of a tool integrating force sensing with automated insertion in cochlear implantation. *IEEE/ASME Transactions on Mechatronics*, 17(2):381–389, apr 2012.

[130] Trevor L. Bruns and Robert J. Webster. An image guidance system for positioning robotic cochlear implant insertion tools. volume 10135, page 101350O. International Society for Optics and Photonics, mar 2017.

[131] Robert F Labadie, Ramya Balachandran, Jack H Noble, Gr S egoire Blachon, Jason E Mitchell, Fitsum A Reda, Benoit M Dawant, and J Michael Fitzpatrick. Minimally Invasive Image-Guided Cochlear Implantation Surgery: First Report of Clinical Implementation. *The Laryngoscope*, 124:1915–1922, 2014.

[132] Marco Caversaccio, Kate Gavaghan, Wilhelm Wimmer, Tom Williamson, Juan Ansò, Georgios Mantokoudis, Nicolas Gerber, Christoph Rathgeb, Arne Feldmann,

Franca Wagner, Olivier Scheidegger, Martin Kompis, Christian Weisstanner, Masoud Zoka-Assadi, Kai Roesler, Lukas Anschuetz, Markus Huth, and Stefan Weber. Robotic cochlear implantation: surgical procedure and first clinical experience. *Acta Oto-Laryngologica*, 137(4):447–454, apr 2017.

[133] Lueder Alexander Kahrs, Theodore R McRackan, and Robert F Labadie. Intracochlear visualization: Comparing established and novel endoscopy techniques. *Otology and Neurotology*, 32(9):1590–1595, dec 2011.

[134] Jack H. Noble, Robert F. Labadie, George B. Wanna, and Benoit M. Dawant. Image guidance could aid performance of atraumatic cochlear implantation surgical techniques. In David R. Holmes and Ziv R. Yaniv, editors, *Medical Imaging 2013: Image-Guided Procedures, Robotic Interventions, and Modeling*, volume 8671, page 86711T. International Society for Optics and Photonics, mar 2013.

[135] Robert F Labadie and Jack H Noble. Preliminary results with image-guided cochlear implant insertion techniques. *Otology & Neurotology*, 39(7):922–928, 2018.

[136] Loris Fichera, Neal P Dillon, Dongqing Zhang, Isuru S Godage, Michael A Siebold, Bryan I Hartley, Jack H Noble, Paul T Russell, Robert F Labadie, and Robert J. Webster. Through the Eustachian Tube and Beyond: A New Miniature Robotic Endoscope to See Into The Middle Ear. *IEEE Robotics and Automation Letters*, 2(3):1488–1494, 2017.

[137] Jason Pile, Alex D. Sweeney, Shaun Kumar, Nabil Simaan, and George B. Wanna. Detection of modiolar proximity through bipolar impedance measurements, jun 2016.

[138] Saumya S Gurbani, Paul Wilkening, Mingtao Zhao, Berk Gonenc, Gyeong Woo Cheon, Iulian I Iordachita, Wade Chien, Russell H Taylor, John K Niparko, and Jin U Kang. Robot-assisted three-dimensional registration for cochlear implant surgery

using a common-path swept-source optical coherence tomography probe. *Journal of biomedical optics*, 19(5):057004, may 2014.

[139] J. Wang and K.D. Wise. A Hybrid Electrode Array With Built-In Position Sensors for an Implantable MEMS-Based Cochlear Prosthesis. *Journal of Microelectromechanical Systems*, 17(5):1187–1194, oct 2008.

[140] J. Pile, G. B. Wanna, and N. Simaan. Robot-assisted perception augmentation for online detection of insertion failure during cochlear implant surgery. *Robotica*, 35(07):1598–1615, jul 2017.

[141] Hanqi Zhuang, ZS Roth, and R Sudhakar. Practical fusion algorithms for rotation matrices: a comparative study. *Journal of robotic systems*, 9(7):915–931, 1992.

[142] Jason Pile and Nabil Simaan. Characterization of friction and speed effects and methods for detection of cochlear implant electrode tip fold-over. In *IEEE International Conference on Robotics and Automation*, pages 4409–4414, Karlsruhe, Germany, may 2013. IEEE.

[143] M Geraldine Zuniga, Alejandro Rivas, Andrea Hedley-Williams, Rene H Gifford, Robert Dwyer, Benoit M Dawant, Linsey W Sunderhaus, Kristen L Hovis, George B Wanna, Jack H Noble, and Robert F Labadie. Tip fold-over in cochlear implantation: Case series. In *Otology and Neurotology*, volume 38, pages 199–206. NIH Public Access, 2017.

[144] A Nemtoi, C Czink, D Haba, and A Gahleitner. Cone beam ct: a current overview of devices. *Dentomaxillofacial Radiology*, 42(8):20120443, 2013.

[145] Jack H. Noble, Robert F. Labadie, Omid Majdani, and Benoit M. Dawant. Automatic segmentation of intracochlear anatomy in conventional CT. *IEEE Transactions on Biomedical Engineering*, 58(9):2625–2632, sep 2011.

[146] Yiyuan Zhao, Benoit M Dawant, Robert F Labadie, and Jack H Noble. Automatic localization of cochlear implant electrodes in ct. In *International Conference on Medical Image Computing and Computer-Assisted Intervention*, pages 331–338. Springer, 2014.

[147] Lawrence T Cohen, Jin Xu, Shi Ang Xu, and Graeme M Clark. Improved and simplified methods for specifying positions of the electrode bands of a cochlear implant array. *Scientific publications, vol. 9, 1995-1996, no. 902*, 1996.

[148] Xenia Meshik, Timothy A Holden, Richard A Chole, and Timothy E Hullar. Optimal cochlear implant insertion vectors. *Otology & neurotology: official publication of the American Otological Society, American Neurotology Society [and] European Academy of Otology and Neurotology*, 31(1):58, 2010.

[149] Jason Pile. *Wire-Actuated Parallel Robots for Cochlear Implantation with In-Vivo Sensory Feedback*. PhD thesis, Vanderbilt University.

[150] Brendan P OâĂŹconnell, Ahmet Cakir, Jacob B Hunter, David O Francis, Jack H Noble, Robert F Labadie, Geraldine Zuniga, Benoit M Dawant, Alejandro Rivas, and George B Wanna. Electrode location and angular insertion depth are predictors of audiologic outcomes in cochlear implantation. *Otology & neurotology: official publication of the American Otological Society, American Neurotology Society [and] European Academy of Otology and Neurotology*, 37(8):1016, 2016.

[151] Kevin J. Choi and David M. Kaylie. What is the role of preoperative imaging for cochlear implants in adults with postlingual deafness? *Laryngoscope*, 127(2):287–288, feb 2017.

[152] Robert J Webster III, Joseph M Romano, and Noah J Cowan. Mechanics of precurved-tube continuum robots. *IEEE Transactions on Robotics*, 25(1):67–78, 2009.

[153] Pierre E Dupont, Jesse Lock, Brandon Itkowitz, and Evan Butler. Design and control of concentric-tube robots. *IEEE Trans. Robot.*, 26(2):209–225, 2010.

[154] Jessica Burgner-Kahrs, D Caleb Rucker, and Howie Choset. Continuum robots for medical applications: A survey. *IEEE Transactions on Robotics*, 31(6):1261–1280, 2015.

[155] Nabil Simaan, Russell Taylor, and Paul Flint. A dexterous system for laryngeal surgery. In *Robotics and Automation, 2004. Proceedings. ICRA'04. 2004 IEEE International Conference on*, volume 1, pages 351–357. IEEE, 2004.

[156] Aristeidis Sotiras, Christos Davatzikos, and Nikos Paragios. Deformable medical image registration: A survey. *IEEE transactions on medical imaging*, 32(7):1153–1190, 2013.

[157] Mitsuhiro Hayashibe, Naoki Suzuki, and Yoshihiko Nakamura. Laser-scan endoscope system for intraoperative geometry acquisition and surgical robot safety management. *Medical Image Analysis*, 10(4):509–519, 2006.

[158] Roger E Goldman, Andrea Bajo, and Nabil Simaan. Algorithms for autonomous exploration and estimation in compliant environments. *Robotica*, 31(1):71–87, 2013.

[159] Long Wang, Zihan Chen, Preetham Chalasani, Rashid M Yasin, Peter Kazanzides, Russell H Taylor, and Nabil Simaan. Force-controlled exploration for updating virtual fixture geometry in model-mediated telemanipulation. *Journal of Mechanisms and Robotics*, 9(2):021010, 2017.

[160] David M Kwartowitz, S Duke Herrell, and Robert L Galloway. Toward image-guided robotic surgery: determining intrinsic accuracy of the da vinci robot. *International Journal of Computer Assisted Radiology and Surgery*, 1(3):157–165, 2006.

[161] Nabil Simaan, Andrea Bajo, Austin Reiter, Long Wang, Peter Allen, and Dennis Fowler. Lessons learned using the insertable robotic effector platform (irep) for single port access surgery. *Journal of robotic surgery*, 7(3):235–240, 2013.

[162] A. Bajo, R. E. Goldman, and N. Simaan. Configuration and joint feedback for enhanced performance of multi-segment continuum robots. In *2011 IEEE International Conference on Robotics and Automation*, pages 2905–2912, May 2011.

[163] Nabil Simaan. Snake-like units using flexible backbones and actuation redundancy for enhanced miniaturization. In *Robotics and Automation, 2005. ICRA 2005. Proceedings of the 2005 IEEE International Conference on*, pages 3012–3017. IEEE, 2005.

[164] Bryan A Jones and Ian D Walker. Practical kinematics for real-time implementation of continuum robots. *IEEE Trans. Robot.*, 22(6):1087–1099, 2006.

[165] Robert J Webster III and Bryan A Jones. Design and kinematic modeling of constant curvature continuum robots: A review. *The International Journal of Robotics Research*, 29(13):1661–1683, 2010.

[166] Jienan Ding, Roger E Goldman, Kai Xu, Peter K. Allen, Dennis L. Fowler, and Nabil Simaan. Design and Coordination Kinematics of an Insertable Robotic Effectors Platform for Single-Port Access Surgery. *IEEE/ASME transactions on mechatronics*, 18(5):1612–1624, October 2013.

[167] Andrea Bajo, Roger E Goldman, Long Wang, Dennis Fowler, and Nabil Simaan. Integration and preliminary evaluation of an insertable robotic effectors platform for single port access surgery. In *Robotics and Automation (ICRA), 2012 IEEE International Conference on*, pages 3381–3387. IEEE, 2012.

[168] J. Ding, R. E. Goldman, K. Xu, P. K. Allen, D. L. Fowler, and N. Simaan. Design and coordination kinematics of an insertable robotic effectors platform for single-port access surgery. *IEEE/ASME Transactions on Mechatronics*, 18(5):1612–1624, Oct 2013.

[169] Kai Xu and Nabil Simaan. Actuation compensation for flexible surgical snake-like robots with redundant remote actuation. In *Proceedings 2006 IEEE International Conference on Robotics and Automation, 2006. ICRA 2006.*, pages 4148–4154. IEEE, 2006.

[170] Yoshihiko Nakamura and Hideo Hanafusa. Inverse Kinematic Solutions With Singularity Robustness for Robot Manipulator Control. *Journal of Dynamic Systems, Measurement, and Control*, 108(3):163–171, 09 1986.

[171] Tan Fung Chan and Rajiv V Dubey. A weighted least-norm solution based scheme for avoiding joint limits for redundant joint manipulators. *IEEE Transactions on Robotics and Automation*, 11(2):286–292, 1995.

[172] Roy Featherstone, Stef Sonck, and Oussama Khatib. A general contact model for dynamically-decoupled force/motion control. In *Experimental Robotics V*, pages 128–139. Springer, 1998.

[173] Peter Kazanzides, N. Scott Bradley, and William A. Wolovich. Dual-drive force/velocity control: implementation and experimental results. *Proceedings, 1989 International Conference on Robotics and Automation*, pages 92–97 vol.1, 1989.

[174] Jr Robert H. Cannon and Eric Schmitz. Initial experiments on the end-point control of a flexible one-link robot. *The International Journal of Robotics Research*, 3(3):62–75, 1984.

[175] Andriy Myronenko and Xubo Song. Point set registration: Coherent point drift.

IEEE transactions on pattern analysis and machine intelligence, 32(12):2262–2275, 2010.

[176] MD Naish, GL McCreery, AL Trejos, RV Patel, and RA Malthaner. Effect of velocity control on kinesthetic lung tumour localization. In *Electrical and Computer Engineering, 2008. CCECE 2008. Canadian Conference on*, pages 001337–001340. IEEE, 2008.

[177] Rangaprasad Arun Srivatsan, Elif Ayvali, Long Wang, Rajarshi Roy, Nabil Simaan, and Howie Choset. Complementary model update: A method for simultaneous registration and stiffness mapping in flexible environments. In *Robotics and Automation (ICRA), 2016 IEEE International Conference on*, pages 924–930. IEEE, 2016.

[178] Stephen McKinley, Animesh Garg, Siddarth Sen, Rishi Kapadia, Adithyavairavan Murali, Kirk Nichols, Susan Lim, Sachin Patil, Pieter Abbeel, Allison M Okamura, et al. A single-use haptic palpation probe for locating subcutaneous blood vessels in robot-assisted minimally invasive surgery. In *2015 IEEE International Conference on Automation Science and Engineering (CASE)*, pages 1151–1158. IEEE, 2015.

[179] Preetham Chalasani, Long Wang, Rashid Yasin, Nabil Simaan, and Russell H Taylor. Preliminary evaluation of an online estimation method for organ geometry and tissue stiffness. *IEEE Robotics and Automation Letters*, 3(3):1816–1823, 2018.

[180] P. Chalasani, L. Wang, R. Roy, N. Simaan, R. H. Taylor, and M. Kobilarov. Concurrent nonparametric estimation of organ geometry and tissue stiffness using continuous adaptive palpation. In *2016 IEEE International Conference on Robotics and Automation (ICRA)*, pages 4164–4171, May 2016.

[181] Roger E Goldman, Andrea Bajo, and Nabil Simaan. Compliant motion control for

multisegment continuum robots with actuation force sensing. *IEEE Transactions on Robotics*, 30(4):890–902, 2014.

[182] Andrea Bajo, Roger E Goldman, Long Wang, Dennis Fowler, and Nabil Simaan. Integration and preliminary evaluation of an insertable robotic effectors platform for single port access surgery. In *2012 IEEE International Conference on Robotics and Automation*, pages 3381–3387. IEEE, 2012.

[183] AL Trejos, RV Patel, and MD Naish. Force sensing and its application in minimally invasive surgery and therapy: a survey. *Proceedings of the Institution of Mechanical Engineers, Part C: Journal of Mechanical Engineering Science*, 224(7):1435–1454, 2010.

[184] Samuel B. Kesner and Robert D. Howe. Robotic catheter cardiac ablation combining ultrasound guidance and force control. *The International Journal of Robotics Research*, 33(4):631–644, 2014.

[185] Masaya Kitagawa, Daniell Dokko, Allison M Okamura, and David D Yuh. Effect of sensory substitution on suture-manipulation forces for robotic surgical systems. *The Journal of thoracic and cardiovascular surgery*, 129(1):151–158, 2005.

[186] M. Mahvash and P. E. Dupont. Stiffness control of surgical continuum manipulators. *IEEE Transactions on Robotics*, 27(2):334–345, April 2011.

[187] Junghwan Back, Thomas Manwell, Rashed Karim, Kawal Rhode, Kaspar Althoefer, and Hongbin Liu. Catheter contact force estimation from shape detection using a real-time cosserat rod model. In *Intelligent Robots and Systems (IROS), 2015 IEEE/RSJ International Conference on*, pages 2037–2042. IEEE, 2015.

[188] Mahta Khoshnam, Allan C Skanes, and Rajni V Patel. Modeling and estimation of tip contact force for steerable ablation catheters. *IEEE Trans. Biomed. Eng.*, 62(5):1404–1415, 2015.

[189] Mahta Khoshnam and Rajni V Patel. Estimating contact force for steerable ablation catheters based on shape analysis. In *Intelligent Robots and Systems (IROS 2014), 2014 IEEE/RSJ International Conference on*, pages 3509–3514. IEEE, 2014.

[190] Junghwan Back, Lukas Lindenroth, Rashed Karim, Kaspar Althoefer, Kawal Rhode, and Hongbin Liu. New kinematic multi-section model for catheter contact force estimation and steering. In *Intelligent Robots and Systems (IROS), 2016 IEEE/RSJ International Conference on*, pages 2122–2127. IEEE, 2016.

[191] Shahir Hasanzadeh and Farrokh Janabi-Sharifi. Model-based force estimation for intracardiac catheters. *IEEE/ASME Trans. Mechatronics*, 21(1):154–162, 2016.

[192] D Caleb Rucker and Robert J Webster. Deflection-based force sensing for continuum robots: A probabilistic approach. In *Intelligent Robots and Systems (IROS), 2011 IEEE/RSJ International Conference on*, pages 3764–3769. IEEE, 2011.

[193] R. Roy, L. Wang, and N. Simaan. Modeling and estimation of friction, extension, and coupling effects in multisegment continuum robots. *IEEE/ASME Transactions on Mechatronics*, 22(2):909–920, April 2017.

[194] Ferenc Preisach. Uber die magnetische nachwirkung. *Zeitschrift fur physik*, 94(5-6):277–302, 1935.

[195] R. Roy, L. Wang, and N. Simaan. Investigation of effects of dynamics on intrinsic wrench sensing in continuum robots. In *2016 IEEE International Conference on Robotics and Automation (ICRA)*, pages 2052–2059, May 2016.

[196] Jun Zhang, Emmanuelle Merced, Nelson Sepúlveda, and Xiaobo Tan. Modeling and inverse compensation of hysteresis in vanadium dioxide using an extended generalized prandtl–ishlinskii model. *Smart Materials and Structures*, 23(12):125017, 2014.

[197] Jun Zhang, Anthony Simeonov, and Michael C Yip. Three-dimensional hysteresis compensation enhances accuracy of robotic artificial muscles. *Smart Materials and Structures*, 27(3):035002, 2018.

[198] Giovanni Finocchio, Ermanno Cardelli, and Bruno Azzerboni. A simplified model for vector hysteresis computation. *IEEE transactions on magnetics*, 42(4):955–958, 2006.

[199] Chih-Chung Chang and Chih-Jen Lin. Training v-support vector regression: theory and algorithms. *Neural computation*, 14(8):1959–1977, 2002.

[200] Peter Kazanzides, Zihan Chen, Anton Deguet, Gregory S. Fischer, Russell H. Taylor, and Simon P. DiMaio. An open-source research kit for the da vinci surgical system. In *IEEE Intl. Conf. on Robotics and Auto. (ICRA)*, pages 6434–6439, Hong Kong, China, 2014.

[201] Sandra G Hart. Nasa-task load index (nasa-tlx); 20 years later. In *Proceedings of the human factors and ergonomics society annual meeting*, volume 50, pages 904–908. Sage publications Sage CA: Los Angeles, CA, 2006.

[202] Jacob Rosen, Blake Hannaford, Christina G Richards, and Mika N Sinanan. Markov modeling of minimally invasive surgery based on tool/tissue interaction and force/torque signatures for evaluating surgical skills. *IEEE transactions on Biomedical Engineering*, 48(5):579–591, 2001.

[203] Ali Talasaz, Ana Luisa Trejos, and Rajni V Patel. Effect of force feedback on performance of robotics-assisted suturing. In *Biomedical Robotics and Biomechatronics (BioRob), 2012 4th IEEE RAS & EMBS International Conference on*, pages 823–828. IEEE, 2012.

[204] Michael J Massimino and Thomas B Sheridan. Sensory substitution for force

feedback in teleoperation. *Presence: Teleoperators & Virtual Environments*, 2(4):344–352, 1993.

[205] Min Li, Jelizaveta Konstantinova, Guanghua Xu, Bo He, Vahid Aminzadeh, Jun Xie, Helge Wurdemann, and Kaspar Althoefer. Evaluation of stiffness feedback for hard nodule identification on a phantom silicone model. *PloS one*, 12(3):e0172703, 2017.

[206] Tomonori Yamamoto, Niki Abolhassani, Sung Jung, Allison M Okamura, and Timothy N Judkins. Augmented reality and haptic interfaces for robot-assisted surgery. *The International Journal of Medical Robotics and Computer Assisted Surgery*, 8(1):45–56, 2012.

[207] Mahya Shahbazi, Seyed Farokh Atashzar, and Rajni V Patel. A systematic review of multilateral teleoperation systems. *IEEE Trans. Haptics*, 11(3):338–356, 2018.

[208] Takayuki Osa, Naohiko Sugita, and Mamoru Mitsuishi. Online trajectory planning and force control for automation of surgical tasks. *IEEE Trans. Autom. Sci. Eng.*, 15(2):675–691, 2017.

[209] Preetham Chalasani, Long Wang, Rajarshi Roy, Nabil Simaan, Russell H Taylor, and Marin Kobilarov. Concurrent nonparametric estimation of organ geometry and tissue stiffness using continuous adaptive palpation. In *Robotics and Automation (ICRA), 2016 IEEE International Conference on*, pages 4164–4171. IEEE, 2016.

[210] Elif Ayvali, Rangaprasad Arun Srivatsan, Long Wang, Rajarshi Roy, Nabil Simaan, and Howie Choset. Using bayesian optimization to guide probing of a flexible environment for simultaneous registration and stiffness mapping. In *Robotics and Automation (ICRA), 2016 IEEE International Conference on*, pages 931–936. IEEE, 2016.

[211] Probal Mitra and Günter Niemeyer. Model mediated telemanipulation. In *ASME*

2006 International Mechanical Engineering Congress and Exposition, pages 1393–1401. American Society of Mechanical Engineers, 2006.

[212] Probal Mitra and Günter Niemeyer. Model-mediated telemanipulation. *The International Journal of Robotics Research*, 27(2):253–262, 2008.

[213] Xiao Li and Peter Kazanzides. Task frame estimation during model-based teleoperation for satellite servicing. In *2016 IEEE International Conference on Robotics and Automation (ICRA)*, pages 2834–2839. IEEE, 2016.

[214] Tian Xia, Simon Léonard, Isha Kandaswamy, Amy Blank, Louis L Whitcomb, and Peter Kazanzides. Model-based telerobotic control with virtual fixtures for satellite servicing tasks. In *Robotics and Automation (ICRA), 2013 IEEE International Conference on*, pages 1479–1484. IEEE, 2013.

[215] Zihan Chen, Anton Deguet, Russel Taylor, Simon DiMaio, Gregory Fischer, and Peter Kazanzides. An open-source hardware and software platform for telesurgical robot research. In *MICCAI Workshop on Systems and Arch. for Computer Assisted Interventions*, Sep 2013.

[216] Min Yang Jung, Anton Deguet, and Peter Kazanzides. A component-based architecture for flexible integration of robotic systems. In *Intelligent Robots and Systems (IROS), 2010 IEEE/RSJ International Conference on*, pages 6107–6112. IEEE, 2010.

[217] H. Lin, C. Vincent Hui, Y. Wang, A. Deguet, P. Kazanzides, and K. W. S. Au. A reliable gravity compensation control strategy for dvrk robotic arms with nonlinear disturbance forces. *IEEE Robotics and Automation Letters*, 4(4):3892–3899, Oct 2019.

[218] David M. Kwartowitz, S. Duke Herrell, and Robert L. Galloway. Toward image-guided robotic surgery: determining intrinsic accuracy of the da Vinci robot.

International Journal of Computer Assisted Radiology and Surgery, 1(3):157–165, oct 2006.

[219] David M. Kwartowitz, S. Duke Herrell, and Robert L. Galloway. Update: Toward image-guided robotic surgery: determining the intrinsic accuracy of the daVinci-S robot. *International Journal of Computer Assisted Radiology and Surgery*, 1(5):301–304, mar 2007.

[220] Andriy Fedorov, Reinhard Beichel, Jayashree Kalpathy-Cramer, Julien Finet, Jean-Christophe Fillion-Robin, Sonia Pujol, Christian Bauer, Dominique Jennings, Fiona Fennessy, Milan Sonka, et al. 3d slicer as an image computing platform for the quantitative imaging network. *Magnetic resonance imaging*, 30(9):1323–1341, 2012.

[221] J Michael Fitzpatrick, Jay B West, and Calvin R Maurer. Predicting error in rigid-body point-based registration. *IEEE transactions on medical imaging*, 17(5):694–702, 1998.

[222] Andriy Myronenko and Xubo Song. Point set registration: coherent point drift. *IEEE Trans. Pattern Anal. Mach. Intell.*, 32(12):2262–75, December 2010.

[223] Rashid Yasin, Long Wang, Colette Abah, and Nabil Simaan. Using continuum robots for force-controlled semi autonomous organ exploration and registration. In *Medical Robotics (ISMR), 2018 International Symposium on*, pages 1–6. IEEE, 2018.

[224] Shinji Umeyama. Least-squares estimation of transformation parameters between two point patterns. *IEEE Transactions on Pattern Analysis & Machine Intelligence*, (4):376–380, 1991.